

SEARCHING FOR GRAVITATIONAL WAVES ASSOCIATED WITH FLARING
GALACTIC MAGNETARS

by

KARA MERFELD

A DISSERTATION

Presented to the Department of Physics
and the Division of Graduate Studies of the University of Oregon
in partial fulfillment of the requirements
for the degree of
Doctor of Philosophy

June 2023

DISSERTATION APPROVAL PAGE

Student: Kara Merfeld

Title: Searching for Gravitational Waves associated with Flaring galactic Magnetars

This dissertation has been accepted and approved in partial fulfillment of the requirements for the Doctor of Philosophy degree in the Department of Physics by:

Benjamin Farr	Chair
Raymond Frey	Advisor
Robert Schofield	Core Member
Laura Jeanty	Core Member
Carol Paty	Institutional Representative

and

Krista Chronister	Vice Provost for Graduate Studies
-------------------	-----------------------------------

Original approval signatures are on file with the University of Oregon Division of Graduate Studies.

Degree awarded June 2023

© 2023 Kara Merfeld
All rights reserved.

DISSERTATION ABSTRACT

Kara Merfeld

Doctor of Philosophy

Department of Physics

June 2023

Title: Searching for Gravitational Waves associated with Flaring galactic Magnetars

The third observing run of Advanced LIGO and Virgo (O3) took place from April 1st, 2019 to September 30th, 2019, and from November 1st, 2019 to March 27th, 2020. The multi-messenger astronomy efforts during O3 included conducting gravitational-wave follow-up searches to electromagnetic burst sources, specifically Gamma-Ray Bursts, Fast Radio Bursts (FRBs), and magnetar x-ray bursts. The overarching goal of the research described in this dissertation is to improve the sensitivity of the LIGO burst searches in the third observing run, and to expand on our data analysis methods for the next observing run.

Magnetars are highly magnetized neutron stars with intermittent x-ray bursting behavior. We present a gravitational-wave follow-up search on the magnetar bursts from O3. This is an expansion on a similar search that was done in the second observing run (O2), and we present the differences in search methods and their effects. We place the most stringent upper limits on gravitational wave energy of any gravitational-wave search to date, and while these upper limits are still not low enough to be astrophysically meaningful, they do provide a framework for future searches.

FRBs are short-duration, bright bursts of radio signal from far outside Milky Way galaxy. We conduct the first-ever search for unmodeled gravitational-wave transients coincident with FRBs detected by the Canadian Hydrogen Intensity Mapping Experiment, the largest population of FRBs detected so far. We search over both repeating and non-repeating FRBs. Although we find no evidence for a signal, the study does lay the groundwork for future FRB searches from sources within our detection radius.

A stacked search in which multiple triggers are analyzed simultaneously is motivated by a number of very marginal triggers in the O3 magnetar search. We develop a version of an existing LIGO burst pipeline that can perform a stacked analysis. We describe the methods, and demonstrate a reduction in the root-sum-squared strain that an unstacked event would need to have if it were to be detected in a stacked analysis with a specific p-value. We also present sensitivity studies to determine how to optimize our pipeline.

CURRICULUM VITAE

NAME OF AUTHOR: Kara Merfeld

GRADUATE AND UNDERGRADUATE SCHOOLS ATTENDED:

University of Oregon, Eugene, OR, USA

University of Puget Sound, Tacoma, WA, USA

Everett Community College, Everett, WA, USA

California State University at Los Angeles, Los Angeles, CA, USA

DEGREES AWARDED:

Doctor of Philosophy, Physics, University of Oregon, 2023

Master of Science, Physics, University of Oregon, 2020

Bachelor of Science, Physics and Mathematics, University of Puget Sound,
2014

AREAS OF SPECIAL INTEREST:

Gravitational Wave Astrophysics

PROFESSIONAL EXPERIENCE:

Research Assistant, 2018-2023

Teaching Assistant, 2017-2018

Peace Corps Volunteer, Mozambique, 2014-2016

GRANTS, AWARDS AND HONORS:

LIGO Scientific Collaboration fellow, Hanford Observatory

PUBLICATIONS:

56 LIGO Scientific Collaboration papers published between 2018 and the present.

Publications for which I was on the paper-writing team:

The LIGO Scientific Collaboration, the Virgo Collaboration, the KAGRA Collaboration, and CHIME/FRB Collaboration. Search for gravitational waves associated with fast radio bursts detected by chime/frb during the ligo-virgo observing run o3a. 2022. Submitted to the *Astrophysical Journal*.

Publications for which I was a co-manager:

The LIGO-Virgo-KAGRA Collaboration. Search for gravitational-wave transients associated with magnetar bursts in advanced ligo and advanced virgo data from the third observing run, 2022. URL <https://arxiv.org/abs/2210.10931>. Submitted to the *Astrophysical Journal*.

Publications for which I participated as a data analyst:

The LIGO-Virgo-KAGRA Collaboration. Search for gravitational waves associated with gamma-ray bursts detected by fermi and swift during the LIGO-virgo run o3a. *The Astrophysical Journal*, 915(2):86, jul 2021. doi: 10.3847/1538-4357/abee15.

The LIGO-Virgo-KAGRA Collaboration. Search for gravitational waves associated with gamma-ray bursts detected by fermi and swift during the LIGO-virgo run o3b. *The Astrophysical Journal*, 928(2):186, apr 2022. doi: 10.3847/1538-4357/ac532b.

Instrumental author list publications:

D. Davis et al. LIGO detector characterization in the second and third observing runs. *Classical and Quantum Gravity*, 38(13):135014, jun 2021. doi: 10.1088/1361-6382/abfd85. URL <https://doi.org/10.10882F1361-63822Fabfd85>.

S. Soni et al. Reducing scattered light in LIGO's third observing run. *Classical and Quantum Gravity*, 38(2):025016, jan 2021. doi: 10.1088/1361-6382/abc906. URL <https://doi.org/10.10882F1361-63822Fabc906>.

A. Buikema et al. Sensitivity and performance of the advanced LIGO detectors in the third observing run. *Physical Review D*, 102(6), sep 2020. doi: 10.1103/physrevd.102.062003. URL <https://doi.org/10.11032Fphysrevd.102.062003>.

Conference Preceedings:

K. Merfeld. Search for gravitational-wave transients associated with magnetar bursts during the third advanced LIGO and advanced virgo observing run. *Proceedings of the International Astronomical Union*, 16(S363): 187–190, Jun 2020. doi: 10.1017/s1743921322002629. URL <https://doi.org/10.10172Fs1743921322002629>.

ACKNOWLEDGEMENTS

There are a great many people to whom I owe my gratitude for making this research possible. I'm firstly grateful to the people who helped me with the actual research: Ray Frey, for helping me navigate through the challenges and uncertainties of graduate school, and for always encouraging me to take on new challenges. I'm grateful to Robert Schofield for his help when I was at Hanford, and for always inviting questions and taking the time to make sure I understand the instrumentation. I also want to acknowledge Patrick Sutton for his help on untangling x-pipeline for the magnetar search and his help on the stacking project. And lastly Ryan Quitzow-James; Ryan put in so much time to help me learn the ropes of leading a collaboration project, and doing burst searches in general, and was a completely invaluable resource during my graduate career.

I also want to acknowledge my family, who supported my decision to go to graduate school, and has shown incredible resilience over these last five years. My dad never stopped living the life that he wanted, and never stopped reminding us that "life is good". I'm reminded every day to leave work behind and go have fun with my time here on Earth. My mom is the 2nd most courageous person I know – I might not have grown up to be a cheeky hell-raiser without her example, and I don't know how I would have survived the program if I weren't one. My brother was the first in our immediate family to earn higher than a Bachelors' degree; I suppose I ought to acknowledge that he beat me to it. I also need to acknowledge Chris Nair, one of the best friends and mentors that I'm ever likely to have. Chris was easily the most intelligent person I've ever known; he was curious

and encouraged me to be as well. He lost his life part way through my first year in the program.

I also need to acknowledge the Covid-19 pandemic, and express gratitude to the essential workers who carried society through the dark time. The pandemic also played another key role in my graduate career in that it allowed me to work remotely. I spent 1 month in Northern Ireland, and a year and a half in Ireland, split between county Mayo and Galway. I went through a lock down in Creagh House, with circa 15 other people from around the world, with traditional Irish music sessions and set dancing a few times a week. This crew turned into a broader community and has been incredibly welcoming to me for my entire time in the country. I got to return and spend a month in Montepuez, Mozambique. I saw my old friends again, caught up with my students, and told tales of gravitational waves in my old Peace Corps site while dodging a pandemic and watching my old community navigate development and the arrival of tens of thousands of refugees. Then I spent 2 months in Tanzania, 1.5 months in Egypt, 1.5 months in France, 2.5 months in Scotland, a month in Portugal, and 3 weeks in Greece. There is no possible way to travel meaningfully and integrate into local cultures without emerging a changed and more broadened version of yourself.

TABLE OF CONTENTS

Chapter	Page
I. INTRODUCTION	2
1.1. Forward	2
1.2. Introduction to Magnetars	4
1.3. The fundamental pressure mode of a neutron star	8
1.4. Organization of Thesis	17
II. GENERAL RELATIVITY AND THE LIGO OBSERVATORIES	20
2.1. Gravity and an Introduction to General Relativity	20
2.2. Introduction to the LIGO Observatories	28
2.3. Detector Response to a Gravitational Wave	32
2.4. ALS glitches	36
2.5. Feedforward Filters	46
2.6. Violin Mode Damping Filters	55
III. O3 MAGNETAR SEARCH	61
3.1. Introduction	61
3.2. Magnetar Flares in O3 LIGO and Virgo Data	64
3.3. Search Methods	67

Chapter	Page
3.4. Results	77
3.5. Short-Duration Results	79
3.6. Long-Duration Results	95
3.7. Sensitivity of the 2-component short-duration search	98
3.8. Conclusion	102
IV. O3 FAST RADIO BURST SEARCH	106
4.1. Introduction to Fast Radio Bursts	106
4.2. The FRB Sample	115
4.3. Methods	119
4.4. Results	123
4.5. Conclusion	125
V. A SEARCH FOR REPEATED, LOW-SNR TRANSIENTS	127
5.1. Introduction to and history of stacked searches	127
5.2. Description of x-pipeline (x-pipeline)	129
5.3. Modifications to x-pipeline to Enable Stacking	135
5.4. P-values and measures of sensitivity in stacking	138
5.5. Sensitivity Studies	142
5.6. The Mean Significance required to produce a given p-value	149
5.7. A demonstration of the reduction of the $h_{\text{RSS}}^{50\%}$ with stacking	161
5.8. Efficacy of stacking N triggers	163
5.9. Conclusion	166

Chapter	Page
VI. APPENDIX	168
6.1. Documentation of the new x-pipeline Stacking Features	168
REFERENCES CITED	174

LIST OF FIGURES

Figure	Page
<p>1. A lightcurve for magnetar x-ray trigger 2656 (naming convention consistent with that of [1]) from SGR 1935+2154 (SGR 1935+2154). The majority of photons fell in the 10-44 keV energy range, and we show histograms of the photon count rates in two of the channels in red and green [2].</p>	6
<p>2. The QPOs observed in the 2004 giant flare from SGR 1806-20 [3]. The excited frequencies of oscillation range from 18 Hz to 2384 Hz, and are detected for tens to hundreds of seconds in the first 300 s after the giant flare. The rotational period of SGR 1806-20 is 7.548 s, which matches the most prominent oscillation in this plot. It is also important to note that the scaling is chosen to show the QPOs, and the initial burst is off the plot.</p>	9
<p>3. The effects of the plus and cross polarization on a ring of stationary point particles at different stages of phase evolution [4]. The top row represents the effects of the + polarization, and the bottom row represents the x polarization. In each case the arrangement of particles is elongated along one axis, returns to its circular shape, and then is elongated along the perpendicular axis before returning to its unperturbed state when the phase reaches 2π.</p>	27
<p>4. The optical setup of Advanced LIGO [5]</p>	31
<p>5. Antenna response pattern for a gravitational wave detector for the + polarization (left), the X polarization (center) and mean polarization (right) [6, 7]. The arms of the gravitational-wave detector are taken to lie along the black lines, and the radius from a point on the surface to the origin represents the sensitivity to gravitational waves of that polarization in that direction.</p>	35
<p>6. The optical setup of the Arm Length Stabilization system.</p>	38
<p>7. The second trend data from the Y-arm transmission channel taken on December 13th, 2018 [8]. The green shows the minimum values per second. The first events that were having a noticeable effect on locking the interferometer are most visible as small dips in the minimum trend</p>	

Figure	Page
between about 10:10 and 10:13 UTC. These were the ones that were first coined as ‘rainy day glitches’ by the commissioners.	39
8. A zoom in of the trend data from the Y-arm transmission channel taken on December 13th, 2018 [8]. The drop in the signal indicates a high-frequency ALS glitch.	40
9. The control signal at both the times of the noise-eater events (top) and the times of the ALS glitches (bottom). We see that when the algorithm identifies a noise-eater event, there is a lot more noise in the signal than when it identifies an ALS glitch. On the bottom, we see that just before the time of each ALS glitch, the control signal jumps up to a higher value, and remains there and then comes back down just after the glitch, forming what we call a ‘plateau’ in the signal. The locations of these plateaus are emphasized with red circles.	41
10. The standard error on the lines of best fit to the control signal. We fit lines to the signal both before and after a distinct rise in the signal. Here we have four histograms of the standard error of these lines: the blue and grey histograms are from data before and after noise-eater events respectively, and the red and yellow distributions are from before and after true ALS glitches respectively. We can see distinct population differences in the standard errors for ALS glitches and for noise-eater events, and we choose our threshold values such that we can optimize the accuracy of our glitch identification algorithm.	43
11. ALS glitches identified over a 10 s span of time by the algorithm involving both the control and transmission signals. This was a span of time containing events that the commissioners identified as true ALS glitches that were detrimental for the locking process. The red signal is the transmission signal, the blue signal is the control signal, and the horizontal black line on the bottom plot represents the threshold value of the high-passed transmission signal at which a transmission glitch is identified. The times of the ALS glitches here are indicated by vertical green lines.	44
12. A timeline of the ALS glitch rates (10 s averages) between September 2018 and July 2019, calculated using the algorithm involving both transmission and control signals. As with the previous algorithm, there is no obvious improvement after the fiber was re-buried, and the improvement after the beginning of third observing run (O3) is likely due to longer lock stretches and therefore less time spent locking.	45

Figure	Page
13. We make the analogous ALS glitch timeline to that shown in Figure 12, for O2, using the algorithm involving transmission and control signals. This algorithm identifies a very clear start to these events after the commissioning break (from May 8th to May 25th, 2017), and a point in time when the ALS glitches were solved by taping down a flapping tag in the MSR [9]. This suggests that ALS glitches can be caused by mechanical disturbances to the fiber, and also lends credence to the algorithm that we use on O3 data.	46
14. Schematic of the control loops for each Length Sensing and Control degree of freedom [10]. The triangles on the left each represent a digital control filter, one for DARM and one for MICH, given by subscripts D and M in their respective labels. The triangle labeled α is the feedforward filter. The diamonds on the right are frequency independent sensors. $P_{(D \rightarrow S_D)}$ and $P_{(M \rightarrow S_M)}$ represent any frequency dependent actuation, optics, and electronics. $P_{(M \rightarrow S_D)}$ and $P_{(\alpha \rightarrow S_D)}$ are both coupling functions from the MICH actuation to the DARM, and from the feedforward filter to DARM respectively. n_{act} and n_{sens} are the noise from MICH actuation and sensing.	48
15. The optimal PRCL ZPK filter used in O3, [11]. The magnitude and phase of the measured transfer function from PRCL to DARM is displayed on the top and bottom plots respectively in blue. The orange lines are the magnitude and phase of the optimal filter. The shaded region shows the frequency range that is important to actuate in. Outside of this range the magnitude of the filter should drop so as not to inject into DARM. Our filter is a good fit to the optimal transfer function in most of the frequency band of highest importance, but we see that the phase of our ZPK filter is very misaligned with the optimal phase at around 10 Hz.	51
16. The minute trend of LIGO's sensitivity, as measured by the BNS inspiral range in Mpc. The time at which the PRCL filter is implemented as shown, and we see an increase in range of just over 2 Mpc [11].	52
17. The coherence between the PRCL and DARM at each frequency before (red) and after (green) the filter [11]. We see a reduction in coherence in the frequency band at which the filter actuates.	53
18. The noise budget for each LSC degree of freedom after the PRCL filter was implemented, with squeezing [12].	54

Figure	Page
19. The multiplicative residuals between α and the best fit to α . [11]. A perfect filter would yield a multiplicative residual amplitude of 1 and phase of 0 at every frequency. The red lines represent an arbitrary margin of error on the residuals to still have an acceptable filter. Any iterative filters should prioritize the frequencies which fall outside of this range.	55
20. The quadrupole suspension system for the Advanced LIGO test masses, the End Test Masses (ETMs) and the Input Test Masses (ITMs) [13].	57
21. The normalized gravitational-wave strain data with both the first and second-order violin modes present at approximately 500 Hz and 1000 Hz, respectively. The strength of these modes decays over time, as a result of the automated damping filters.	59
22. The 2nd order violin modes at H1 before and after the damping filters were applied.	60
23. Sky locations and 1σ error regions of the four electromagnetic bursts from an unknown source. These are triggers 2669-2672 in the SGR trigger catalogue. We also mark the location of the nearest magnetar (1 RXS J170849) which falls in the 3σ uncertainty region of all four bursts. We indicate the locations of the other known magnetars including SGR 1935+2154 and Swift J1818–1607. We overlay this with the coordinates of the plane of the Milky Way, according to the J2000 coordinate system.	66
24. A histogram of the time distribution at which the 1600 Hz sine-Gaussian injections were made into the dummy on-source window of Trigger 2668, and rates at which they were recovered. 1200 injections are made at each injection amplitude, the loudest 600 of which are shown here in blue to be approximately uniformly distributed in time. Only 470 of these (in green) passed all of the pipeline cuts. We see repeating occurrences where the injections have a noticeably decreased probability of passing all the pipeline cuts, and this happens with approximate 224 s periodicity. We see the efficiency curves increase in Figure 25, and we also see the periodicity in injection recovery percentage vanish.	73
25. The efficiency curves of the 1600 Hz, elliptically polarized sine-Gaussian waveform injected into the off-source segment containing the most significant event (the ‘dummy on-source segment’) of trigger 2668. We use a dummy on-source for injection studies so that the sensitivity	

- can be maximized without viewing the results, and the efficiency curve shows the fraction of injections at each h_{rSS} of injection that are recovered with a higher significance than the loudest event in the dummy on-source. The plot on the left shows the efficiency curve when the pipeline is run with no uncertainty in the position of the magnetar, and we see that it asymptotic to approximately 0.9. On the right side we have the efficiency curve with 1 degree of uncertainty, and this efficiency rises to unity. 75
26. The p-values of the centered and delayed on-source searches plotted along with the cumulative probability of each p-value [14]. The dotted line indicates the expectation value for each p-value, and the shaded band indicates the region in which 90% of the p-values should fall. We note several analyses with p-value=1 in the centered search – this is the case because none of those on-source times contained loud clusters that survived the x-pipeline cuts. The lowest p-values in the delayed and centered searches are coming from Trigger 2653 and 2656 respectively, and are discussed in greater detail in Section 3.5. 81
27. Spectrograms of H1 data at the time of the loudest event in the delayed search over trigger 2653 (top) and at the time of a Omicron-identified glitch with a similar morphology (bottom) [14]. We see that in each case the event is accompanied by a loud burst of instrumental noise in the same approximate frequency range, and separated by .3s. The presence of glitches with such similar properties in the background data, at other points in the on-source, and at times before and after the event bolsters the idea that new class of instrumental artifact, the double-glitch, was present around the time of trigger 2653 and was detected during the delayed search. 94
28. Spectrograms of the loudest event in the centered search for both L1 (top) and H1 (bottom) [14]. The event is visible in L1 as a higher energy region of time-frequency space just below 1600Hz. No such high-energy region is readily visible in H1. We also see similar noise in L1 at lower frequencies both before and after the time of the event, which adds credence to it being a glitch in L1 only. We also see that the ambient noise at the time of the run is in a normal state. 96
29. A histogram of the ratio of sensitivities between the centered and delayed searches, as measured by the $h_{rSS}^{50\%}$ for each waveform common to both searches injected into each trigger analyzed by both searches. The median $h_{rSS}^{50\%}$ for the centered search is found to be 83% of its counterpart in the delayed search. 100

Figure	Page
30. The best 50% detection $h_{\text{rss}}^{50\%}$ of each waveform (from either SGR 1935+2154 or J1818.0-1607) included in both the centered and delayed searches, overlaid with the O3 sensitivity curves from Hanford and Livingston. These include both circularly and elliptically polarized sine Gaussians, and White Noise Bursts (here we show the WNB's of 11 s duration). In every case we see that the centered on-source search has better sensitivity.	101
31. The 50% detection $h_{\text{rss}}^{50\%}$ of several waveforms from O3 with their corresponding waveforms from O2, overlaid with the O3 sensitivity curves from Hanford and Livingston. For each waveform we present the lowest $h_{\text{rss}}^{50\%}$ value coming from either SGR 1935+2154 or J1818.0-1607. The waveforms marked by 'x' represent elliptically polarized sine Gaussians, of which there were none injected in O2.	104
32. This is the waterfall plot of the Lorimer burst showing the difference in arrival times of photons of different frequencies in the first-discovered Fast Radio Burst (FRB) [15].	108
33. A histogram of the posterior luminosity distance values of each FRB in the the Canadian Hydrogen Intensity Mapping Experiment (CHIME) FRB sample of 806 bursts [16]. Each of these luminosity distances has a very high uncertainty with the 90% credible interval commonly spanning hundreds of Mpc, making it difficult to prioritize which events to analyse. It should be noted that a very low percentage of these fall within the Advanced LIGO (aLIGO) detection range; the closest FRB in the sample is FRB 20190425A, for which the median distance is 133 Mpc, with a 90% confidence interval ranging from 13 Mpc to 386 Mpc.	116
34. An example output of the localization data provided by CHIME, including each of the sky localization islands [16].	117
35. The detection efficiency curves of one of the accretion disk instability (ADI) waveforms injected into FRB 37888771. The plot on the left is without autogating, and the plot on the right is with autogating. The ADI waveform is a long-duration waveform, and one which normally has sensitivity limitations due to short-duration transients. We see that when autogating is applied the efficiency curve is smoother and approaches unity faster, and we also see that it has lower values of h_{rss}^{50} and h_{rss}^{90} , meaning it has higher sensitivity as measured by this ADI waveform.	120

Figure	Page
36. The detection efficiency curves of the elliptically polarized sine Gaussian waveforms at 650 Hz. The top row is injected into FRB 37888771 and the bottom row is FRB 39069820. The left side plots are with no autogating, and the right side plots are with autogating applied. We see that at higher values of the h_{rss} injection amplitude there is a drop in the fraction of injections recovered in the autogated analyses. This is because the injections are loud enough such that the average energy over the 1 s span of time exceeds the autogating threshold in 1 detector but not in the other, and the injection is gated. The detection efficiency normally rises at even higher amplitudes because the autogating algorithm canceled if the energy requirement is met in multiple detectors.	122
37. The cumulative distribution of the p-values from all the analyses over both repeating FRBs and non-repeaters. We include the 90% band encompassing the range in which each p-value has a 90% chance of falling, numerically calculated [16]. There are two repeaters with p-values of 1; this indicates that no on-source events survived the pipeline cuts.	123
38. Histograms showing the $h_{\text{rss}}^{50\%}$ of the 1600 Hz elliptically polarized sine Gaussian waveform for both the non-repeaters (left) and the repeaters (right). The search over repeaters generally has lower values of $h_{\text{rss}}^{50\%}$, and so is a more sensitive search as measured by this waveform.	125
39. Histograms of the distributions of significance values of all clusters from x-pipeline runs on triggers 2669, 2670, and 2671 from [1], all of which were from an unidentified source. The different distributions represent the percentile of pixels in a time-frequency map that the pipeline considers to be bright enough to be included in the clusters, and we plot the distributions of brightness cutoffs between 1 percent and 5 percent. In these distributions we only consider clusters with central frequencies between 1000 and 3000 Hz, and use timesteps of $\frac{1}{2^N}$, where $2 \leq N \leq 7$	143
40. A plot of the sensitivities of the searches on four different magnetar triggers in O3 done at four different superdecimate rates ranging from $\frac{1}{10}$ to $\frac{1}{3}$. The sensitivity is standardized by the $h_{\text{rss}}^{50\%}$ of the ringdown waveform at 1590 Hz with damping time 100 ms. The superdecimate rate is a parameter of x-pipeline which determines the rate at which the clusters are allowed to appear in the data. The standard x-pipeline runs are done with a superdecimate rate of $\frac{1}{4}$, meaning that there is 1 cluster per 4 seconds of data on average, but that the clusters need not be	

Figure	Page
uniformly distributed in time. The mean sensitivities for each trigger across all superdecimate rates are plotted as dashed lines.	146
41. We plot the evolution of the distribution of stacked significances with the number of triggers in the stack ranging from 1 to 57. The frequency bins are 100 Hz wide and span from 1-3 kHz, with their index given on the left of each subplot. Time bins are 5 s in duration, with their index on the horizontal axis. For the purpose of saving computing resources, for this preliminary study we use background segments from the delayed short-duration search over Trigger 2656 described in Chapter 3.3, and stack them as though they were independent triggers. We see that the total significance of the stacks tend toward a mean significance as more triggers are added, and we also see that certain frequency bins have disproportionately high significance.	147
42. Histogram of the significance values of the clusters generated by the runs on triggers 2652, 2653, and 2654 before stacking, between 1500 and 1600 Hz. The overlap of these distributions shows that the significance of the clusters in the x-pipeline output is independent of the sensitivity of the detector network. Trigger 2653 has fewer clusters because it has less background time available, and a higher percentage of its clusters could fall in a frequency bin not shown here. We also see an overpopulation of clusters with significance approximately 10 in trigger 2652; this could be caused by a specific type of glitch being more common in the background of that analysis, and might become a source of noise for the stacked search.	150
43. Histograms of the significance of the stacked triggers without weighting. The original x-pipeline runs are over a frequency range of 1500-1900 Hz at a cluster rate of 1 per 4 s, and these histograms show the triggers in the 1500-1600 Hz bin. We include the histogram for 2, 5, 9, and 17 triggers in the stack, and we see that the distribution moves to higher significance as more triggers are added to the stack.	152
44. Histogram of the significances with 17 triggers in the stack, shown with smaller histogram bin width. There are periodic spikes at lower significance, but the higher significance part of this distribution is relevant for this analysis.	153
45. The mean significance required of the unstacked triggers for their stacked counterpart to have a specific p-value, 1×10^{-3} or 5×10^{-4} . The mean significance reduces with more triggers in the stack. This data is also displayed in Table 16.	154

Figure	Page
46. Histogram of the significance values of the clusters generated by the runs on triggers 2652, 2653, and 2654 before stacking, weighted by the network sensitivity. The distributions of sensitivity separate according to network sensitivity, and the total range of sensitivities increases over the unweighted case shown in Figure 42.	157
47. Histograms analogous to the ones shown in Figure 43, but with the significances weighted according to the sensitivity of the detector network. We see a similar result as in the unweighted case; the distributions move to higher significance with more triggers in the stack. There is also more distinct broadening of the distributions with more triggers. This is because the range of significance values of the unstacked triggers is wider in the weighted case, as evidenced in Figure 46.	158
48. The mean significance required of the unstacked triggers for their stacked counterpart to have a specific p-value, 1×10^{-3} or 5×10^{-4} , when weighted according to network sensitivity. The weighted case is denoted by triangles, and is consistently somewhat higher than the unweighted case. This is to be expected when the sensitivity distributions spread out with weighting.	159
49. Histograms of the significances with 17 triggers in the stack, shown with smaller histogram bin width. There are periodic spikes at lower significance, but the higher significance part of this distribution is relevant for this analysis.	160
50. We plot the equations of best fit describing the relationship between the mean significance needed to achieve a specific p-value, and the number of triggers in the stack. We do this for both $p = 1 \times 10^{-3}$ and $p = 5 \times 10^{-4}$, and overlay it with the calculated mean significance for each stack size. The fit is done assuming that the mean significance (S) can be reasonably well-described by $S = b + m \times N^{-a}$, where b , m , and a are constants, and N is the number of triggers in the stack. . . .	165

LIST OF TABLES

Table	Page
<p>1. The frequencies of the 2nd order violin modes in O3. These are measured in Hz and entries of ‘-’ indicate that the value is not known. The reason that the frequencies of specific violin modes are not known is that they are not routinely rung up and sources of noise in DARM, so their frequencies are not obvious to spot. Notice also the proximity of certain modes on the same test masses, specifically modes 2 and 3 on ITMY.</p>	58
<p>2. List of bursts considered for the search</p>	65
<p>3. Parameters used in the centered on-source and delayed on-source short-duration searches. When no value is specified, the search was run with the default parameters, including frequency ranging from 50-4000 Hz, a symmetric background window 10800s in length, and 0 degree error region. The background asymmetry factor is defined as the fraction of the background time before the burst time, with 0.5 corresponding to a symmetric background. The error region is defined as the 1σ uncertainty in the sky position of the source. Using a non-zero error region on a point source can sometimes increase the search sensitivity because it counters the effects of the earth’s rotation during the on-source window.</p>	74
<p>4. On-source, off-source and frequency range of searches performed. The off-source interval is centered around the magnetar burst time.</p>	76
<p>5. The resulting FBS and p-values from both the short-duration and long-duration searches [14]. A p-value of 1 indicates that there were no clusters in the on-source window that survived the veto cuts. x-pipeline constrains the number of loud clusters it can generate to a rate of 1 cluster per 4 s, meaning that it is more probable for a shorter on-source window not to have any surviving clusters. Table entries of ‘-’ indicate that no value is recorded, because no search was run. Bursts 2669-2671 are from the magnetar with no identified source, and the long-duration search was not conducted on these. Bursts 2651 and 2665 were missing segments of data from the on-source window such that the short-duration searches could not run, and burst 2671 had data missing in the delayed on-source window such that the delayed on-source search could not be run.</p>	80

6. The central frequencies and damping times are shown for each of the waveforms used in the centered on-source search. We also show the most constraining $h_{\text{rss}}^{50\%}$ for each waveform considering only bursts from Swift J1818.0-1607 (J1818.0-1607), and calculate the corresponding $E_{\text{GW}}^{50\%}$ using Equation 3.7 (and Equation 3.8 for the white noise bursts (WNBs)) assuming a source distance of 4.8 kpc [17]. We also provide the corresponding ratios of gravitational wave energy to electromagnetic (EM) energy, using the isotropic energies given in Table 2. All waveforms have elliptical polarization except for those marked by *, which are circularly polarized, and the WNBs, which have isotropic polarization. 84
7. The central frequencies and damping times are shown for each of the waveforms used in the centered on-source search. We also show the most constraining $h_{\text{rss}}^{50\%}$ for each waveform considering only bursts from SGR 1935+2154, and calculate the corresponding $E_{\text{GW}}^{50\%}$ using Equation 3.7 (and Equation 3.8 for the WNBs) assuming a source distance of 9 Kpc [18]. We also provide the corresponding ratios of gravitational wave energy to EM energy, using the isotropic energies given in Table 2. All waveforms have elliptical polarization except for those marked by *, which are circularly polarized, and the WNBs, which have isotropic polarization. 85
8. The central frequencies and damping times are shown for each of the waveforms used in the centered on-source search. We also show the most constraining $h_{\text{rss}}^{50\%}$ for each waveform considering only bursts from the unknown source, and calculate the corresponding $E_{\text{GW}}^{50\%}$ using Equation 3.7 (and Equation 3.8 for the WNBs) assuming a source distance of 3.8 kpc [19]. We also provide the corresponding ratios of gravitational wave energy to EM energy, using the isotropic energies given in Table 2. All waveforms have elliptical polarization except for those marked by *, which are circularly polarized, and the WNBs, which have isotropic polarization. 86
9. The central frequencies and damping times are shown for each of the waveforms used in the delayed on-source search. We also show the most constraining $h_{\text{rss}}^{50\%}$ for each waveform considering only bursts from the J1818.0-1607, and calculate the corresponding $E_{\text{GW}}^{50\%}$ using Equation 3.7 (and Equation 3.8 for the WNBs) assuming a source distance of 4.8 kpc [17]. We also provide the corresponding ratios of gravitational wave energy to EM energy, using the isotropic energies given in Table 2. All waveforms have elliptical polarization except for those marked by *,

Table	Page
which are circularly polarized, and the WNBs, which have isotropic polarization.	87
10. The central frequencies and damping times are shown for each of the waveforms used in the delayed on-source search. We also show the most constraining $h_{\text{rss}}^{50\%}$ for each waveform considering only bursts from the SGR 1935+2154, and calculate the corresponding $E_{\text{GW}}^{50\%}$ using Equation 3.7 (and Equation 3.8 for the WNBs) assuming a source distance of 9 Kpc [18]. We also provide the corresponding ratios of gravitational wave energy to EM energy, using the isotropic energies given in Table 2. All waveforms have elliptical polarization except for those marked by *, which are circularly polarized, and the WNBs, which have isotropic polarization.	88
11. The central frequencies and damping times are shown for each of the waveforms used in the delayed on-source search. We also show the most constraining $h_{\text{rss}}^{50\%}$ for each waveform considering only bursts from the unknown source, and calculate the corresponding $E_{\text{GW}}^{50\%}$ using Equation 3.7 (and Equation 3.8 for the WNBs) assuming a source distance of 3.8 kpc [19]. We also provide the corresponding ratios of gravitational wave energy to EM energy, using the isotropic energies given in Table 2. All waveforms have elliptical polarization except for those marked by *, which are circularly polarized, and the WNBs, which have isotropic polarization.	89
12. The gravitational wave energy at 50% detection efficiency for every analysis included in the centered on-source search. We include the ratio of the gravitational wave energy upper limit to the isotropic EM energy for the triggers for which the EM energy is known. We specifically present the energies pertaining to the elliptically polarized 1600 Hz sine Gaussian waveform, and the 1590 Hz ringdown waveform with 100 ms damping time. The parameters of each of these waveforms make them plausible representations of gravitational wave (gravitational wave) from excited fundamental oscillation modes (f -modes). The burst numbers are consistent with those used in [1].	90
13. Upper limits for root sum square of the integrated GW strain (h_{rss}) and gravitational-wave energy (E_{GW}) for both the half sine-Gaussian and ringdown waveforms at both 150 Hz and 750 Hz. We present the burst with the most sensitive upper limits from each source, which were trigger 2656 from SGR 1935+2154, and trigger 2674 from Swift J1818.0-1607. No long-duration analysis was run on the unknown source.	97

Table	Page
14. Details of the 11 repeating FRBs events provided by CHIME[16]. Repeaters are determined by the CHIME events with the same sky positions and dispersion measure (DM). The detector network indicates the detectors that were in observing at the time of the FRB; V1 = Virgo, H1 = Hanford, and L1 = Livingston. For FRB 20190518A and its associated repeats, we list only the distance of the source as obtained by galaxy localization [20]. There are no islands of sky position on these events by virtue of being repeated events from the same source.	118
15. We show the percent change in sensitivity as measured by the $h_{\text{rss}}^{50\%}$ of the 100 ms ringdown waveform at central frequency 1590 Hz when comparing the runs at the most and least sensitive superdecimate rate. For trigger 2652 this change is 15.1%, and specifically there is an outlier superdecimate rate of $\frac{1}{4}$ which reduces the sensitivity of this run. The other superdecimate rates yield a nearly constant sensitivity for trigger 2652. The other triggers have very negligible differences in their sensitivities when run with different superdecimate rates.	145
16. We show the mean significance needed in the unstacked triggers to give stacked p-values of 5×10^{-4} and 1×10^{-3} for all numbers of triggers in the stack ranging from 2 to 17. The values for 1 trigger in the stack are obtained through the normal x-pipeline post-processing stage of analysis, and include no stacking.	156
17. We show the $h_{\text{rss}}^{50\%}$ of two individual triggers, 2655 and 2656, which corresponds to the mean unstacked significance needed to make a detection of a stacked trigger with $p = 5 \times 10^{-4}$. We see a reduction in the $h_{\text{rss}}^{50\%}$ in both cases. An entry ‘-’ indicates that the post-processing was not completed.	163

CHAPTER I

INTRODUCTION

1.1 Forward

This dissertation encompasses the work that I've done as a graduate student at the University of Oregon between September of 2017 and April of 2023. For the 20 years preceding my graduate school career, experimental gravitational-wave science was considered to be an engineering problem, with the first detection of an actual event in 2015, exactly a century after General Relativity was first theorized. The first binary neutron star merger was detected in August of 2017, a month before I entered grad school.

Since that time we've made both instrumental and software advances that have allowed us to reach sensitivities such that a binary neutron star merger can be detected with signal-to-noise ratio of 8 at up to 200 Mpc. We have detected tens of gravitational-wave events, the most distant of which was likely created at a similar time as our sun.

The third observing run (O3) of Advanced LIGO and Advanced Virgo was punctuated by several types of electromagnetic bursting events: Fast Radio Bursts (FRBs), Gamma-Ray Bursts (GRBs), and magnetar x-ray flares. One of the challenges of O3 was to develop and run searches on these events to optimize the probability of detecting a gravitational wave in conjuncture with one of them, in the hopes of constraining the astrophysics of the burst. The summary of my Ph.D. research was attempting to increase the sensitivity of these searches.

I spent nine months total as a LIGO Scientific Collaboration (LSC) fellow at LIGO Hanford Observatory (LHO) between 2018 and 2019. During that time I designed a feedforward filter to remove noise from the Power Recycling Cavity Length (PRCL) that was coupling into the Differential Arm length (DARM), and implemented it to gain sensitivity in the detector. I also searched for a cause of the glitches in the Arm Length Stabilization (ALS) fiber and showed that they were likely mechanical disturbances, but not linked to the outdoor humidity or rain. I also spent significant effort designing filters to damp violin modes, and wrote code that calculates coherence between auxiliary channels and DARM, and posts plots to the F-scan pages. I also participated in the O3 upgrades for the physical environmental monitoring channels and equipment, and ran noise injection studies.

I joined the burst group in 2019 by running x-pipeline on GRB triggers for the O3 GRB papers. From there I co-managed the O3 Magnetar search, and served on the paper writing team for the FRB paper from the first half of the third observing run of Advanced LIGO and Advanced Virgo (O3a). Although none of these papers are able to claim a detection, the magnetar and FRB papers do set historically sensitive upper limits.

The O3 observing run was populated with bursts from repeated sources in both the magnetar and FRB searches. Furthermore, it has recently been shown that one of the magnetars in our study, SGR 1935+2154, has windowed periodicity in its flare times. This means that if we see flares from it during the fourth observing run of Advance LIGO and Advanced Virgo (O4), there will very likely be a large cluster of them. This was the motivation to start a branch of x-pipeline that can analyze the data from many bursts simultaneously, rather than just burst-by-burst. We develop a motivation for this new ‘stacking’ pipeline, go through

the statistics of what its potential for detection is, and present some preliminary sensitivity studies that indicate that with a proper choice of search parameters, we could be more sensitive to a lower signal-to-noise ratio gravitational-wave event, as long as one were consistently accompanying each electromagnetic burst.

1.2 Introduction to Magnetars

Magnetars are neutron stars with exceptionally strong external dipole magnetic fields, on the order of $10^{14} - 10^{15}$ G, and potentially stronger internal magnetic fields [21]. There are 30 known magnetars to date, 28 of these are located within the Milky Way Galaxy, and 2 are in the Magellanic Clouds. These magnetars have displayed a wide range of phenomena, including x-ray bursts with energies of $\approx 10^{42}$ erg, x-ray ‘giant flares’ with energies as high as $\approx 10^{46}$ erg, and glitches and anti-glitches characterized by abrupt changes in the rotational angular velocity. The frequency range of emission seems to be star-dependent and variable, with some magnetars seen to emit bursts of soft gamma rays, and six of them have also emitted in radio frequencies. With such a wide range of possible behaviors and each of them only represented in a subset of the known magnetars, it is reasonable to explore the development of the magnetar model as an explanation for its encompassing stars. For the remainder of this dissertation, we will use the terms *x-ray flare* and *x-ray burst* interchangeably, as both are commonly seen in the literature.

The late 1970’s through the mid 1990’s saw the emergence and development of two seemingly independent phenomena, that of Soft Gamma Repeaters (SGRs) and Anomalous X-ray Pulsars (AXPs). The first x-ray bursts from an SGR (which included a giant flare) were detected in 1979 from the Dorado region of the Large

Magelanic Cloud [22]. Periodic pulsations in the tail of the giant flare as well as coincident sky localization with supernova remnant N49 evidenced a neutron star as the source of the bursts, where the periodic pulsations were attributed to the rotational period of the star [23]. This magnetar is now known as SGR 0526-66. These bursts were joined by those from SGR 1900+14 and SGR 1806-20 over the next decade.

The strong magnetic fields in SGRs were hypothesized as a way of reconciling the association of SGR 0526-66 with a supernova remnant and its long (8 s) spin period [24, 25]. Surface magnetic fields of magnitude $10^{14} - 10^{15}$ G are needed to slow the magnetar from newly-born remnant rotational periods to typical SGR rotational periods within the typical lifetime of a supernova remnant, assuming the slowing is due to magnetic dipole braking, and such magnetic fields also provide sufficient energy to power the SGR bursting behavior. This theory was bolstered in 1998 and 1999, when the first direct measurements of the spin-down velocity were made on known magnetars SGR 1806-20 and SGR 1900+14 [26, 27], and the corresponding magnetic field strengths fell within the hypothesized range.

The 1980's also saw the detection of bright x-ray bursts with seconds-long pulsation periods from supernova remnant CBT 109[21], as well as similar x-ray bursts from sources 1E 1048.1-1537 and U 0142+61, which lack any supernova connection [28]. These were coined 'Anomalous X-ray Pulsars' (AXPs), and were soon joined with several other detections, all with spin periods between 6 and 12 s. It was suggested in 1996 that AXP's might be related to SGR's [25], but it was not until 2002 that a burst of soft gamma rays was detected from an AXP [29, 30]. There have since also been x-ray bursts detected from SGR's, and the

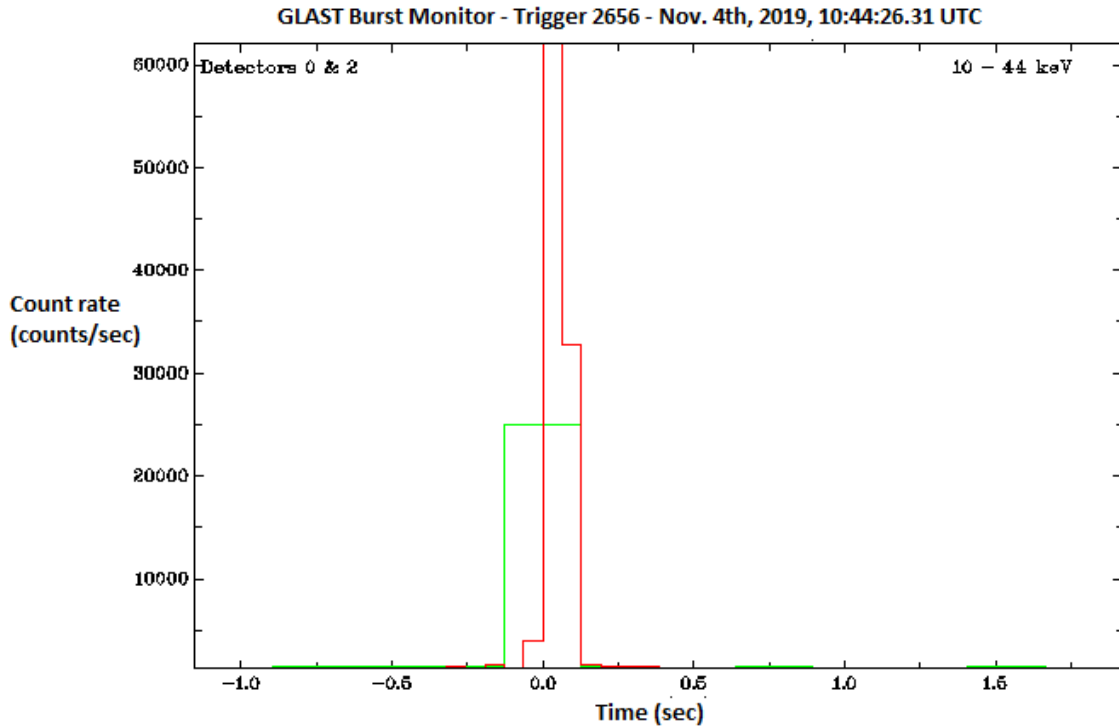


FIGURE 1. A lightcurve for magnetar x-ray trigger 2656 (naming convention consistent with that of [1]) from SGR 1935+2154. The majority of photons fell in the 10-44 keV energy range, and we show histograms of the photon count rates in two of the channels in red and green [2].

term ‘magnetar’ now applies to all SGR’s and AXP’s. A lightcurve from one such x-ray burst is shown in Figure 1.

One leading model of magnetar flares is crust cracking, wherein the crust experiences extreme pressure due to twisting of the magnetic field just before a magnetic reconnection event [24, 31]. The crust then experiences a brittle crack, which can then couple into quasi-normal oscillatory modes in the star. This model has been compared with earthquake models, and depends on the properties of the neutron stars, including the equation of state, the magnetic field strength, and the matter composition of the crust.

The catalogue of known magnetars was first published in 2014 [19] and is kept up-to-date. These magnetars produce x-ray pulsations with periods matching their spin periods, which range from 2 to 12 s. The spin-down timescales, $\frac{P}{\dot{P}}$ are on the order of 1000 years, indicating a young magnetar population. The short end of the spin period distribution corresponds to the youngest magnetars (they are all spinning down), and the longest burster spin period (12 s) might provide some limits on the lifetime during which a magnetar still retains its bursting properties. More evidence for magnetars' youth comes in their detection strictly no more than 20-30 pc from the galactic plane. Assuming velocities consistent with the kick velocity of a core collapse supernova event, the distance from the galactic plane implies ages of no more than 10^5 years [21, 32].

Several new and exotic behaviors have been observed in specific magnetars over the last few years, making them a particularly highly scrutinized area of modern astrophysics. In particular, on April 28th, 2020, a Fast Radio Burst (FRB) was observed in coincidence with an x-ray flare from SGR 1935+2154, a day after a flare storm from the same magnetar[33]. Although leading models had already pinned magnetars as likely progenitors of at least a subset of repeating FRBs, the coincident flare and FRB proved to be the smoking gun that linked these two phenomena. The connection between magnetars and FRBs is covered in more detail in Chapter 4.1. SGR 1935+2154 is also particularly interesting because it is the only magnetar to date that has demonstrated Periodic Windowed Behavior (PWB), a phenomenon by which x-ray flares can only happen in a specific active phase of a repeated period of time [34].

If any of these magnetar phenomena excite non-radial modes of oscillation (f -modes, r -modes, w -modes, g -modes, Alfven modes, etc.) then gravitational

waves would be produced, and their detectability depends on the parameters of the system, as well as the sensitivity of the gravitational-wave detector network in the frequency band of emission. These modes are discussed in greater detail in Chapter 3.1.

One phenomenon worth discussing in relation to the properties of gravitational waves are the Quasi-Periodic Oscillations (QPOs) that have been observed in the tails of the EM data of giant flares, shown in Figure 2. While only a few giant flares have been observed to date, quasi-periodic oscillations (QPOs) have been observed from 18 Hz to 2380 Hz during these first few hundred seconds following the giant flares. Some theories correlate the QPOs to torsional modes in the magnetar’s crust, and while the torsional modes themselves are unlikely to radiate gravitational waves, it is possible that they can couple into different oscillatory modes with more observable parameters. One such mode is the f -mode, which we now discuss in more detail.

1.3 The fundamental pressure mode of a neutron star

The oscillatory mode of a neutron star’s core thought to have the strongest coupling to gravitational waves is the f -mode. The properties of the f -mode and of its resulting gravitational wave emission are largely dependent on the equation of state (EOS) of the neutron star, which is very much unknown. The only previous gravitational wave study on tidal deformability of neutron stars comes from an analysis of GW 170817, and puts the f -mode gravitational wave frequency very loosely at ≈ 2 kHz [35]. This is somewhat higher than the most sensitive bands of the LIGO and Virgo detectors, and might be better suited to a gravitational wave search with kHz-specific facilities such as the proposed Neutron Star Extreme

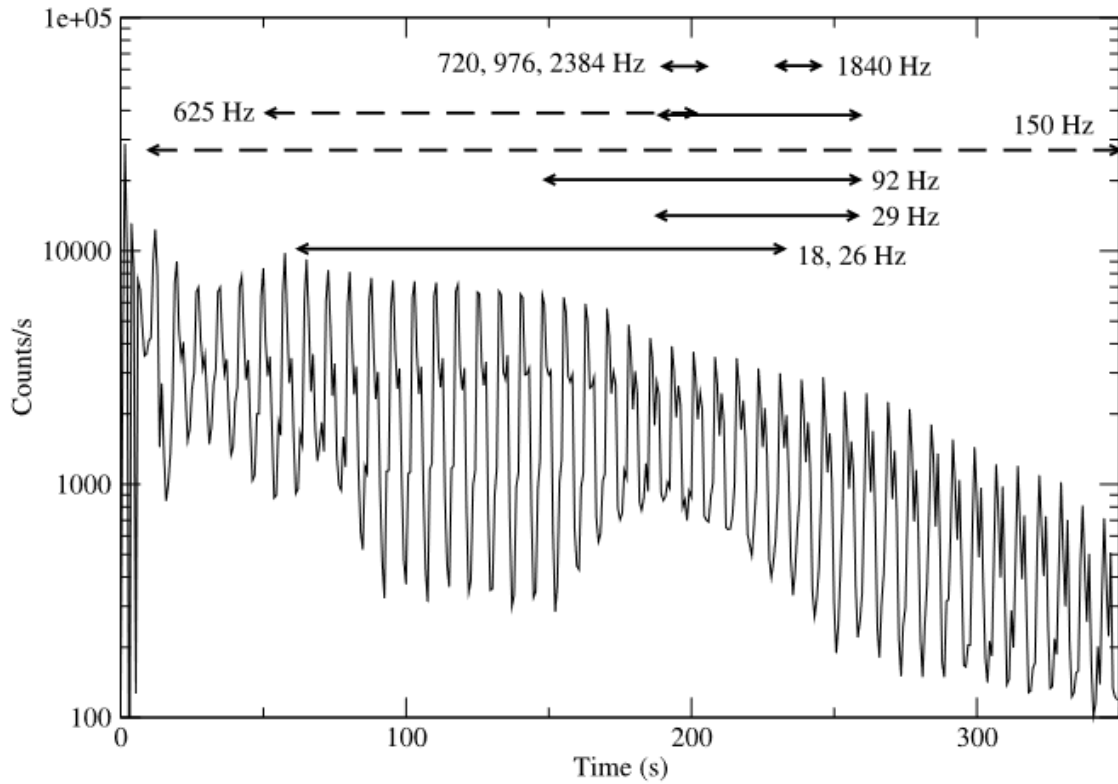


FIGURE 2. The QPOs observed in the 2004 giant flare from SGR 1806-20 [3]. The excited frequencies of oscillation range from 18 Hz to 2384 Hz, and are detected for tens to hundreds of seconds in the first 300 s after the giant flare. The rotational period of SGR 1806-20 is 7.548 s, which matches the most prominent oscillation in this plot. It is also important to note that the scaling is chosen to show the QPOs, and the initial burst is off the plot.

Matter Observatory (NEMO) [36]. Here we discuss different theoretical models and properties of the f -mode.

The f -mode frequency is proportional to the density of a neutron star [37], and for uniformly dense stars in the Newtonian limit, this frequency is given by:

$$\omega^2 = \frac{2l(l-1)}{2l+1} \frac{GM}{R^3}, \quad (1.1)$$

where M and R are the mass and radius of the star, and $l = 2$ when the star is described by spherical harmonic functions. This is a reasonable approximation in the relativistic case [38].

An initial 1998 study of the properties of the f -mode oscillation in canonical neutron stars assumed that the eigen-frequency was proportional to the square-root of the mean density, and calculated it assuming 12 different realistic equations of state, for a wide range of densities [39]:

$$.03 \leq \left(\frac{\bar{M}}{\bar{R}^3} \right)^{\frac{1}{2}} \leq .08 \quad (1.2)$$

where \bar{M} and \bar{R} are dimensionless measures of mass and radius given by $\bar{M} = \frac{M}{1.4M_\odot}$ and $\bar{R} = \frac{R}{10\text{km}}$. When the f -mode frequencies (numerically calculated from a fully general relativistic framework) are plotted against the mean stellar density, we do see some deviations for each EOS. However, it is possible to make a linear approximation of the f -mode frequency, in kHz, that is approximately valid for all 12 equations of state [39]:

$$F \approx .78 + 1.635 \times \left(\frac{\bar{M}}{\bar{R}^3} \right)^{\frac{1}{2}}. \quad (1.3)$$

If we then assume a $1.4M_{\odot}$ neutron star with a 10 km radius, this implies an f -mode frequency of 2.4 kHz. The corresponding damping time can be calculated using the quadrupole formula, Equation 2.33, for the appropriate system parameters:

$$\tau_f = \frac{\text{oscillation energy}}{\text{GW power}} \approx R \left(\frac{R}{M} \right)^3. \quad (1.4)$$

The authors numerically generate values of $\frac{R^4}{\tau_f M^3}$ for varying values of the stellar compactness, $\frac{\bar{M}}{R}$, for each of the 12 equations of state. Regardless of the true equation of state of the magnetar, they find an approximate relation between the inverse damping time (in seconds) and the stellar compactness to be:

$$\frac{1}{\tau_f} \approx \frac{\bar{M}^3}{R^4} \times \left(22.85 - 14.65 \frac{\bar{M}}{R} \right). \quad (1.5)$$

A similar analysis was performed in 2004, using nine different, new equations of state [40]. The subatomic properties of neutron star interiors were considered, and the f -mode frequency (kHz) was approximated for these equations of state for neutron star densities of $\rho > 2 \times 10^{14} \frac{g}{cm^3}$ as:

$$F \approx a + b \times \sqrt{\frac{M}{R^3}}, \quad (1.6)$$

where:

$$a = 0.79 \pm 0.09 \quad (1.7)$$

$$b = 33 \pm 2 \quad (1.8)$$

and a is measured in kHz and b is measured in $\text{km} \times \text{kHz}$. The damping time is approximated by:

$$\tau_f(s) \approx \frac{R^4}{cM^3} \times \left(a + b \frac{M}{R} \right)^{-1} \quad (1.9)$$

where a and b are:

$$a = 8.7 \pm .2 \quad (1.10)$$

$$b = -.271 \pm .009. \quad (1.11)$$

These relations indicated a somewhat lower frequency of f -mode oscillation, which physically is merely a reflection of the EOSs being somewhat less compressible than those previously considered. More significantly, the difference in the frequency range of the f -mode as approximated by nine EOSs as opposed to 13 EOSs shows that the inferred properties of the star (mass, radius) could be incorrectly constrained if the range of EOSs is not sufficiently inclusive [41].

In an attempt to avoid too many assumptions about a neutron star's EOS, a 2010 study looked at gravitational waves produced by excited f -modes in both neutron stars and quark stars in terms of the moment of inertia I of the star, by introducing a dimensionless quantity $\eta = \sqrt{\frac{M^3}{I}}$ [42]. This study used numerical simulations with nine realistic EOSs for neutron stars as well as two quark star equations of state to plot both ω_r and ω_i in terms of η , where ω_r and ω_i are the real and imaginary components of a complex f -mode eigen-frequency, $\omega = \omega_r + i\omega_i$. The f -mode has exponential decay with time constant $\tau = \frac{1}{\omega_i}$. All of the equations of

state were well-described by the lines of best fit:

$$M\omega_r = -0.0047 + 0.233\eta + 0.0575\eta^2 \quad (1.12)$$

$$\frac{I^2\omega_i}{M^5} = -0.00694 + 0.0256\eta^2. \quad (1.13)$$

If a gravitational wave were observed such that ω_i and ω_r could be extracted, then I and M could be inferred through Equation 1.12. The radius can then also be inferred through [43]:

$$\tilde{I} = 0.237(1 + 4.2x + 90x^4) \quad (1.14)$$

where

$$\tilde{I} = \frac{I}{MR^2} \quad (1.15)$$

$$x = \frac{M}{R} \quad (1.16)$$

and M is measured in solar masses and R is in km.

A 2001 study [44] of the gravitational-wave energy budget available to the f -mode was based on a global reconfiguration of the internal magnetic field during a giant flare, and set a framework for future energy budget studies. The properties of the 1998 giant flare from SGR 1900+14 [45, 46] included a 230% increase in the spin-down rate of the magnetar [47], which suggests either variable angular momentum or moment of inertia. This study assumes changes in the moment of inertia caused by a reconfiguration of the internal magnetic field consistent with the observed properties of the 1998 giant flare. They assume an internal magnetic field

of $B \geq 10^{16}$ G, and polytropic equations of state given by:

$$p = K \rho^{1+\frac{1}{n}} \quad (1.17)$$

where K is a constant, ρ is the local density of the neutron star, and n is the polytropic index which is chosen to be half-integer values ranging from 1 to 2.5. They compare different stable configurations of the magnetar, and are able to explain both the release of electromagnetic energy ($\geq 10^{44}$ erg) and change in spin-down rate by a hydrodynamic deformation of the star from a prolate to a more spherical shape, without requiring a large reduction in the magnetic energy of the star. The energy released in gravitational waves in this model would be set by the spin-down rate increase. For typical neutron star properties and assuming the f -modes are principally damped gravitationally with a damping time of 100 ms, a characteristic gravitational-wave amplitude is approximated in this model by:

$$h_c = 5 \times 10^{-21} \left(\frac{E_{gw}}{10^{47} \text{ erg}} \right) \left(\frac{f}{2 \text{ kHz}} \right) \left(\frac{d}{5 \text{ kpc}} \right) \quad (1.18)$$

where E_{gw} is the energy released in gravitational waves, f is the f -mode frequency, and d is the distance to the source. This initial 2001 approximation yielded optimistic prospects for the then-future LIGO and Virgo detectors; the implication was that such an event at less than about 5 kpc would be observable.

The internal magnetic field rearrangement model used in [44] was motivated largely by the discontinuous spin-down rate surrounding the 1998 giant flare, a property that has not consistently accompanied other giant flares or more energetically typical x-ray flares. A 2011 study [48] investigated the total energy budget available in a SGR flare by following similar methods to the 2001 study [44],

but with much less restrictive assumptions, specifically allowing the magnetic field to provide energy to the gravitational waves. The gravitational wave energy budget derived in this manner ranged from $10^{48} - 10^{49}$ erg.

A study the following year performed non-linear general-relativistic simulations to determine the dependence of the gravitational-wave luminosity on the magnetic field strength, assuming that a giant flare is accompanied by a rearrangement of a magnetar's internal magnetic field [49]. The models assumed $n = 1$ polytropic, 1.3 solar mass neutron stars 15 km in radius. The polar surface magnetic field amplitudes ranged from 3.5×10^{15} G to 5.5×10^{16} G. A power-law fit to the gravitational-wave amplitude of the models at each magnetic field strength gives the relation:

$$h \approx 1.1 \times 10^{-27} \times \left(\frac{10 \text{ kpc}}{d} \right) \times \left(\frac{B_{pole}}{10^{15} \text{ G}} \right)^{3.3} \quad (1.19)$$

where d is the distance to the source and B_{pole} is the magnetic field strength at the magnetar's pole. The authors note that most of this gravitational wave energy is radiated by the f -mode oscillation. Assuming a damping time of 100 ms, a corresponding gravitational-wave energy and magnetic field relation is given by [49]:

$$E_{gw} \approx 1.5 \times 10^{36} \left(\frac{B_{pole}}{10^{15} \text{ G}} \right)^{6.5} \text{ erg} \quad (1.20)$$

giving the f -mode detectability a high dependence on the magnetic field strength, and implying a gravitational-wave energy to electromagnetic energy ratio of:

$$\frac{E_{GW}}{E_{EM}} \approx 10^{-6}. \quad (1.21)$$

For magnetars with magnetic fields of $B_{pole} \approx 10^{15}$ G, the maximum gravitational wave strain emitted by a giant flare at 10 kpc (assuming a reconfiguration of the internal magnetic field) is 10^{-25} , making magnetar flares dim prospects for gravitational wave observation with current observatories.

This study was expanded upon with more detailed models including more general polytropes and a full range of mass and radius values to approximate a maximum cross-polarization amplitude of the gravitational-wave strain of the f -mode[50]:

$$h_x^{\max} = 8.5 \times 10^{-28} \left(\frac{10\text{kpc}}{d} \right) \left(\frac{R}{10\text{km}} \right)^{4.8} \left(\frac{M}{M_{\text{solar}}} \right)^{1.8} \left(\frac{B_{\text{pole}}}{10^{15}\text{G}} \right)^{2.9} \quad (1.22)$$

which, when assuming a damping time of 100 ms, corresponds to a gravitational-wave energy of:

$$E_{GW} = 1.7 \times 10^{36} \left(\frac{10\text{kpc}}{d} \right) \left(\frac{R}{10\text{km}} \right)^{9.6} \left(\frac{M}{M_{\text{solar}}} \right)^{3.6} \left(\frac{B_{\text{pole}}}{10^{15}\text{G}} \right)^{5.8}. \quad (1.23)$$

This provides a similar grim outlook on the prospects of detecting gravitational waves associated with an excited f -mode during a magnetar giant flare assuming a reconfiguration of the internal magnetic field.

The unexpected upshot of this study was a possibility of detecting lower-frequency (tens to hundreds of Hz) gravitational waves associated with the Alfvén modes inside the star, if they were to become excited. It is not obvious that they correlate with the QPOs observed in the tails of giant magnetar flares, and the properties (damping time, frequency, damping mechanism) are not well enough established to design a specific search for gravitational waves that targets them. But if there is any correlation with the QPOs in the tails of giant flares, then a

search that is broadly sensitive to lower-frequency, longer-duration signals after the time of the flare is sufficiently motivated.

The primary goal of this dissertation work is to increase the sensitivity of the current LIGO and Virgo searches to include the regions of parameter space in which one might expect to find a gravitational wave associated with an excited quasi-normal mode of oscillation in a magnetar. We focus specifically on the f -mode oscillation around the times of the magnetar x-ray flares in O3, and the FRBs during O3a.

1.4 Organization of Thesis

This thesis is organized as follows: In Chapter II we introduce the basics of general relativity and the theory behind gravitational wave detection. We then discuss the basic principles of interferometry, and the mechanics of the LIGO observatories. We introduce the basic improvements to Advanced LIGO to increase sensitivity: power recycling, signal recycling, and squeezing. I spent three quarters as a LSC fellow at the LHO, during which time I helped with Physical Environmental Monitoring upgrades and noise studies, and helped with commissioning projects aimed at increasing the detector's sensitivity and duty factor. In Chapter 2.4 we discuss a study of problematic instrumental artifacts in the Alignment Sensing and Control (ALS) system which were inhibiting an efficient transition between commissioning the detector and bringing it to a state where usable data could be taken. In Chapter 2.5 we discuss feedforward filters designed to mitigate noise coupling from specific systems into the gravitational-wave data. In Chapter 2.6 we discuss artifacts in the gravitational-wave spectrum due to the oscillations of the test masses, and ways of mitigating this noise.

In Chapter III we discuss the search for gravitational waves coincident with x-ray flares from galactic magnetars SGR 1935+2154 and Swift J1818.0–1607 during the third observing run of Advanced LIGO and Virgo. This was a two-part search for both long and short-duration gravitational waves retaining the properties theorized by the electromagnetic observations of quasi-periodic oscillations in the tails of giant flares, and hypothesis of f -modes being excited in the magnetar’s core. We discuss the differences between the search methods used in the second observing run (O2) and O3, and give a qualitative analysis of the gains in sensitivity. This research became a LIGO-Virgo-KAGRA collaboration paper [14].

Chapter IV handles the search for gravitational waves coincident with FRBs that happened during the first half of the third LIGO-Virgo observing run, O3a. We searched a subset of the FRBs in that time-period, which were selected for characteristics that would increase GW detectability, assuming short-duration gravitational waves consistent with the theoretical predictions given by both repeating and non-repeating FRB theories. This research also resulted in a collaboration paper, [16].

In Chapter V we introduce a new search method for lower-amplitude but consistently-present gravitational waves that are coincident with electromagnetic sources, specifically flaring magnetars. This is a modification to x-pipeline [51, 52], an existing GW search pipeline to enable a method of ‘stacking’, where the gravitational wave strain data coincident with multiple electromagnetic events is analyzed simultaneously. We review the relevant properties of x-pipeline in Chapter 5.2, and present the modifications to x-pipeline to enable stacking in Chapter 5.3. We use the magnetar flares from O3 to study the x-pipeline input

search parameters that yield the most sensitive stacked search in Chapter 5.5. We finally demonstrate that a reduction in the significance of an unstacked x-pipeline cluster in order to achieve a specific p-value is possible with stacking in Chapter 5.6, and show a similar study pertaining to the root-sum-squared strain sensitivity in Chapter 5.7. Finally, we quantify these improvements such that we can predict the gains in sensitivity from stacks formed from N electromagnetic events, and acknowledge the limits to which stacking is useful given the input parameters to x-pipeline in Chapter 5.8. Details of the code are given in an appendix.

CHAPTER II

GENERAL RELATIVITY AND THE LIGO OBSERVATORIES

Abstract: This chapter presents a broad overview of gravitational-wave properties and detection methods, beginning with a description of gravitational waves as they arise from general relativity. We discuss small perturbations to the Minkowski metric, and show a resulting wave equation, which we provide solutions to in the far-field approximation. We then discuss the physical effect of a gravitational wave on a ring of point-particles, and how interferometry can be used to make a detection. We discuss the sensitivity of the LIGO and Virgo observatories, and the detail three of the detector characteristics and commissioning projects that I was involved in. I developed an algorithm to identify instrumental artifacts which prevented the Hanford observatory from entering observing mode, and used it to provide recommendations on how to mitigate the instrumental artifacts. I also designed a feedforward filter which helped to decouple specific sources of noise from the gravitational-wave strain channel, and I adjusted filters designed to remove noise from specific oscillatory modes from the hanging test masses.

2.1 Gravity and an Introduction to General Relativity

The first formal description of gravitational attraction was given by Isaac Newton in 1686 in which the gravitational force between two objects was proportional to their masses, and given by an inverse square law [53]:

$$F = G \frac{m_1 m_2}{r^2} \tag{2.1}$$

where m_i are the masses, r is the distance between them, and G is the gravitational constant, now accepted to have a value $G = 6.67 \times 10^{-11} \frac{\text{Nm}^2}{\text{kg}^2}$. This was an accepted theory which provided a good description of motion at slow velocities, and in the rather weak gravitational fields in which humans have lived experience on which to base our tuition.

It was not until the early 1900's that Einstein published his theory of GR (GR), which describes space and time in terms of a geometry. This theory includes perturbations to a flat spacetime which can be described as gravitational waves. Gravitational waves were first directly observed almost exactly a century after the theory was formulated: on September 14th, 2015, the LIGO Virgo Collaboration (LVC) announced its first detection of a gravitational wave, coined GW150914, caused by two inspiraling black holes [54], the properties of which were shown to be consistent with the predictions put forth by GR [55]. We dedicate the remainder of this section to examining the points of GR which are relevant to understanding the properties of gravitational waves, and specifically those predicted from isolated neutron stars [56, 57, 58].

The distance squared between any two points in a given spacetime geometry is given by:

$$ds^2 = g_{\mu\nu}(x^\alpha) dx^\mu dx^\nu \quad (2.2)$$

where g is the metric representing that spacetime, and is a function of the spacetime coordinates x^α . For flat spacetime g is merely the Minkowski metric,

given by:

$$\eta_{\mu\nu} = \begin{pmatrix} -1 & 0 & 0 & 0 \\ 0 & 1 & 0 & 0 \\ 0 & 0 & 1 & 0 \\ 0 & 0 & 0 & 1 \end{pmatrix}, \quad (2.3)$$

where $c = 1$. For a flat spacetime the distance between two points then becomes:

$$ds^2 = \eta_{\mu\nu} dx^\mu dx^\nu \quad (2.4)$$

$$= -c^2 dt^2 + dx^2 + dy^2 + dz^2. \quad (2.5)$$

A slightly curved spacetime resulting from a weak gravitational field can be represented by a perturbation to the Minkowski matrix, h :

$$g_{\alpha\beta} = \eta_{\alpha\beta} + h_{\alpha\beta}. \quad (2.6)$$

The world line of a particle in such a geometry, $x^\alpha(\tau)$ where τ is the proper time of the particle, can be found by solving the geodesic equations:

$$\frac{d^2 x^\alpha}{d\tau^2} = -\Gamma_{\mu\nu}^\alpha \frac{dx^\mu}{d\tau} \frac{dx^\nu}{d\tau} \quad (2.7)$$

where Γ is the Christoffel symbol, given by:

$$\Gamma_{\alpha\beta}^\gamma = \frac{1}{2} \eta^{\gamma\delta} \left(\frac{\partial h_{\beta\delta}}{\partial x^\alpha} + \frac{\partial h_{\alpha\delta}}{\partial x^\beta} - \frac{\partial h_{\alpha\beta}}{\partial x^\delta} \right) + O(h^2). \quad (2.8)$$

The effects of parallel transport of an arbitrary vector \bar{w} through such a curved spacetime are described by the Reimann curvature tensor:

$$(R_{\alpha\beta\gamma})^\delta w^\gamma := -(\nabla_\alpha \nabla_\beta - \nabla_\beta \nabla_\alpha) w^\delta \quad (2.9)$$

$$= -\frac{\partial}{\partial x^\alpha} \Gamma_{\beta\gamma}^\delta + \frac{\partial}{\partial x^\beta} \Gamma_{\alpha\gamma}^\delta - \Gamma_{\alpha\mu}^\delta \Gamma_{\beta\gamma}^\mu + \Gamma_{\beta\mu}^\delta \Gamma_{\alpha\gamma}^\mu. \quad (2.10)$$

Linearized Gravity

The linearized Einstein tensor is defined to be:

$$G_{\alpha\beta} = R_{\alpha\beta} - \frac{1}{2} g_{\alpha\beta} R, \quad (2.11)$$

where $R_{\alpha\beta}$ is the linearized Ricci tensor, and is a contraction of the Reimann tensor:

$$R_{\alpha\beta} = (R_{\alpha\mu\beta})^\mu \quad (2.12)$$

$$= \frac{1}{2} \left(-\frac{\partial^2 h}{\partial x^\alpha \partial x^\beta} + \frac{\partial^2 h_\beta^\mu}{\partial x^\alpha \partial x^\mu} + \frac{\partial^2 (h_\alpha)^\mu}{\partial x^\mu \partial x^\beta} - \eta^{\mu\nu} \frac{\partial^2 h_{\alpha\beta}}{dx^\mu dx^\nu} \right) + O(h^2) \quad (2.13)$$

and R is the linearized Ricci scalar:

$$R = g^{\alpha\beta} R_{\alpha\beta} \quad (2.14)$$

$$= \frac{\partial^2 h^{\mu\nu}}{\mu \partial x^\nu} - \eta^{\mu\nu} \frac{\partial^2 h}{\partial x^\mu \partial x^\nu} + O(h^2). \quad (2.15)$$

The conservation of energy requires that the Einstein tensor $G_{\alpha\beta}$, describing the gravitational field arising from matter in GR, be proportional to the stress-

energy tensor $T_{\alpha\beta}$:

$$G_{\alpha\beta} = \frac{8\pi G}{c^4} T_{\alpha\beta} \quad (2.16)$$

where the constant of proportionality is found through requiring that the analogous field equation be recovered in the Newtonian limit. We can equate Equation 2.11 and Equation 2.16 to calculate the linearized Einstein field equations:

$$-\eta^{\mu\nu} \frac{\partial^2 \bar{h}_{\alpha\beta}}{\partial x^\mu \partial x^\nu} - \eta^{\alpha\beta} \frac{\partial^2 \bar{h}^{\mu\nu}}{\partial x^\mu \partial x^\nu} + \frac{\partial^2 \bar{h}_\beta^\mu}{\partial x^\alpha \partial x^\mu} + \frac{\partial^2 \bar{h}_\alpha^\mu}{\partial x^\mu \partial x^\beta} + O(h^2) = \frac{16\pi G}{c^4} T_{\alpha\beta}, \quad (2.17)$$

where we have used a trace-reversed metric perturbation $\bar{h}_{\alpha\beta}$, defined as:

$$\bar{h}_{\alpha\beta} = h_{\alpha\beta} - \frac{1}{2} \eta_{\alpha\beta} h. \quad (2.18)$$

With the Lorenz gauge condition:

$$\frac{\partial \bar{h}^{\mu\alpha}}{\partial x^\mu} = 0, \quad (2.19)$$

equation 2.17 is recognizably a wave equation when written as:

$$-\square \bar{h}_{\alpha\beta} = \frac{16\pi G}{c^4} T_{\alpha\beta} \quad (2.20)$$

where \square is the d'Alembertian operator. $\bar{h}_{\alpha\beta}$ is then the solution to the wave equation. We can replace T with an effective stress-energy tensor $\tau^{\alpha\beta}$ which includes the $O(h^2)$ terms, and we have exact field equations:

$$-\square \bar{h}_{\alpha\beta} = \frac{16\pi G}{c^4} \tau_{\alpha\beta}, \quad (2.21)$$

which we know the solutions of given that \square is a flat-space operator:

$$\bar{h}_{\alpha\beta}(t, x) = \frac{4G}{c^4} \int \frac{\tau_{\alpha\beta}(t - ||x - x'||/c, x')}{||x - x'||} d^3x'. \quad (2.22)$$

The plane-wave solution

The sources of detectable gravitational waves are sufficiently distant that upon arrival at Earth, their spherical shell can be approximated as locally flat. We now discuss some properties of gravitational waves in the far zone approximation:

$$R \ll \lambda \ll r \quad (2.23)$$

where R is the characteristic size of the source, λ is the wavelength of the wave, and r is the distance to the source. With this, the wave can be approximated to be a plane wave. In this realm Equation 2.22 reduces to:

$$\bar{h}_{\alpha\beta}(t, x) = \frac{4G}{c^4 r} \int \tau_{\alpha\beta}(t - r/c, x') d^3x'. \quad (2.24)$$

This can be written in terms of a mass quadrupole tensor:

$$I_{ij}(t) = \int x_i x_j \tau_{00}(t - \frac{r}{c}, x') d^3x' \quad (2.25)$$

as:

$$\bar{h}_{ij}(t, x) \approx \frac{2G}{c^4 r} I_{ij}(t - \frac{r}{c}). \quad (2.26)$$

This gives an approximate value of the gravitational wave strain at great distances from the source, as a function of the properties of the source, contained in I .

Imagine a plane wave traveling in the z direction. The time and spatially dependent perturbation h can be represented as:

$$h(t, z) = \begin{pmatrix} 0 & 0 & 0 & 0 \\ 0 & h_+ & h_\times & 0 \\ 0 & h_\times & -h_+ & 0 \\ 0 & 0 & 0 & 0 \end{pmatrix} e^{i\omega(z-ct)} \quad (2.27)$$

where h_+ and h_\times are the amplitudes of the gravitational wave's plus and cross polarizations respectively, and ω is its frequency, making the total metric:

$$g_{\alpha\beta} = \eta_{\alpha\beta} + h_{\alpha\beta} \quad (2.28)$$

$$= \begin{pmatrix} 1 & 0 & 0 & 0 \\ 0 & 1 + h_+ & h_\times & 0 \\ 0 & h_\times & 1 - h_+ & 0 \\ 0 & 0 & 0 & 1 \end{pmatrix}. \quad (2.29)$$

The physical effects of this time-dependent perturbation to the metric are manifested in a time-varying change in the distance, L , between two objects oriented along both axes perpendicular to the gravitational wave, and aligned with one of the polarizations (for instance the $+$ polarization):

$$\frac{\delta L_x}{L_x} = +\frac{1}{2}h_+ \sin(\omega t) \quad (2.30)$$

$$\frac{\delta L_y}{L_y} = -\frac{1}{2}h_+ \sin(\omega t). \quad (2.31)$$

The time-varying effects of gravitational waves acting on an otherwise stationary ring of point-particles in both polarizations are shown in Figure 3.

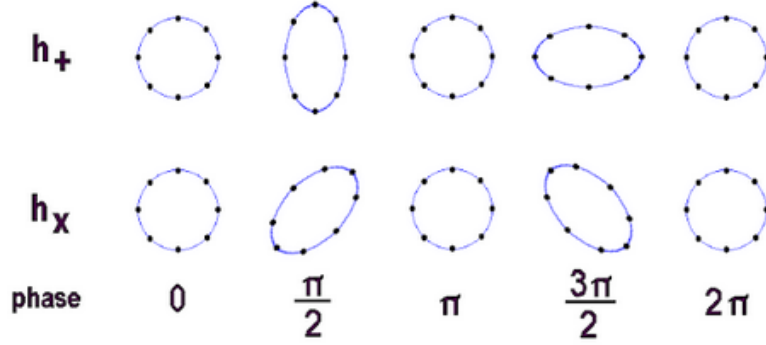


FIGURE 3. The effects of the plus and cross polarization on a ring of stationary point particles at different stages of phase evolution [4]. The top row represents the effects of the + polarization, and the bottom row represents the x polarization. In each case the arrangement of particles is elongated along one axis, returns to its circular shape, and then is elongated along the perpendicular axis before returning to its unperturbed state when the phase reaches 2π .

The gravitational-wave energy flux is given by:

$$\frac{dE}{dt dA} = -\frac{c^3}{16\pi G} \langle \dot{h}_+^2 + \dot{h}_\times^2 \rangle . \quad (2.32)$$

Integrating this to include all solid angles gives the gravitational wave luminosity.

To include the physical properties of the system, we write it as:

$$L_{GW} = -\frac{dE}{dt} = \frac{1}{5} \frac{G}{c^5} \langle I_{ij} \dot{I}^{ij} \rangle \quad (2.33)$$

where I is the mass moment:

$$I^{ij} = \int \left(x^i x^j - \frac{1}{3} r^2 \delta^{ij} \right) \tau^{00}(x') d^3 x' . \quad (2.34)$$

Although GR includes much more detailed descriptions of space and time and gravitational waves from different sources, the above is sufficient for understanding the gravitational wave science surrounding magnetar flares and FRBs.

2.2 Introduction to the LIGO Observatories

Figure 3 shows a very exaggerated response from a ring of point particles interacting with a gravitational wave moving vertically through them. Gravitational wave detectors are designed to detect this change in distance from one side of the ring to the other, but on much smaller scales. The current gravitational wave detector network is comprised of 2nd generation, ground based detectors. This includes the two Laser Interferometer Gravitational Wave (LIGO) observatories in Hanford, Washington, and Livingston, Louisiana (H1 and L1 respectively), and the Virgo observatory in Pisa, Italy (V1). These interferometers were originally patterned after the Michelson and Morley interferometer [59], which was used to search for the hypothetical ether which light traveled through.

The basic design of a laser interferometer consists of a laser which passes through an optic (called the beamsplitter), which splits the light into two beams and lets one beam pass through and re-directs the other at 90° . These beams then travel down 4 km long vacuum tunnels called arms, and then reflect off of test masses hanging at the end of the arms called the End Test Mass (ETM). The beams travel back along the arms and re-combine in the beamsplitter, before being read by a photodiode. When the laser light initially passes through the beamsplitter and becomes two beams, they are both in phase. As long as both arms are exactly the same length (or off by an integer multiple of the wavelength of the laser) then they will still be in phase upon return. But if a gravitational wave were to pass through such that the arms were aligned along the direction of polarization, then at any given point one arm would be slightly longer and one would be slightly shorter (by the amount δL from Equation 2.30).

The quantity that we measure is the difference in the arm lengths at any given time:

$$\Delta L = \delta L_x - \delta L_y \tag{2.35}$$

where L_x and L_y are the uncontracted lengths of the x and y arms respectively. If ΔL is an integer multiple of the laser's wavelength then the photodiode will detect constructive interference, and if $\Delta L = (n + .5)\lambda$, then the light interferes destructively. We can interpolate to find the value of ΔL given the interference at the photodiode.

There are several alterations to the basic design of the Michelson Interferometer which optimize the sensitivity to gravitational waves. Figure 4 shows a schematic of the Advanced LIGO optical setup [5].

Each arm is interrupted near the beamsplitter with an Input Test Mass (ITM). These are optics with a transmission coefficient of just 1.4%, causing the light to reflect back and forth approximately 300 times between the ETMs and the ITMs, effectively turning the arm into a Fabry- Pérot cavity. This allows power to build up to 750 kW in the arms, and effectively increases the arm lengths L in Equation 2.30. The advantage to this is that any contraction to the arms δL is then amplified, and so is the interference in the output arm.

A second addition to the Michelson is power recycling [60], which results in a sensitivity increase across a broad frequency band. Before entering the arms the laser power is built up in a Power Recycling Cavity (PRC), which is a resonant cavity formed between a highly reflective Power Recycling Mirror (labeled PRM in Figure 4, and the Michelson. The length of this cavity is extended to 57.6 m by two additional rounded mirrors labeled PR2 and PR3 in Figure 4 [5]. The laser light

enters the PRC at 125 W, and the PRC amplifies it to 5.2 kW by the time it passes through the beamsplitter.

A signal recycling mirror is located near the anti-symmetric port of the Michelson, indicated in Figure 4 as SRM. This forms a resonant Signal Recycling Cavity (SRC) which is 56 m in length and is comprised of two additional mirrors, labeled SR2 and SR3. Signal recycling adds the coherent signal incident on the SRM back into the interferometer, and is a process which effectively lowers the arm cavity finesse to a value of 450 [5]. This strikes a balance between the reduced coupling from the Michelson at higher finesse, and reduced sensitivity to optical loss at lower finesse. A more detailed description of both power and signal recycling can be found in [61].

The sensitivity of second-generation gravitational-wave detectors is limited at high frequencies by laser shot noise, which is due to statistical fluctuations of the arrival times of the photons at the dark port, due to light's quantum nature. A first study on the effect of injecting squeezed states of light into a LIGO observatory were done in 2011, when squeezed light was injected into GEO 600 (GEO) [62, 63, 64], and its sensitivity increased. A similar study was done on an initial LIGO detector in 2013, with sensitivities shown to increase to beyond the quantum limit [65]. Squeezed light was implemented in the Advanced LIGO detectors in preparation for O3 [66], which led to a 35% and 25% reductions in detector noise between 1.1 kHz and 1.4 kHz for LIGO Livingston Observatory (LLO) and LHO respectively. The sensitivity of the LIGO instruments are standardized by the angle-averaged radius at which a Binary Neutron Star (BNS) merger involving two canonical 1.4 solar-mass neutron stars can be detected with a Signal-to-noise ratio (SNR) of 8. We call this distance the *BNS range*, or the *range*. The BNS

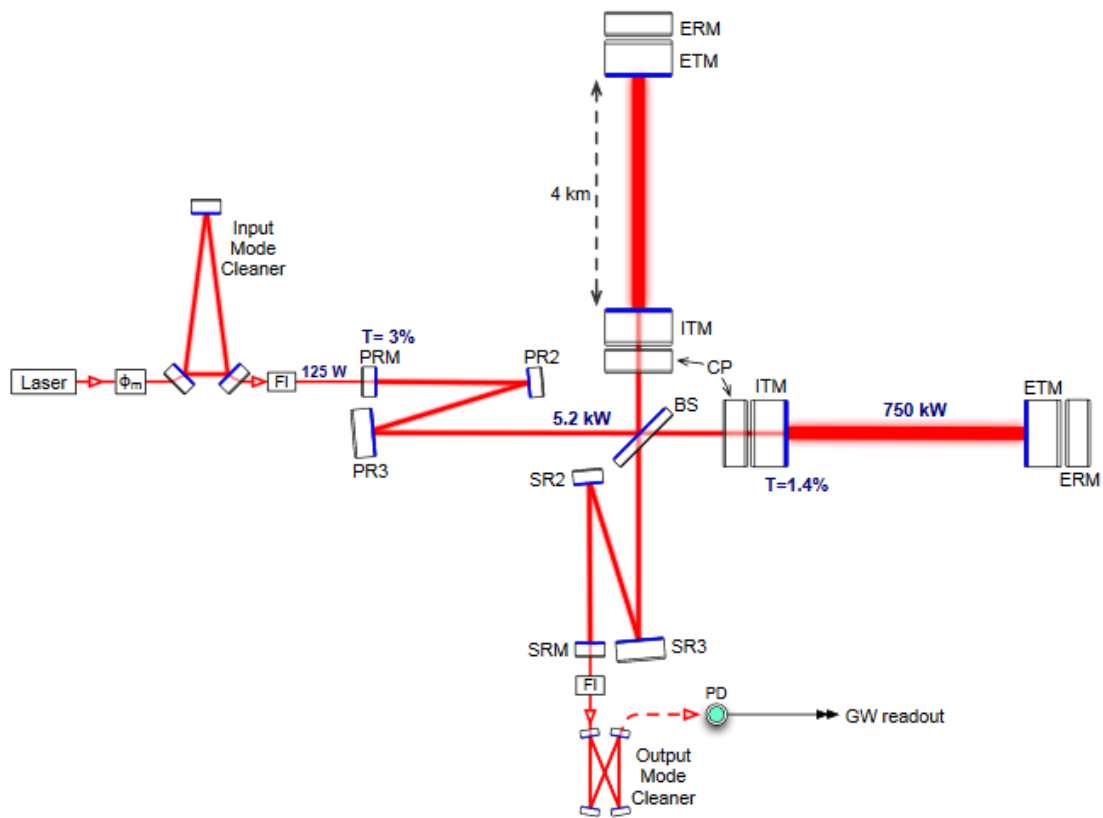


FIGURE 4. The optical setup of Advanced LIGO [5]

range increased by 12% and 14% for LHO and LHO respectively when squeezing was implemented.

2.3 Detector Response to a Gravitational Wave

We now discuss the response of the detector to a plane wave incident on the detector from an arbitrary direction. As previously stated, gravitational-wave detection happens through recognizing the laser's interference at the anti-symmetric port, after the power-recycling cavity. The phase of the light upon leaving the Fabry-Pérot cavities depends on how much time it spent contained there:

$$\Phi = \int \omega dt \tag{2.36}$$

where Φ is the phase of the light, and ω is the frequency of the laser [7]. To gain a directional sensitivity the integration needs to be done over the lengths that the laser light travels, and we make this transformation:

$$dt^2 = dx_\mu g_{\mu\nu} dx^\nu. \tag{2.37}$$

where $g_{\mu\nu} = \eta_{\mu\nu} + h_{\mu\nu}$ is the perturbed space-time metric and $h_{\mu\nu}$ is given by the Equation 2.27, in the case of a plane-wave traveling in the z direction.

To generalize to a plane wave from any sky direction (ϕ, θ) , where ϕ and θ are the azimuthal and polar angles respectively, we replace z in Equation 2.27 with:

$$z = \sin \theta \cos \phi x + \sin \theta \sin \phi y + \cos \theta z. \tag{2.38}$$

The metric also undergoes a rotation from operator R , which rotates it into the source direction:

$$R(\phi, \theta) = R(\phi)R(\theta), \quad (2.39)$$

where $R(\phi)$ and $R(\theta)$ are defined as (dropping the time component):

$$R(\phi) = \begin{pmatrix} \cos \phi & -\sin \phi & 0 \\ \sin \phi & \cos \phi & 0 \\ 0 & 0 & 1 \end{pmatrix} \quad (2.40)$$

$$R(\theta) = \begin{pmatrix} \cos \theta & 0 & \sin \theta \\ 0 & 1 & 0 \\ -\sin \theta & 0 & \cos \theta \end{pmatrix}. \quad (2.41)$$

The rotation we do is then:

$$\hat{h} = R(\phi, \theta)hR(\phi, \theta)^{-1} \quad (2.42)$$

$$\begin{aligned} &= \begin{pmatrix} \cos \phi & -\sin \phi & 0 \\ \sin \phi & \cos \phi & 0 \\ 0 & 0 & 1 \end{pmatrix} \begin{pmatrix} \cos \theta & 0 & \sin \theta \\ 0 & 1 & 0 \\ -\sin \theta & 0 & \cos \theta \end{pmatrix} \begin{pmatrix} h_+ & h_\times & 0 \\ h_\times & -h_+ & 0 \\ 0 & 0 & 0 \end{pmatrix} \\ &\times \begin{pmatrix} \cos \theta & 0 & -\sin \theta \\ 0 & 1 & 0 \\ \sin \theta & 0 & \cos \theta \end{pmatrix} \begin{pmatrix} \cos \phi & \sin \phi & 0 \\ -\sin \phi & \cos \phi & 0 \\ 0 & 0 & 1 \end{pmatrix} \quad (2.43) \end{aligned}$$

$$= \begin{pmatrix} h_{xx} & h_{xy} & h_{xz} \\ h_{yx} & h_{yy} & h_{yz} \\ h_{zx} & h_{zy} & h_{zz} \end{pmatrix}. \quad (2.44)$$

The quantity

$$|h_{xx} - h_{yy}| \tag{2.45}$$

is the difference in the detector response to the GW strain in the X and Y directions. The practical interpretation of the components of the detector response function, h_{xx} and h_{yy} , is an integration of Equation 2.36 along the X and X arm respectively, and these are given by [7, 67]:

$$h_{xx} = -\cos\theta \sin(2\phi)h_{\times} + (\cos^2\theta \cos^2\phi - \sin^2\phi)h_{+} \tag{2.46}$$

$$h_{yy} = \cos\theta \sin(2\phi)h_{\times} + (\cos^2\theta \sin^2\phi - \cos^2\phi)h_{+} \tag{2.47}$$

.

Doing the subtraction in Equation 2.45 gives the antenna function for the detectors:

$$|h_{xx} - h_{yy}| = -2\cos\theta \sin(2\phi)h_{\times} + (-\sin^2\phi + \cos^2\phi)h_{+} \tag{2.48}$$

$$= F_{\times}^2 h_{\times} + F_{+}^2 h_{+} \tag{2.49}$$

$$= F^2. \tag{2.50}$$

Figure 5 shows the detector response to a gravitational wave [6, 7]. Both LHO and LLO are positioned such that one arm from each detector is co-aligned as much as is possible, given the curvature of Earth. We define the polarization in which they lie such that the sensitivity to +-polarized gravitational waves is maximized in the sky-directions above the arms of the detectors. The reason for orienting both detectors along the same axis was to increase the sensitivity to a

specific polarization for the purposes of making the initial detection, which would have been a more dubious goal without the gain in sensitivity that this provided.

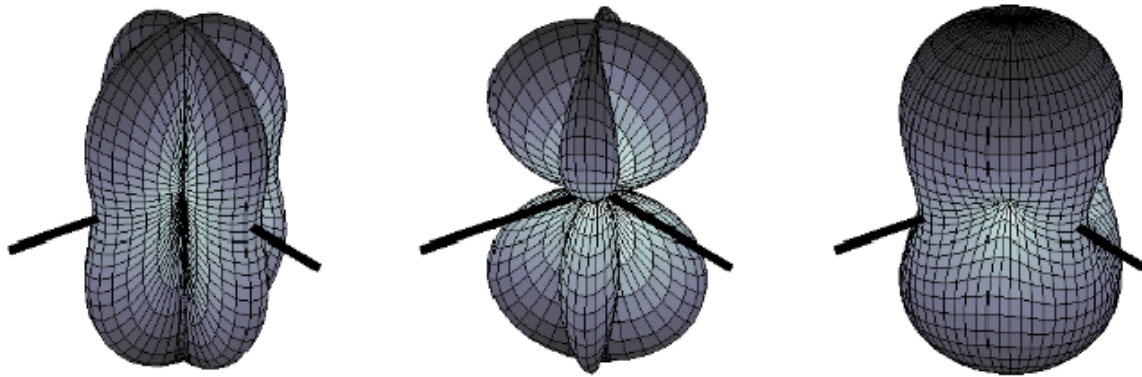


FIGURE 5. Antenna response pattern for a gravitational wave detector for the $+$ polarization (left), the X polarization (center) and mean polarization (right) [6, 7]. The arms of the gravitational-wave detector are taken to lie along the black lines, and the radius from a point on the surface to the origin represents the sensitivity to gravitational waves of that polarization in that direction.

I spent the summer quarters of 2018 and 2019, as well as winter of 2019 as an LSC fellow at the LIGO Hanford Observatory. My first two quarters there were spent preparing for the O3 observing run, and helping with Detector Characterization, Physical Environmental Monitoring (PEM), and commissioning projects. I helped test and upgrade the PEM sensors (such as accelerometers and magnetometers) and injection tools and wrote code to make mechanical hardware injections and analyze the responses. I also wrote code that calculates the coherence between any auxiliary channel and the gravitational-wave strain channel, which was then incorporated into the F-scan code, and makes daily updates to the Detector Summary pages. I helped the commissioning team to identify a specific type of glitch in the Arm Length Stabilization lasers, and studied possible sources of them. I also designed feedforward filters for the Length Sensing and Control degrees of freedom, which resulted in the BNS inspiral range increasing by

approximately 2 Mpc. I also studied the oscillation modes of the fibers supporting the test masses, and designed monitoring and damping filters to mitigate their effect on the gravitational-wave strain data. The rest of this chapter is devoted to detailing some of these projects.

2.4 ALS glitches

Here we detail a commissioning project in which I wrote code to identify a specific type of instrumental artifact in the data called a glitch, and searched for an environmental cause in an effort to mitigate it. We discuss the process by which the detector is brought into observing mode, and the channels where these glitches were found, and hypotheses as to their origin. We then describe an algorithm which can identify them, and the efforts which were made to reduce their prevalence in the lead-up to the third observing run.

Bringing the interferometer to a state of low-noise sensitivity in which we take data suitable to be used for scientific study requires that the length of each cavity be manipulated such that they are all resonant. There are seven optics that are relevant in that they can be manipulated to change the length of a cavity. These are the End Test Masses (ETMX and ETMY), the Input Test Masses (ITMX and ITMY), the beamsplitter (BS), the Power Recycling Mirror (PRM) and the Signal Recycling Mirror (SRM), most of which are shown in either Figure 4 or Figure 6. It is more physically relevant to translate these into seven other degrees of freedom. The first of these are the Common Arm length (CARM) and the Differential Arm length (DARM), which is the channel used for measuring gravitational-wave strain. The Power Recycling Cavity Length (PRCL) and Signal Recycling Cavity Length (SRCL) are the average distances from the PRM or SRM respectively to the ITMs.

The Michelson length (MICH) is the distance from the BS to the ITMs. The other 2 degrees of freedom have no relevance to the physics. These are the breathing mode (a scaled expansion of all of the optics), and a translation.

Bringing all of the cavities into resonance is a successive process referred to as ‘locking the interferometer’ [5], for which we use the Pound-Drever-Hall (PDH) technique. For a cavity to be locked to a laser with a given wavelength means that the total path traveled by the light is an integer multiple of that wavelength of light.

There is a specific sequence to follow in the locking, beginning with locking the Input Mode Cleaner (IMC). Then the Michelson is locked, and then the length of the Fabry-Pérot cavities on both the X and Y arm are individually locked and manipulated such that they lock to the Michelson. We use the ALS system to accomplish this, a schematic of which is displayed in Figure 6. The ALS lasers are mounted behind both of the end test masses, on which they actuate. Two feedback loops are engaged which actuate on the respective end test masses to slowly reduce the common mode frequency offset between the 532 nm ALS laser and the main laser. The ALS lasers have wavelength 532 nm, and are locked to their respective arm cavity, meaning that the arm cavity length is an integer multiple of half of this wavelength. We then transition all control of the optics from the ALS lasers to the main laser, whose light has twice the wavelength at 1024 nm. We use CARM to make this transition; the actual value of CARM is irrelevant, but we do need it to be consistent. When we’ve transferred control to the main laser we proceed with the rest of the locking sequence, including locking PRCL, SRCL, and MICH.

In the lead-up to O3 the commissioners began to experience delays and even losses of lock during the ALS locking stage, which was preventing us from

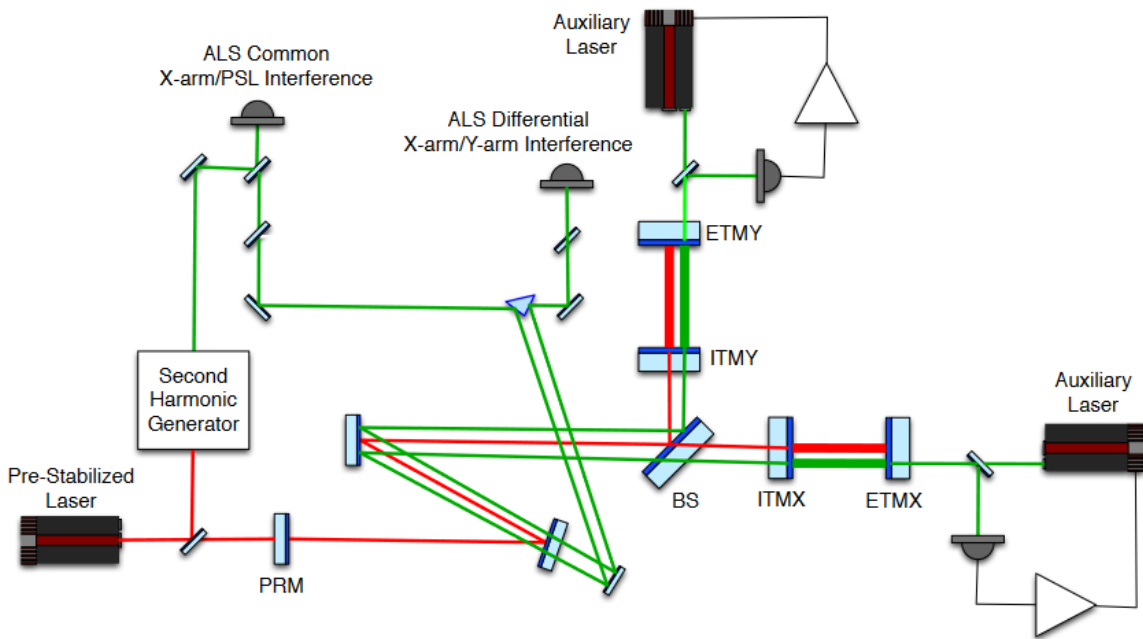


FIGURE 6. The optical setup of the Arm Length Stabilization system.

getting to low noise sensitivity. They anecdotally noticed a correlation between locking delays and the outside weather, specifically the presence of light rain. The commissioners examined both the X and Y transmission channels (given by H1:ALS-C_TRX_A_LF_OUT_DQ and H1:ALS-C_TRX_A_LF_OUT_DQ respectively), which measure how much of the green ALS laser light transitions through the ITMs. Since the ITMs are semi-transmissive and the amount of light that is permitted to escape is proportional to the amount of light resonating in the Fabry-Pérot cavities, any fluctuations in the signal in these channels is indicative of variable laser energy in the corresponding cavity.

The commissioners noticed several instances of sudden high-frequency drops in the transmission signal, and the trend data representing these is displayed in Figure 7. It is important to note that this figure displays severely down-sampled data, and so does not adequately display the high frequency of these signal drops. A zoomed-in time series of one of these high-frequency drops is shown in Figure 8.

The commissioning team termed these signal drops ‘rainy day glitches’, or ‘ALS glitches’.

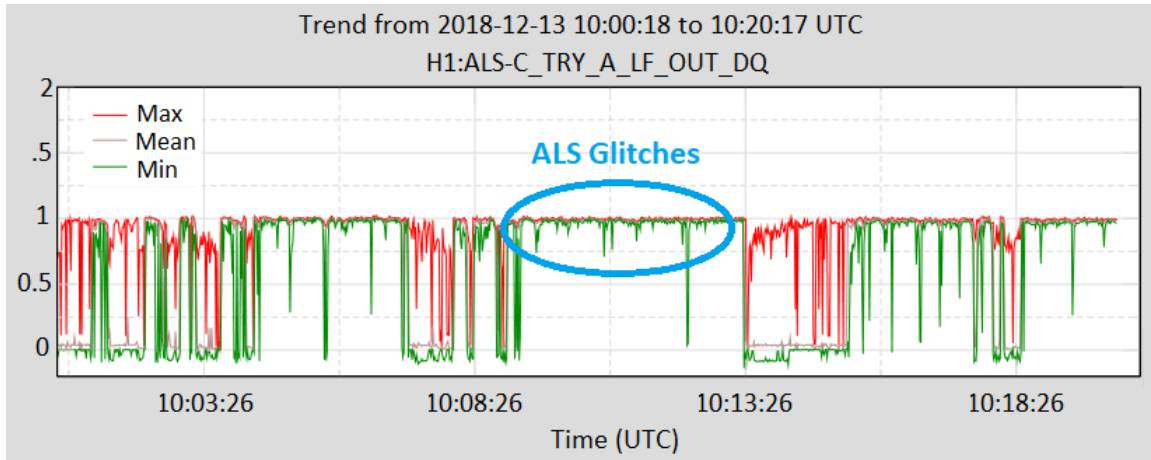


FIGURE 7. The second trend data from the Y-arm transmission channel taken on December 13th, 2018 [8]. The green shows the minimum values per second. The first events that were having a noticeable effect on locking the interferometer are most visible as small dips in the minimum trend between about 10:10 and 10:13 UTC. These were the ones that were first coined as ‘rainy day glitches’ by the commissioners.

The process of matching the frequency and phase offset of the main laser with the ALS lasers requires the main laser light to be sampled at the end stations where the ALS lasers are. So a small amount of light from the pre-stabilized laser is transported via an underground fiber down each of the arms, outside of the enclosure. Any mechanical disturbances to this fiber could result in a disruption of the information brought by the fiber, and then the ALS laser could respond with a momentary change in frequency and a drop in power in the cavity, delaying the lock. These ALS glitches were problematic because they were effectively decreasing the amount of time that the Hanford observatory could spend in observing mode.

A section of the ALS fiber on the X arm had become exposed as a result of many years of wind, rain, and random movement of earth since its burial, and

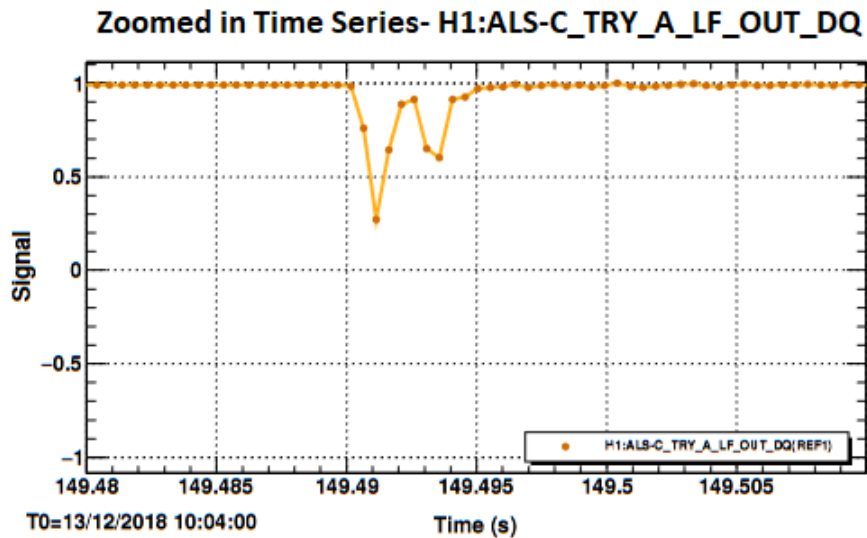


FIGURE 8. A zoom in of the trend data from the Y-arm transmission channel taken on December 13th, 2018 [8]. The drop in the signal indicates a high-frequency ALS glitch.

the hypothesis was that rain droplets were hitting the exposed fiber and causing disturbances. Potential solutions included buying a new ALS fiber and running it inside the enclosure, and somehow re-enforcing the fiber already in place. We eventually adopted a short-term solution of just re-burying the exposed portion of the fiber. My goal was to develop an algorithm that would correctly identify these ALS glitches, and calculate a rate at which they happen. Then I could use those glitch rates to search for environmental correlations, and specifically check for any correlation with rain.

First attempts at such an algorithm correctly identified the ALS glitches, but also identified events which were instead high-frequency variation of a non-stationary signal, rather than the sharp, discrete drops that were thought to be problematic for locking, displayed in the top plot of Figure 11. This high-frequency variation of the transmission signal was caused by the noise-eater on one of the

ALS laser crystals, which helps to reduce the laser intensity noise, and is not important for our purposes.

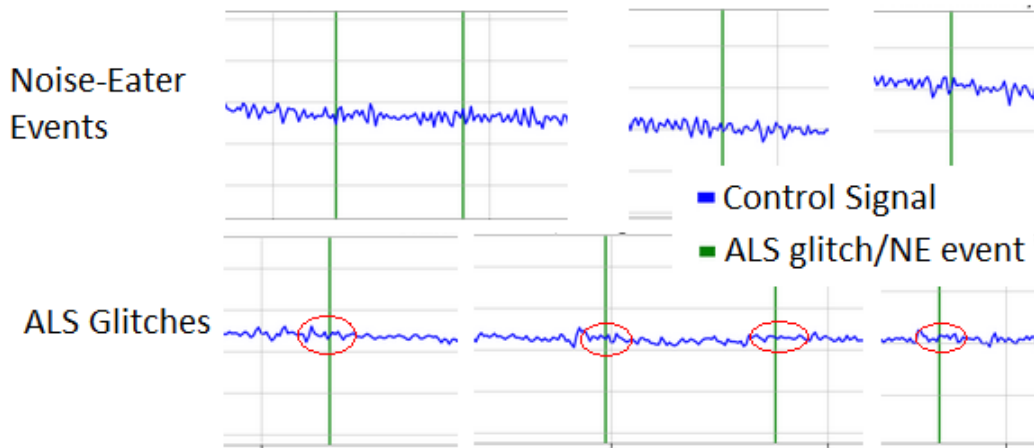


FIGURE 9. The control signal at both the times of the noise-eater events (top) and the times of the ALS glitches (bottom). We see that when the algorithm identifies a noise-eater event, there is a lot more noise in the signal than when it identifies an ALS glitch. On the bottom, we see that just before the time of each ALS glitch, the control signal jumps up to a higher value, and remains there and then comes back down just after the glitch, forming what we call a ‘plateau’ in the signal. The locations of these plateaus are emphasized with red circles.

Furthermore, the ALS glitches can be distinguished from the noise-eater events because they are accompanied by a discontinuous rise and plateau in their respective control channels, H1:ALS-X_REFL_CTRL_OUT_DQ or H1:ALS-Y_REFL_CTRL_OUT_DQ, which we show in Figure 9. We then write another algorithm that searches for the plateaus in the control signal, and define an ALS glitch as being specifically where a transmission glitch and a control plateau happen together. We define a transmission glitch as a data point in the transmission signal which:

- Has a value of at most .04 less than the mean of the transmission signal in that 10s segment of data

- Has a minimum value of .02 when high-passed at 400 Hz.
- Is in a section of signal where the local average is at least .85

We search for control signal plateaus by fitting a line to the raw signal both immediately before a distinct rise and immediately after. A histogram of the standard error of the slope on these lines of best fit is shown in Figure 10. The four distributions in this histogram (the standard errors of the lines of best fit before and after both noise-eater events and real ALS glitches) show distinctly different properties of the signal at the times of a true ALS glitch, and a noise-eater event. These distributions are used to set threshold values and distinguish between ALS glitches and noise-eater events.

We define the control signal plateaus as times when:

- The control signal high-passed at 1200 Hz exceeds 0.002
- The separation between the lines of best fit after and before the discontinuity are greater than 5.6×10^{-4} .
- The error in the line of best fit before this discontinuity is less than .23 or the error in the line of best fit after is less than 0.25.

An ALS glitch is then identified when a transmission glitch has a plateau either immediately before it or immediately after. An example of signals with ALS glitches is shown in Figure 11. This algorithm correctly identified all of the problematic drops in the transmission signal given in [8], and did not include any of the noise eater events. We used this algorithm to search for any correlation with physical environmental monitoring channels, specifically accelerometers,

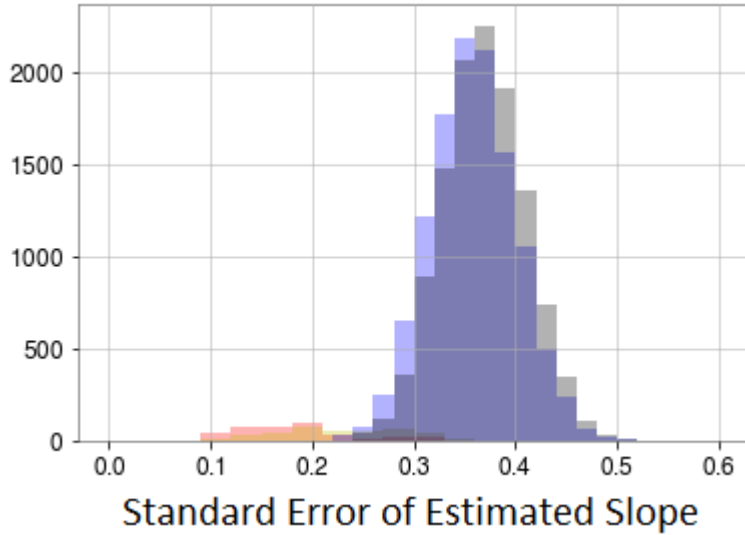


FIGURE 10. The standard error on the lines of best fit to the control signal. We fit lines to the signal both before and after a distinct rise in the signal. Here we have four histograms of the standard error of these lines: the blue and grey histograms are from data before and after noise-eater events respectively, and the red and yellow distributions are from before and after true ALS glitches respectively. We can see distinct population differences in the standard errors for ALS glitches and for noise-eater events, and we choose our threshold values such that we can optimize the accuracy of our glitch identification algorithm.

microphones, relative humidity monitors, and seismometers, and found no significant correlations.

We then consider how the glitch rates change over time. Figure 12 shows the a timeline of the rate of ALS glitches during the commissioning phase before O3, and during the beginning of O3. These glitch rates are computed in 10 s averages, and only includes times during the ALS locking sequence.

We see no obvious reduction in the rates of glitches after the fiber was covered. It does seem as though there are fewer glitches during the actual observing run, and this is likely because we spend more time observing, and because we take additional precautions in mitigating environmental noise.



FIGURE 11. ALS glitches identified over a 10 s span of time by the algorithm involving both the control and transmission signals. This was a span of time containing events that the commissioners identified as true ALS glitches that were detrimental for the locking process. The red signal is the transmission signal, the blue signal is the control signal, and the horizontal black line on the bottom plot represents the threshold value of the high-passed transmission signal at which a transmission glitch is identified. The times of the ALS glitches here are indicated by vertical green lines.

The analogous glitch rate timeline for this algorithm applied to O2 is plotted in Figure 13. The algorithm clearly identifies these glitches as beginning immediately after the commissioning break. A laser safety tag was discovered shortly after the commissioning break in the Mass Storage Room (MSR) [9] which was free to flap and make contact with the ALS fiber. The commissioners taped this tag down to prevent the flapping. We mark the time at which this tag was secured, and see that this seems to have fixed the ALS glitch problem in O2.

Since the source in O2 was an obvious mechanical disturbance to the ALS fiber, it is reasonable to guess that the cause in O3 might be another mechanical disturbance. But since covering the ALS fiber in O3 did not lead to a significant

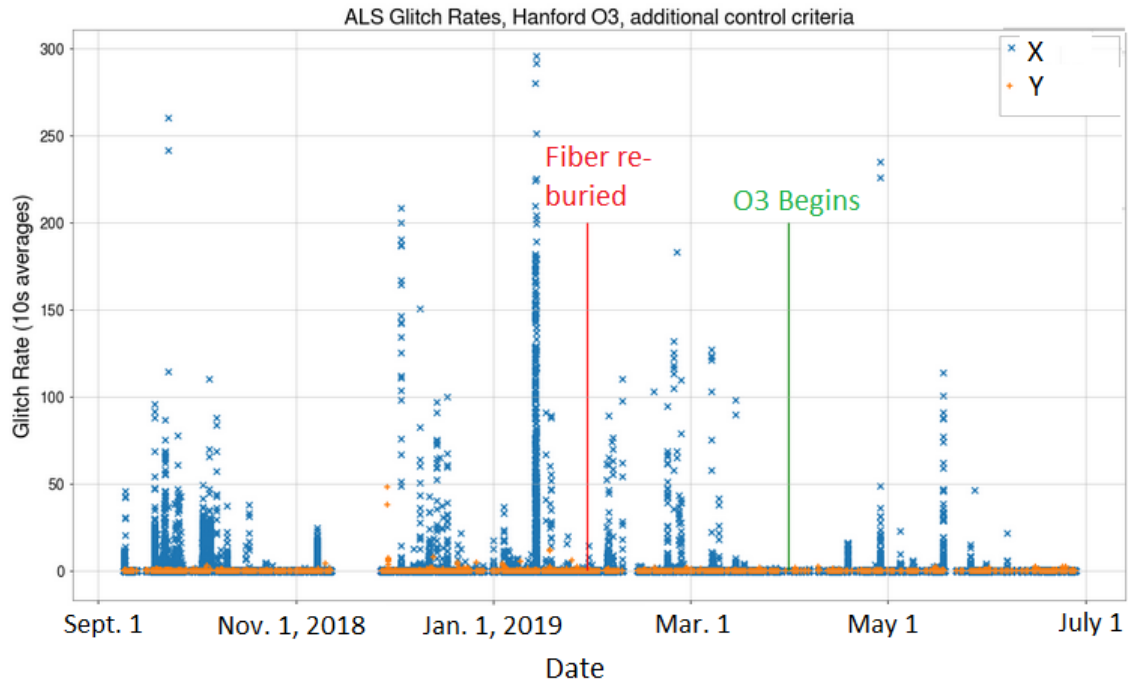


FIGURE 12. A timeline of the ALS glitch rates (10 s averages) between September 2018 and July 2019, calculated using the algorithm involving both transmission and control signals. As with the previous algorithm, there is no obvious improvement after the fiber was re-buried, and the improvement after the beginning of O3 is likely due to longer lock stretches and therefore less time spent locking.

reduction of ALS glitches, a decision was made not to replace the ALS fiber for the remainder of the observing run, a decision which saved the collaboration approximately 100,000 dollars.

Glitches, or unexplained bursts of energy uncorrelated between detectors or any astrophysical source, are an issue in many of the channels (including DARM) in both of the LIGO detectors. Determining their mechanical and environmental causes might help mitigate them, but more realistically determining a probability that an event is indeed an instrumental artifact is essential for determining the accuracy and sensitivity of our searches. While this particular glitch-finding algorithm was effective for distinguishing true ALS glitches from benign noise-

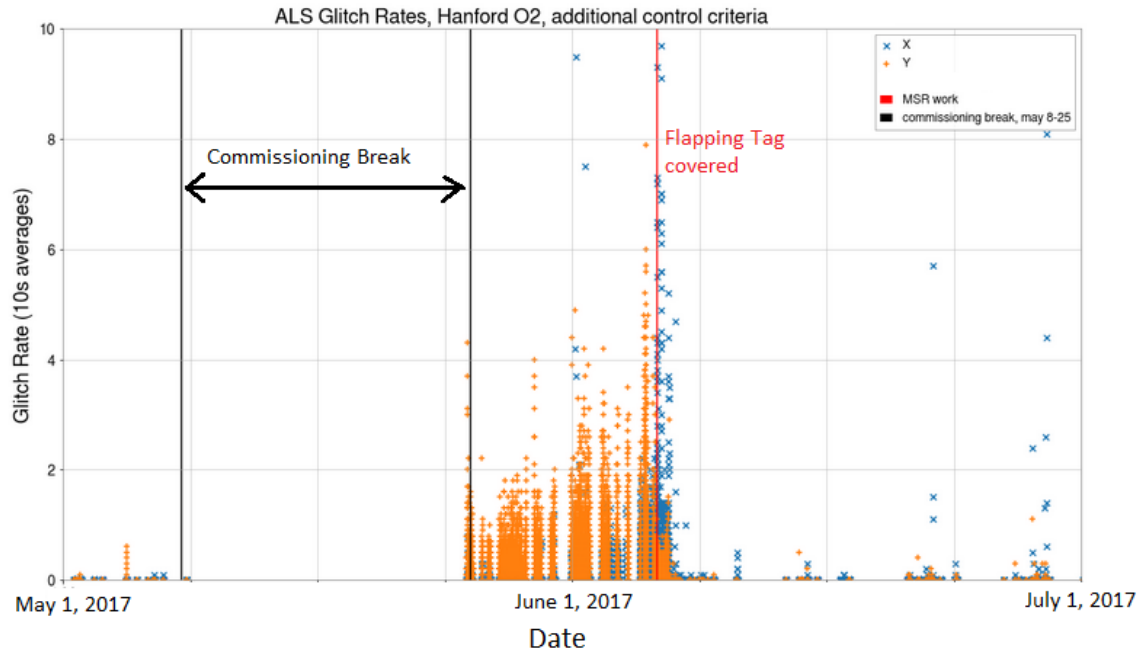


FIGURE 13. We make the analogous ALS glitch timeline to that shown in Figure 12, for O2, using the algorithm involving transmission and control signals. This algorithm identifies a very clear start to these events after the commissioning break (from May 8th to May 25th, 2017), and a point in time when the ALS glitches were solved by taping down a flapping tag in the MSR [9]. This suggests that ALS glitches can be caused by mechanical disturbances to the fiber, and also lends credence to the algorithm that we use on O3 data.

earlier events with a similar morphology, it is not probable that it will be useful in detecting glitches in other channels unless those other glitches are quite similar to the ones in the ALS system. It is, however, possible that this multi-channel approach, and recognizing glitches as containing plateau-like features might inspire other multi-step glitch algorithms.

2.5 Feedforward Filters

Another of the commissioning projects I worked on involved making feedforward filters to actuate on the ETMs and remove noise from the

gravitational-wave strain data. Here we detail the degrees of freedom where the noise can originate, and discuss the control loops and how an optimal feedforward filter is calculated. We present the filter that was used on one of the degrees of freedom, and discuss the benefits of using it in terms of detector sensitivity.

The positions of the optics and the lengths of cavities on the LIGO instruments can be described in terms of seven degrees of freedom. Three of these are Length Sensing and Control (which we will abbreviate locally in this chapter as LSC) degrees of freedom [68]: PRCL, Signal Recycling Cavity Length (SRCL), and the length of the Michelson (MICH). Measurements are made in the basis of two other degrees of freedom, CARM and DARM (the gravitational-wave strain channel). Each of the LSC degrees of freedom can and does couple into DARM, and adds noise into the spectrum which decreases the detector sensitivity in the frequency range of tens to hundreds of Hz, which is the Binary Black Hole (BBH) and BNS detection band. In this section we discuss the feedforward (FF) filters which we create to mitigate this noise.

FF filters cancel the noise in a system using a process in which the noise is sampled at one point in a system and then processed, and then actuation happens at a later point in that system to cancel the effects of that noise [69]. Each of the LSC degrees of freedom has its own automated control loop and could support a FF filter, if its contribution to the DARM noise budget were sufficiently problematic.

A schematic diagram of the control loop for MICH is displayed in Figure 14, although this same schematic is valid for each LSC degree of freedom. This control diagram is used by [10] to calculate the optimal FF filter (labeled α in Figure 14) for each degree of freedom that would minimize the actuator and sensor noise,

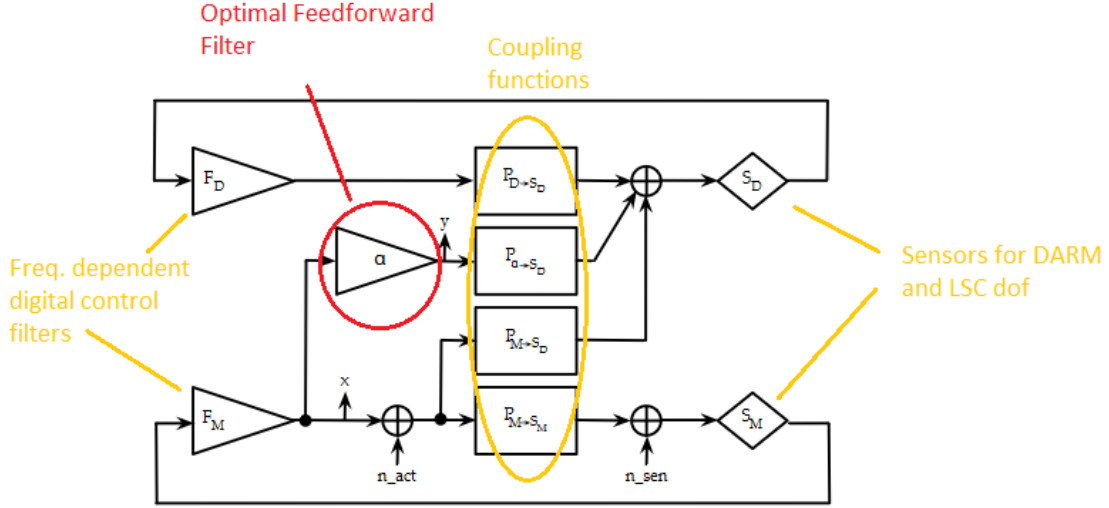


FIGURE 14. Schematic of the control loops for each Length Sensing and Control degree of freedom [10]. The triangles on the left each represent a digital control filter, one for DARM and one for MICH, given by subscripts D and M in their respective labels. The triangle labeled α is the feedforward filter. The diamonds on the right are frequency independent sensors. $P_{(D \rightarrow S_D)}$ and $P_{(M \rightarrow S_M)}$ represent any frequency dependent actuation, optics, and electronics. $P_{(M \rightarrow S_D)}$ and $P_{(\alpha \rightarrow S_D)}$ are both coupling functions from the MICH actuation to the DARM, and from the feedforward filter to DARM respectively. n_{act} and n_{sen} are the noise from MICH actuation and sensing.

n_{act} and n_{sen} respectively, detectable by the DARM sensor S_D in the diagram. We review this derivation of α in terms of transfer functions that we can calculate by making injections. In the absence of actuator noise (it is dominated by sensing noise), and without a FF filter (letting $\alpha = 0$), we can write the noise at point x in the diagram as:

$$x = n_{sen} F_M \left(\frac{1}{1 - P_{(M \rightarrow S_M)}} \right). \quad (2.51)$$

The noise at the DARM sensor, S_D , accounting for the DARM loop and both coupling and FF from MICH, is calculated to be:

$$S_D = \left(\frac{1}{1 - P_{(D \rightarrow S_D)}} \right) (P_{(M \rightarrow S_D)} + \alpha P_{(\alpha \rightarrow S_D)}) x \quad (2.52)$$

and after substituting the noise at x :

$$S_D = \left(\frac{1}{1 - P_{(D \rightarrow S_D)}} \right) (P_{(M \rightarrow S_D)} + \alpha P_{(\alpha \rightarrow S_D)}) n_{sen} F_M \left(\frac{1}{1 - P_{(M \rightarrow S_M)} F_M} \right). \quad (2.53)$$

S_D is directly proportional to n_{sen} , and we see that this effect is zero when:

$$\alpha = - \frac{P_{(M \rightarrow S_D)}}{P_{(\alpha \rightarrow S_D)}}, \quad (2.54)$$

so this is the α that provides the optimal feedforward filter [10]. This translates in practice to:

$$\alpha = - \frac{\left(\frac{S_D}{x} \right)}{\left(\frac{S_D}{y} \right)}. \quad (2.55)$$

The optimal transfer function to fit is the length to DARM transfer function divided by the FF filter to DARM transfer function.

We make injections to determine the transfer functions from the degree of freedom input to DARM, and from the FF filter output to DARM. This transfer function is a zero-pole-gain (ZPK) filter, which has a corresponding function in both time-frequency and phase space, and the ideal FF filter matches it in both respects.

We fit the ideal ZPK filter using the `data2filter` function from the package `IIRrational.v2` [70]. The highest priority frequencies to fit were the ones with high coherence between the LSC degree of freedom and DARM, which tended to be

between about 10Hz and 100Hz. The only requirements for the filter were that it cover this band, and then fall off to zero quickly outside of the band, so that it wouldn't make injections into DARM.

We employed several strategies to actually find a ZPK filter that best recreated this optimal transfer function. We defined the SNR of each data point on the ideal transfer function to be a scalar multiple of the coherence of the degree of freedom to DARM, and tried setting the SNR to 0 for all points except a few on which we wanted to focus. At one point we added manufactured data points to the optimal transfer function to give increased weight to certain desired features of the filters.

The biggest improvement to the sensitivity happened with the implementation of the PRCL filter in O3a, which is displayed in Figure 15. We implement the PRCL filter and see an increase in the BNS inspiral range of just over 2 Mpc, as shown in Figure 16.

To verify that this range increase is indeed due to the PRCL filter, we examine the coherence between PRCL and DARM both before and after its implementation, and we see a noticeable reduction in coherence in the frequency band which before had the highest coherence.

We also look at the noise budget consumed by the LSC degrees of freedom, given in Figure 18. The dark red line is the noise budget for PRCL, and we see that the noise is particularly low in the frequency range where the filter actuates after the PRCL filter was added.

Although the noise added into DARM due to the LSC degrees of freedom is now low, the PRCL filter is not optimal. We see in Figure 15 that although in general the transfer function of our ZPK filter aligns with the optimal filter we've

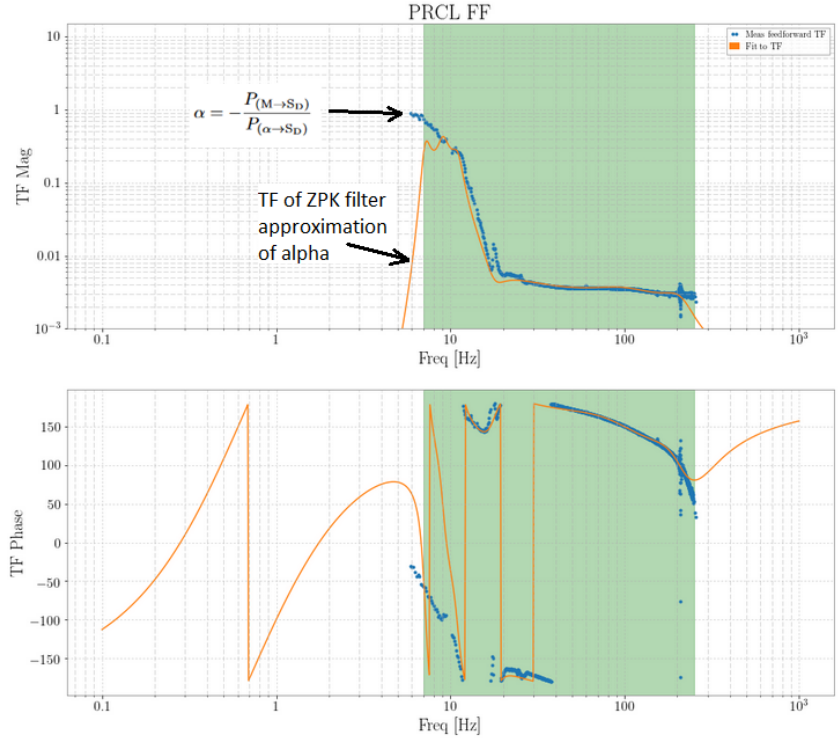


FIGURE 15. The optimal PRCL ZPK filter used in O3, [11]. The magnitude and phase of the measured transfer function from PRCL to DARM is displayed on the top and bottom plots respectively in blue. The orange lines are the magnitude and phase of the optimal filter. The shaded region shows the frequency range that is important to actuate in. Outside of this range the magnitude of the filter should drop so as not to inject into DARM. Our filter is a good fit to the optimal transfer function in most of the frequency band of highest importance, but we see that the phase of our ZPK filter is very misaligned with the optimal phase at around 10 Hz.

calculated through injections, α , in the region of 10 Hz there is misalignment in the phase. This is actually causing an increase in the coherence between PRCL and DARM in that small frequency band, as evidenced in Figure 17. We calculate the multiplicative residuals between our ZPK filter, and the optimal filter α , and plot both the phase and the amplitude of these residuals in Figure 19.

We can create iterative filters, β , applied as shown in Figure 2 of [10]. For this we rename the signal at x to z to indicate a new injection and new transfer

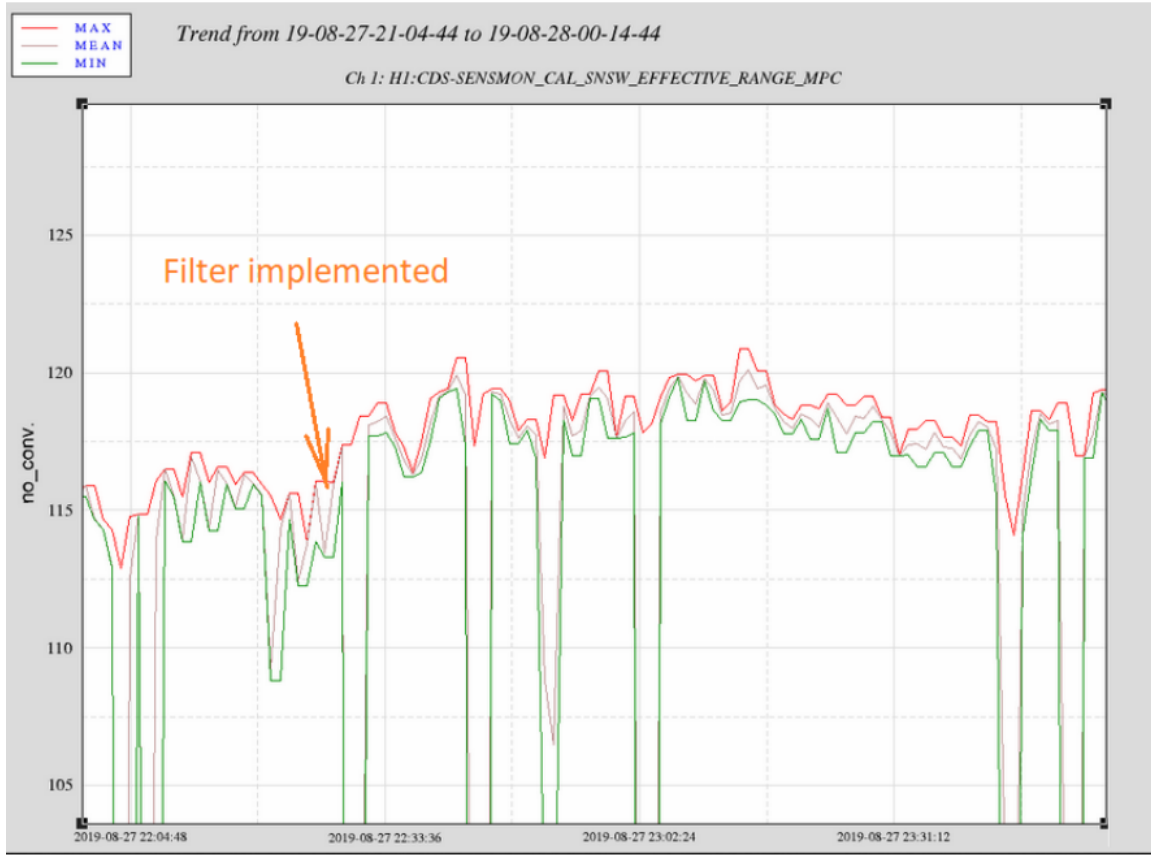


FIGURE 16. The minute trend of LIGO’s sensitivity, as measured by the BNS inspiral range in Mpc. The time at which the PRCL filter is implemented as shown, and we see an increase in range of just over 2 Mpc [11].

functions to fit, and then the new iterative filter is given by Equation 25 of [10]:

$$\beta = 1 - \frac{\left(\frac{S_D}{z}\right)}{\alpha \left(\frac{S_D}{y}\right)}. \quad (2.56)$$

One of the difficulties that we faced in creating these filters was adequately exploring the full range of parameter space that the filters could occupy in order to choose the optimal one, without spending too much human labor to do so. These parameters consisted of the number of zeros and poles, their values, and the gain.

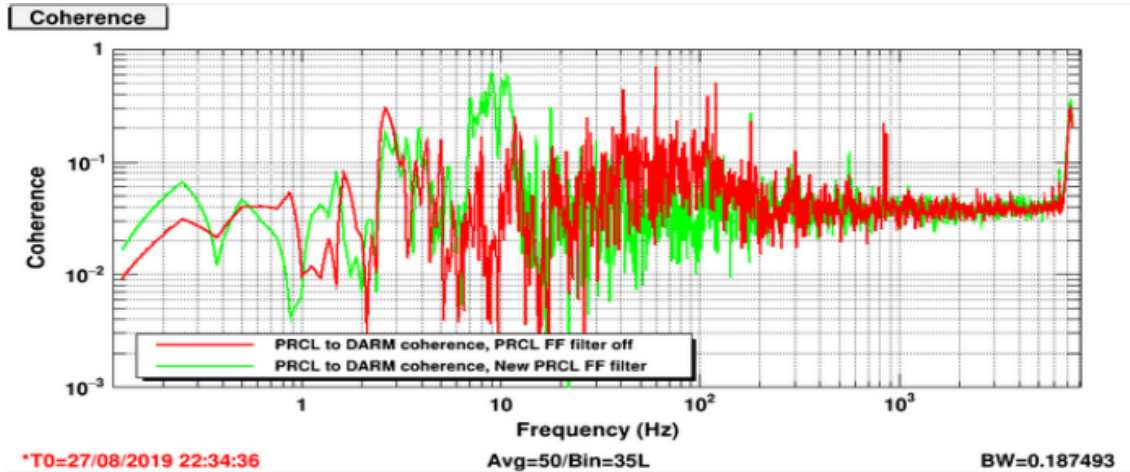


FIGURE 17. The coherence between the PRCL and DARM at each frequency before (red) and after (green) the filter [11]. We see a reduction in coherence in the frequency band at which the filter actuates.

We were able to generate distinct filters by having the code fit specific alterations of the data:

- A weighting factor that raises the SNR of specific data points and makes them a higher priority for the algorithm to fit the filter to.
- Low and high-frequency cutoffs, beyond which we disregard the data and make no effort to fit the data.
- Low and high frequency ranges which the weighting factor is applied to.
- A factor by which the data is down-sampled.

To adequately search a broad range of possible ZPK filters, we wrote code that could run remotely and in parallel. When passed a guess at the number of zeros and the gain to include, it would load the transfer function of the optimal filter and apply the alterations described above, also passed in as arguments. We also wrote some code that takes a user's guess at the optimal parameters to use,

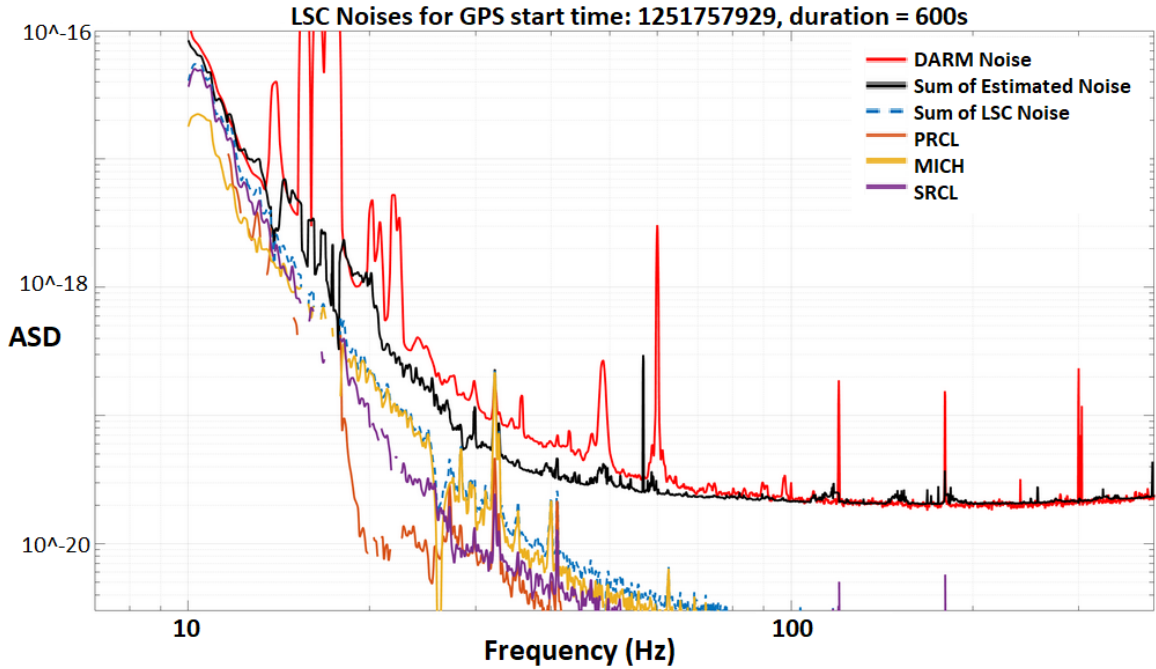


FIGURE 18. The noise budget for each LSC degree of freedom after the PRCL filter was implemented, with squeezing [12].

and then randomizes that guess so that the fitting script can search parameters in the vicinity. It is possible to use this randomization process to search parameter space adequately by simultaneously running an essentially unlimited number of remote jobs, each with a different guess in parameter space. We have also written a script to load up the resulting ZPK filters after the randomized guesses and plot the transfer functions against that of the optimal filter so that a human can scroll through and choose the one that best fits our needs.

The most effective filter that we used is shown in Figure 15, and gained us just over 2 Mpc of BNS range, as shown in Figure 16. The sky-volume that we have sensitivity to increases as the range³, so this increased by approximately 5.3%. While it is true that our attempts to make an iterative filter based on the residuals of the first filter and on Equation 2.56 did not successfully produce a

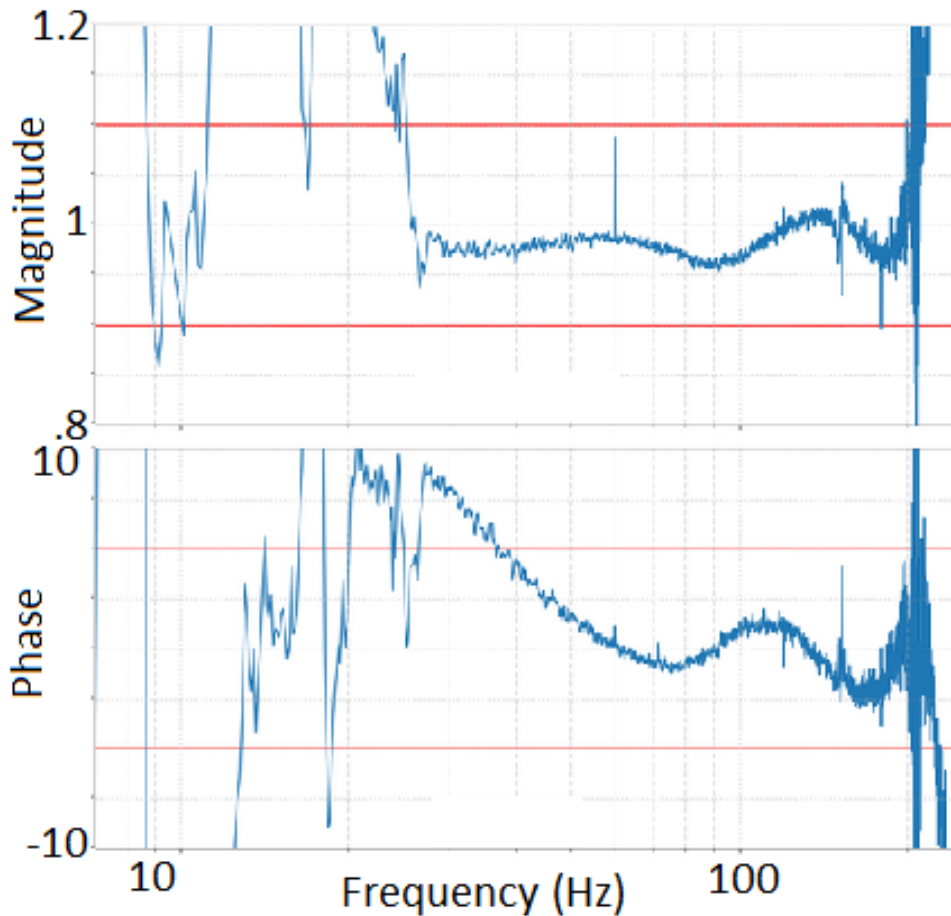


FIGURE 19. The multiplicative residuals between α and the best fit to α . [11]. A perfect filter would yield a multiplicative residual amplitude of 1 and phase of 0 at every frequency. The red lines represent an arbitrary margin of error on the residuals to still have an acceptable filter. Any iterative filters should prioritize the frequencies which fall outside of this range.

filter which was an obvious improvement on the first one, the automated attempt using randomized guesses in parameter space is a concept that will hopefully be of assistance in future filters created for O4.

2.6 Violin Mode Damping Filters

We now discuss a commissioning project in which I attempted to adjust filters to damp out the oscillatory modes of the fibers suspending the tests masses. These

are the most prominent spikes in the DARM spectrum of the multiples of 500 Hz, the fundamental frequency. Here we discuss the properties of the test masses that lead to these oscillation modes, and the efforts to associate each mode with a test mass. We use damping filters to mitigate their effects on DARM, and show the resulting reduction of the DARM spectral lines.

All four test masses, the two ITMs and ETMs are 40 kg fused silica optics which are 20 cm thick, and 34 cm in diameter [68, 71]. Each test mass is suspended by four stages of suspended masses connected by steel wires and silica fibers for passive seismic isolation, and with active isolation in the first two stages. A reaction mass interacts with the test mass through an electrostatic drive such that they are not in thermal contact. Fused silica is used to attach to the actual test mass, which reduces the suspension thermal noise. A diagram of the test masses used in Advanced LIGO is included in Figure 20.

Fused silica is a very brittle substance, and as such it can support high-Q modes of oscillation. There are 4 fused silica strands connected to each test mass, and each of them is free to oscillate in either direction orthogonal to Earth's gravity. This makes eight fundamental oscillation modes that we call 'violin modes', and each of these provides a very high-Q noise source in DARM at a very exact and fixed frequency at approximately 500 Hz. The violin modes and all of their harmonics are by far the loudest sources of noise in the DARM spectrum. Finding a filter which can effectively damp each mode, and adding it into the violin mode guardian, a bank of automated damping filters, can reduce the DARM noise floor in the frequency bands near the violin modes and their beat frequencies.

The loudest violin modes in O3 were actually the second harmonic, and so these are the ones that we focused most of our efforts on damping. They are visible

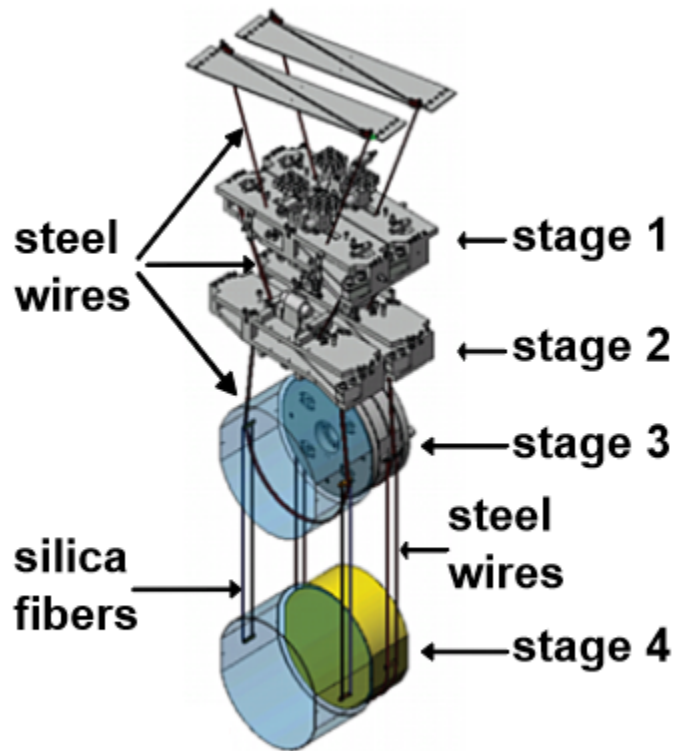


FIGURE 20. The quadrupole suspension system for the Advanced LIGO test masses, the End Test Masses (ETMs) and the Input Test Masses (ITMs) [13].

in the DARM spectrum as spikes at approximately 1000 Hz as shown in red in Figure 22 and also as horizontal lines in Figure 21, but the exact frequency of each mode is not obvious even when examining the spectrum at high frequency resolution because there are often several neighboring modes separated by a fraction of a Hz. It is also not apparent from the spectrum which spike is associated with each test mass. The only way to find these associations is to actuate with a damping filter on each test mass at each frequency peak and observe if the peak is driven up or down. If the peak in the DARM spectrum changes as a result of actuating on a specific test mass, then that peak can be associated with that test mass, even if the filter in use is not optimal.

Mode	ETMX	ETMY	ITMX	ITMY
1	1006.439	1000.061	995.177	991.641
2	1006.745	1000.294	995.462	991.828
3	1010.356	1000.307	998.018	994.801
4	1010.581	1000.423	998.083	995.053
5	1011.063	1009.932	1001.843	997.618
6	1013.869	1017.985	1001.940	997.785
7	1014.091	1018.238	1002.859	998.967
8	-	-	1003.120	-

TABLE 1. The frequencies of the 2nd order violin modes in O3. These are measured in Hz and entries of ‘-’ indicate that the value is not known. The reason that the frequencies of specific violin modes are not known is that they are not routinely rung up and sources of noise in DARM, so their frequencies are not obvious to spot. Notice also the proximity of certain modes on the same test masses, specifically modes 2 and 3 on ITMY.

A table of the second order violin mode frequencies is presented in Table 1. These frequencies are originally reported in [72]. These frequencies are set by the properties in the fused silica suspensions of the test masses, and are found through a trial-and-error method of actuating on each test mass to see which one changes the spectrum. The difficulty of some of the modes clustered tightly together is illustrated by modes 2 and 3 of ITMY, which have frequencies 1000.294 Hz and 1000.307 Hz respectively, and appear as being only one spike in DARM, unless the DARM spectrum is taken at higher frequency resolution, which requires more time in which the damping filter is applied. We experimented with both using two filters which were .005 Hz wide so as not to drive up the neighboring mode, and also using a wider filter to address both modes simultaneously.

Once establishing the frequency of the 32 violin modes, and determining which mode is associated with which test mass, we make both monitoring and damping filters and add them to the violin mode guardian. Each of these filters

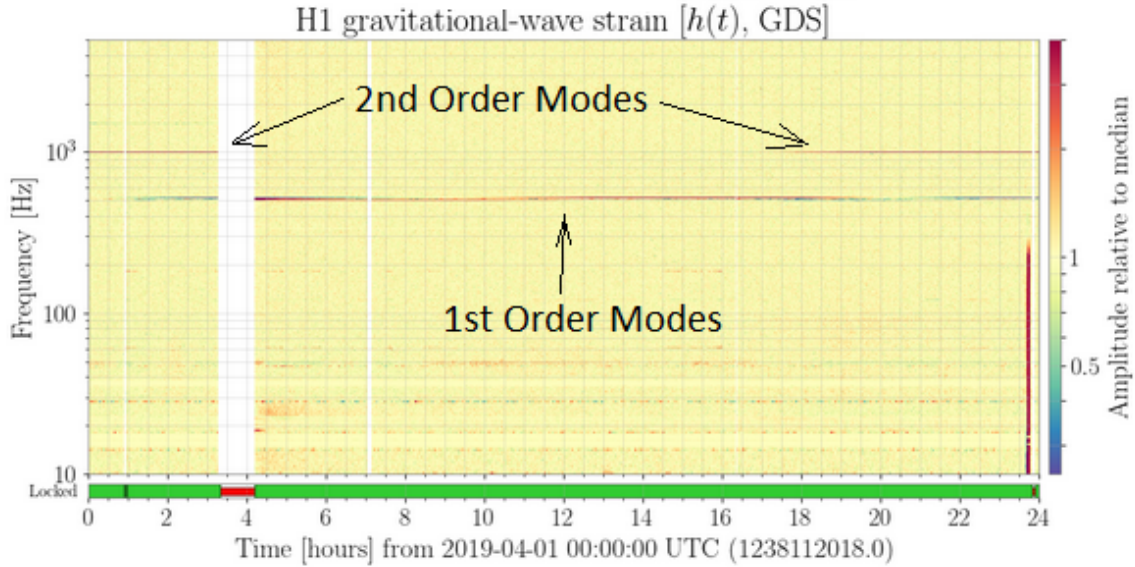
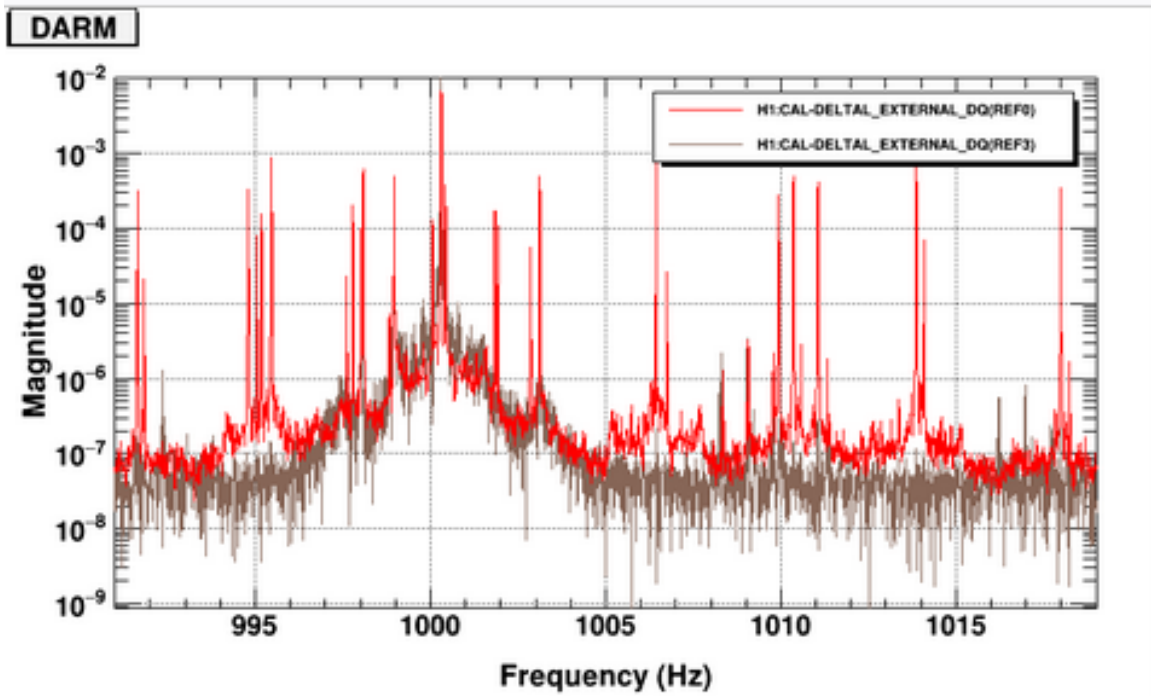


FIGURE 21. The normalized gravitational-wave strain data with both the first and second-order violin modes present at approximately 500 Hz and 1000 Hz, respectively. The strength of these modes decays over time, as a result of the automated damping filters.

has a gain and an angle which defines it, and a frequency band on which it actuates/monitors. We were able to find filters for most of these modes which could be automated and effectively begin damping at the time of the lock, but there were a couple of modes for which a consistently effective filter could not be found and automated. The benefits from this system can be seen in the strain data in Figure 21.

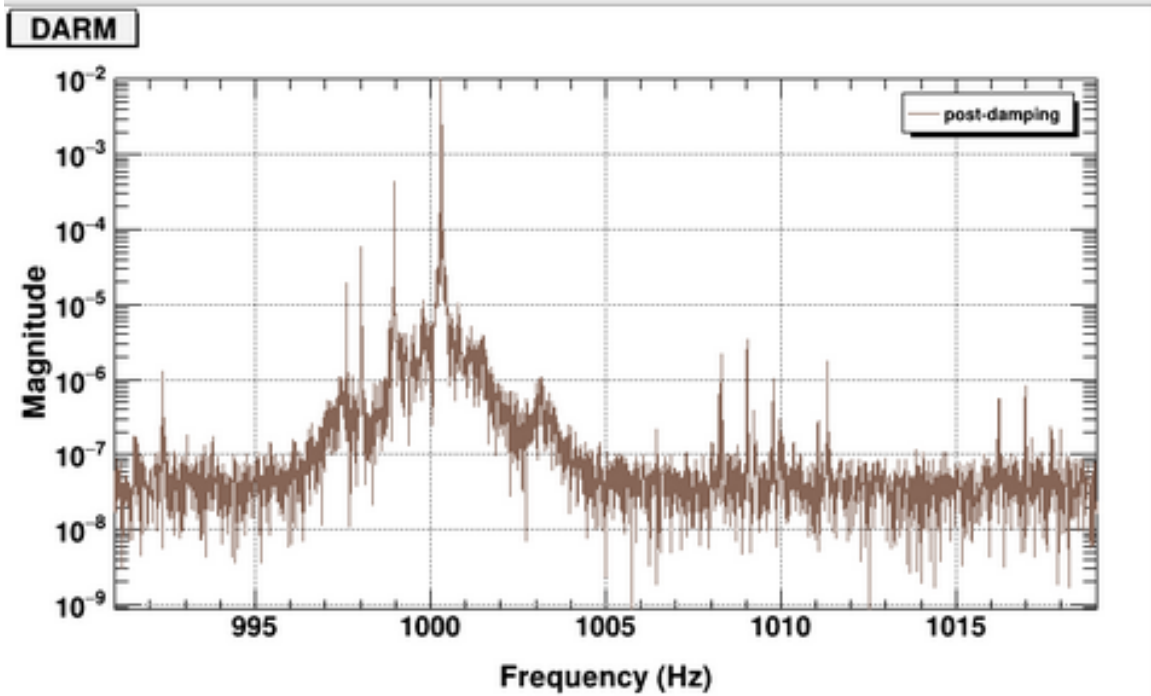
Figure 22 shows the second order violin modes before (red) and after (brown) the damping filters are applied. We see from the difference in the red and brown spectra in the top plot that we have some broader-band gains in sensitivity near 1000 Hz. The bottom plot only displays the spectrum after approximately 30 minutes of damping. We do not see the same high-Q spikes in the spectrum, indicating that the damping has been effective at lowering most of the second-order violin modes.



*T0=01/03/2019 21:55:03

Avg=423

BW=0.0117166



T0=01/03/2019 22:27:47

Avg=423

BW=0.0117166

FIGURE 22. The 2nd order violin modes at H1 before and after the damping filters were applied.

CHAPTER III

O3 MAGNETAR SEARCH

Abstract: The third observing run of Advanced LIGO and Virgo contained 16 magnetar x-ray flares which happened when at least two detectors were in observation mode. We motivate two different searches for gravitational waves patterned after the searches from the second observing run; these are the short-duration (milliseconds to seconds) search and the long-duration (hundreds of seconds) searches. We discuss specific changes to the search from O2 and the sensitivity benefits from these changes. Neither search finds evidence of a gravitational wave. We use the detector sensitivities to place upper limits on the root-sum-squared gravitational-wave strain amplitude and corresponding gravitational-wave energy, above which a gravitational-wave could be detected with 50% probability. The most constrictive strain upper limit for the long-duration search is $\approx 9 \times 10^{-23} \text{ Hz}^{-\frac{1}{2}}$, and the most constrictive energy upper limit for the short-duration search is $\approx 1 \times 10^{46} \text{ erg}$. The gravitational-wave strain sensitivity increased over the O2 search by factors ranging from 1.1 to 1.7.

3.1 Introduction

The third observing run (O3) of Advanced LIGO and Virgo was split into two parts, extending from April 1st, 2019 to September 30th, 2019, and from November 1st, 2019 to March 27th, 2020, when it was ended prematurely due to the Covid-19 pandemic. These two segments (O3a and O3b) are separated by a month during which the detectors were commissioned to improve and maintain high sensitivity. While O3a saw no magnetar activity, O3b contained 22 magnetar x-ray flares from

two identified sources, SGR 1935+2154, and SGR J1818.0–1607, as well as four flares from an unknown source which was presumed to be a magnetar (three of which took place with at least two detectors observing).

The necessary condition for the production of gravitational waves is a non-zero mass quadrupole moment, and if these flares were to excite non-radial modes in the cores of their respective magnetars, then gravitational waves might be produced. The fundamental pressure mode (f -mode) is the mode that would produce GW's most readily detectable by ground-based detectors such as LIGO and Virgo. Early magnetic field re-arrangement models which examined the energy reserves available in the magnetic field were optimistic that an f -mode could emit up to 10^{49} ergs in gravitational-wave energy[44, 48]. Emission would happen over the course of ≈ 100 ms, in the frequency range of about $\approx 1 - 3$ kHz [35], which is well within the LIGO/Virgo observation band. More intricate models used analytic[73] and numerical relativity simulations and showed that even though the magnetic field contains sufficient energy to make a detectable GW, the f -mode energy that would couple to a gravitational wave would be too low to be detected by current facilities.

Other radial oscillatory modes can be excited in the star as well as the f -mode, but would provide gravitational waves which are ill-suited for a GW search. These include surface gravity modes (g -modes) which would be lower frequency than the f -modes, but with too small of an amplitude to produce a GW with any possibility of detection. The neutron star could also contain Alfvén modes, in which the restoring force is provided by the magnetic field. These have only been studied in the context of magnetar giant flares. The GW's associated with Alfvén modes would be longer-duration, with the oscillation frequency

related to the rise time of the x-ray giant flare [45, 49, 74, 75]. Alfvén waves are interesting, yet illusive, candidates for a gravitational-wave search because their amplitude and damping time are largely unknown; any search for longer-duration gravitational waves should not be based on physical models which predict specific waveforms, and instead should be able to detect gravitational waves from a broad parameter space in order to be effective.

Gravitational waves have not previously been detected in coincidence with any EM activity from a magnetar. The first of these searches was over Initial LIGO data from 2004, when SGR 1806-20 exhibited a giant flare during LIGO observation time [76, 77], accompanied by a forest of smaller flares which began and ended within approximately a minute of the giant flare. A search for GW's associated with the giant flare yielded energy upper limits of $10^{46} - 10^{52}$ ergs [78, 79], and a search for consistently present short-duration GW's was conducted through stacking the six brightest x-ray flares in the surrounding burst forest [80]. This still didn't yield a detection, but did somewhat lower the upper limits. Another 2011 search over bursts from six different magnetars [81] lowered the energy upper limits to a range of $10^{44} - 10^{47}$ ergs. There was a renewed effort at detecting short-duration gravitational waves from magnetar flares in the second observing run of Advanced LIGO and Virgo (O2), when a search was performed over four magnetar flares, three of which were from SGR 1806-20, although they were not accompanied by a giant flare [82, 83].

The x-ray tail of the 2004 giant flare, shown in Figure 2, did have an interesting feature which informed another type of gravitational-wave search. Quasi-Periodic Oscillations (QPOs) were observed in the x-ray counts for hundreds of seconds following the giant flare. These QPO's ranged in frequency from

18 to 2384 Hz, and each lasted for tens to hundreds of seconds. This inspired gravitational-wave follow-up searches for signals with similar properties; near-periodicity would indicate monochromaticity in the corresponding GW, and the duration of the QPOs necessitates a search for similarly long-duration GW's.

The first such long-duration search gave gravitational-wave energy upper limits of 10^{46} ergs [84], and a subsequent narrow-band search over the QPO frequencies restricted these upper limits further [85]. A search method was developed in 2017 using data from LIGO's sixth Science Run (S6) [86, 87] for a background, and applied to four bursts from S6 and four other bursts from O2 [82, 83].

In this chapter we present the methods and results of a search for GW's coincident with flaring magnetars in O3 [14, 88]. We describe the x-ray flare data and the magnetars that emitted them, and we describe the search methods used to search for gravitational waves of varying properties. We give the energy upper limits, and compare them to those of O2, and give an astrophysical interpretation.

3.2 Magnetar Flares in O3 LIGO and Virgo Data

The second half of the O3 observing run saw 26 different magnetar x-ray flares [1] coming from two different magnetars, SGR 1935+2154 and J1818.0-1607, and an unknown source also assumed to be a magnetar. The necessary condition to perform a gravitational wave follow-up search is that two of the detectors are in observation mode, and that there is a reasonable level of data quality. Only 16 of the bursts in O3 met these conditions, and were included in this study. A full list of these bursts is shown in Table 2.

Burst	Source	Date	Time (UTC)	Detectors	Eiso (erg)
2651	SGR 1935+2154	Nov 04, 2019	01:54:37	H V*	-
2652	SGR 1935+2154	Nov 04, 2019	02:53:31	H V	1.4×10^{39}
2653	SGR 1935+2154	Nov 04, 2019	04:26:55	H L V	1.1×10^{39}
2654	SGR 1935+2154	Nov 04, 2019	06:34:00	H L V	-
2655	SGR 1935+2154	Nov 04, 2019	09:17:53	H L	5.7×10^{39}
2656	SGR 1935+2154	Nov 04, 2019	10:44:26	H L	2.2×10^{40}
2657	SGR 1935+2154	Nov 04, 2019	12:38:38	H L V	2.7×10^{39}
2660	SGR 1935+2154	Nov 04, 2019	15:36:47	H V	1.2×10^{39}
2661	SGR 1935+2154	Nov 04, 2019	20:29:39	H V	1.3×10^{39}
2665	SGR 1935+2154	Nov 05, 2019	06:11:08	H V	7.8×10^{40}
2668	SGR 1935+2154	Nov 15, 2019	20:48:41	L V	7.7×10^{38}
2669	-	Feb 03, 2020	03:17:11	H L V	-
2670	-	Feb 03, 2020	03:44:03	H L V	-
2671	-	Feb 03, 2020	20:39:37	H L V	-
2673	Swift J1818.0–1607	Feb 28, 2020	22:19:32	L V	-
2674	Swift J1818.0–1607	Mar 12, 2020	21:16:47	H L V	-

TABLE 2. List of bursts considered for the search

Eleven of these x-ray bursts came from SGR 1935+2154. Most of these bursts were concentrated between November 4th-5th, 2019, with only two bursts happening on November 15th, 2019. Although the electromagnetic energies of these flares (assuming isotropic emission) spanned two orders of magnitude from 7×10^{38} and 7×10^{40} ergs, none were at the energies needed to be considered a giant flare.

SGR Swift J1818-1607 was discovered much more recently on the 12th of March, 2020, after it’s flaring episode containing both of the flares that we analyze in our study [89]. The sky position was quickly located to a position very close to the galactic plane at RA(J2000) = 18h 18m 0.22s, DEC(J2000) = -16d 07’ 52.2” with an uncertainty of 2.4 arcseconds. The spin period was determined to be 1.36s [89], which is the second-shortest among the known magnetars, and the spin-down luminosity is exceptionally high at $\frac{dE}{dt} = 1.4 \times 10^{36} \frac{\text{erg}}{\text{s}}$. Observations with the 100-m

Effelsberg radio telescope suggest that the source is radio-loud, and is at a distance of between 4.8 and 8.1 kpc[17]. This study constitutes the first gravitational-wave follow-up search on J1818-1607.

The remaining four flares were detected by Fermi GBM [90, 91], and are not easily associated with any previously identified magnetar. They are each classified as likely originating from an active magnetar, although each of them has such poor sky-localization (plotted in Figure 23 along with the galactic plane and the positions of all other known magnetars) that there is no area of overlap in the 1σ error region of every individual flare.

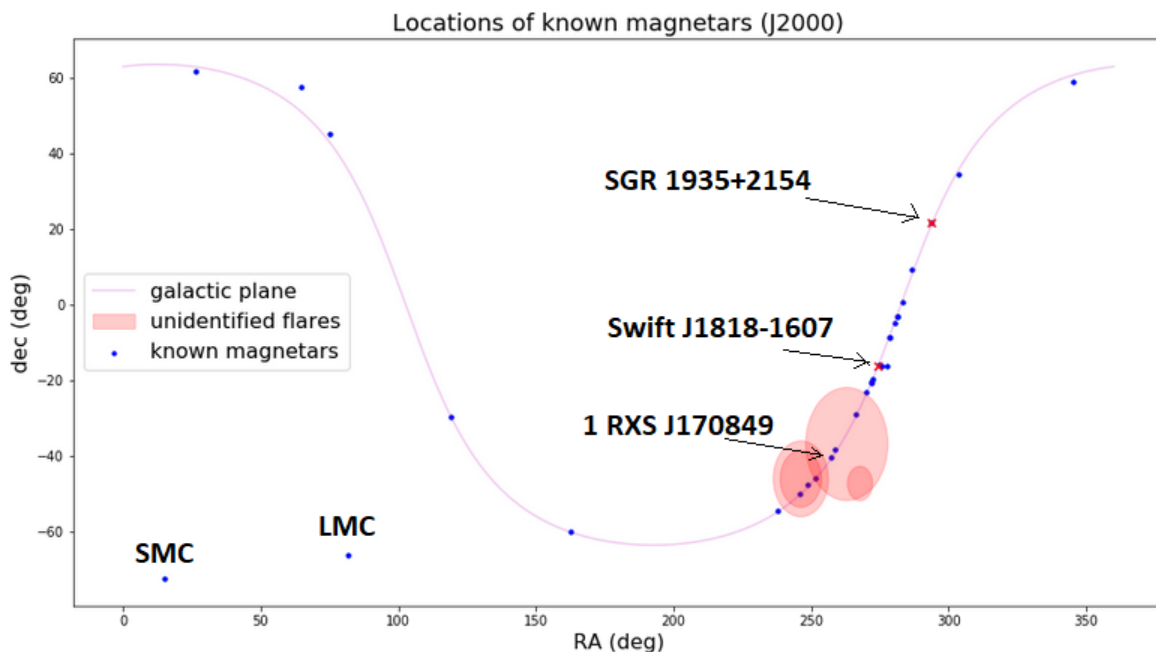


FIGURE 23. Sky locations and 1σ error regions of the four electromagnetic bursts from an unknown source. These are triggers 2669-2672 in the SGR trigger catalogue. We also mark the location of the nearest magnetar (1 RXS J170849) which falls in the 3σ uncertainty region of all four bursts. We indicate the locations of the other known magnetars including SGR 1935+2154 and Swift J1818–1607. We overlay this with the coordinates of the plane of the Milky Way, according to the J2000 coordinate system.

The four unknown flares happened in close temporal proximity, occupying the same 33 hour span of time, and we then conclude that they all originated from the same source. The error regions on each flare have to be expanded to 3σ in order for the area of common overlap to contain any known magnetars. This area is occupied by two magnetars. To obtain the most constraining results, we assume that these flares came from the closer of the two magnetars, 1 RXS J170849 at a distance of 3.8 kpc [92]. The fourth of these flares occurred at a time when we did not have a sufficient amount of usable data from two detectors, and so it cannot be included in our search, and is omitted from Table 2. Its use to us lies only with determining the probable sky location of the magnetar responsible for the other three flares.

3.3 Search Methods

The search for gravitational waves includes minimally modeled, coherent searches so as not to assume underlying physics for which there is no evidence. We search for signals which are short in duration (ms to s) and whose parameters are reminiscent of gravitational waves which could be produced by excited f -modes. We also search for longer duration signals (100s of seconds) coincident with the QPOs observed in the tails of giant flares. In each of these searches we divide the data into that which is present at and around the time of the each flare, which we call the ‘on-source’ data, and the data at times well before and after the flare which comprise the background, which we call the ‘off-source’ data. Since the sensitivity of the detector network is always in flux, we use background data that is taken symmetrically around the time of each flare, and we make the assumption that no gravitational waves exist in this data. This allows us to make a direct comparison

to the background when we calculate the probability of each gravitational-wave candidate occurring under the null hypothesis.

Here we detail the methods for each component of the search.

Short Duration Search

For the short-duration search we use x-pipeline [51, 52], which is a coherent, directional search which is most effective at detecting short-duration GW's, and has previously been used in LIGO/Virgo GW follow-up searches such as the O2 and O3 GRB searches [93, 94], the O3a FRB search [16], and the O2 magnetar search [82].

X-pipeline processes data in blocks of time, typically 256 s in length. The first and last 16 s of each of these blocks is used for whitening the data, which is done using a zero phase linear predictor error filter. X-pipeline performs fast Fourier transforms on the time-series data in each block for each detector to make time-frequency maps for each detector. The time spans of these fast Fourier transforms determine the aspect ratio of the pixels in the time-frequency map, and since the optimal aspect ratio is not known, we use time spans of $dt = \frac{1}{2^N}$ s, where $-1 \leq N \leq 7$, with 50% overlap. X-pipeline then coherently sums and squares the corresponding time-frequency maps from each detector, resulting in a new time-frequency map whose pixels have a brightness according to the coherent energy across the detector network. Because this is a targeted search, x-pipeline can combine the data from each detector α according to the time delay between the sites, Δt , and gain sensitivity by modeling the data as being a combination of coherent signal and incoherent noise:

$$d_\alpha(t + \Delta t_\alpha \hat{\Omega}) = F_\alpha^+(\hat{\Omega})h_+(t) + F_\alpha^\times(\hat{\Omega})h_\times(t) + n_\alpha(t + \Delta t_\alpha(\hat{\Omega})), \quad (3.1)$$

where n_α is the noise, $\hat{\Omega}$ is the sky-position of the incoming gravitational wave, and F^+ and F^\times are the antenna factors in the + and \times polarizations in the direction of $\hat{\Omega}$.

A detection statistic is chosen from among the coherent x-pipeline outputs. We use the standard likelihood, E_{SL} , defined in Equation 2.17 of [51], which is consistent with previous burst searches. Further discussion of coherent energy outputs are given in Chapter 5.2. A cutoff value of the detection statistic is determined such that 1% of the pixels in each coherent time-frequency map fall above the threshold. We call these ‘bright pixels’, and combine all neighboring bright pixels into ‘clusters’, where each cluster is potentially a GW. Each measure of energy for a cluster is the sum across the cluster’s constituent pixels of that measure of energy. More details on the specific energies and clustering algorithms can be found in Chapter 5.2. A maximum possible number of clusters is set through a cluster-rate of 1 cluster per 4 seconds averaged across each block of time. Low-energy clusters are discarded until the number of remaining clusters satisfies this cluster-rate.

This is done for the 256 s in the on-source window, and every 256 s block of time in the off-source data. The background is expanded using time lags and circular time slides, both of which are explained more thoroughly in Section 5.2. The end result of this procedure is a distribution of clusters in the on-source window, and in the background. Cuts are applied to these clusters to distinguish between potential signals and background noise.

The short-duration search consists of two components: the ‘centered’ search which has an 8s on-source window centered on the time of the flare, and a ‘delayed’ search in which the on-source window is 500 s long, and begins 4 s after the time

of the flare. The two-component search allows us to optimize our sensitivity at the time of the flare, and also to have some sensitivity to short-duration signals in the hundreds of seconds after the flare time. In both components of the search, we inject waveforms reminiscent of gravitational-wave transients into the raw data and record the efficiency with which x-pipeline is able to detect them as a way to measure our sensitivity. More details on injections are given in Chapter 3.5.

The centered search has an on-source window from $[-4s,+4s]$ around the time of the flare and has search parameters set to optimize its sensitivity in the parameter space where one would expect to find the gravitational waves produced by f-modes, as well as having some sensitivity to lower frequency signals. The frequency range extends from 50-4000 Hz, with a sampling rate of 8192 Hz. We want the search to be most sensitive at the time with the most EM emission, as the most probable time of GW emission. This increase in sensitivity is achieved in the centered search because the false alarm probability (FAP), or p-value, is the quantity that is standardized to measure the sensitivity of the search. The FAP and False Alarm Rate (FAR) are related through:

$$\text{FAP} = \text{FAR} \times T \tag{3.2}$$

where T represents the length of the on-source window. So since the FAP is standardized between the two searches, we see that:

$$\text{FAR}_{\text{delayed}} = \text{FAR}_{\text{centered}} \times \frac{T_{\text{centered}}}{T_{\text{delayed}}} \tag{3.3}$$

$$= .016 \times \text{FAR}_{\text{centered}}. \tag{3.4}$$

The detection statistic threshold is then higher for the delayed search due to its longer on-source window.

The delayed search extends from $[+4s,+504s]$ after the flare time, and exists with the goal of detecting gravitational waves emitted from f -modes that might have been rung up by torsional modes in the magnetar’s crust. Even though none of the flares in our study are giant flares (and do not exhibit QPOs in their tails), if their internal driving mechanism is a diminished version of that which causes the giant flares, then it might be reasonable to assume that similar surface conditions, including torsional modes, exist in our flares. The frequency of the search matches that of the centered search, but the block time is set to 256 s.

X-pipeline is a targeted search and takes as a parameter an angular error region on the sky localization of the source. Both of our known sources, SGR 1935+2154 and J1818.0-1607, are well-localized sources and can therefore be run with zero error region since the error in sky direction from a GW search is so much greater than the uncertainty on the source position. There are, however, specific delayed on-source runs which display injection recovery inefficiencies with an approximately 224 s period in the higher frequency waveforms, shown in Figure 24. This can be explained through the 256 s block time in which the data is analyzed. Sixteen s on each end of the block time is removed for whitening, leaving 224 s in the middle for analysis. The earth rotates approximately 0.93 degrees during that time, which means that for a 0% error region in the position of the source, x-pipeline interprets the injection as coming from the wrong sky direction when it is injected near the edge of the 224 s usable span of time. We can allow for more flexibility in the sky localization by pretending that the source is not well-

localized and instead introducing an error region of 1 degree, which causes this periodicity to vanish.

We can also see a notable difference in the efficiency curves before and after the error region is introduced in Trigger 2668 (shown in Figure 25), with the injection recovery efficiency approaching unity with the non-zero error region. The runs which include this error region are specified in Table 3.

Both the centered and delayed searches use 3 hours of off-source data taken symmetrically about the time of the flare to be used to make the background. We make exceptions to this in the case of there being multiple flares within the same 3h span of time (thus forcing us to include a neighboring flare time and potentially its corresponding GW in the background), in which case we either reduce the background or take it asymmetrically from before of after the flare. These modifications to the background size and symmetry have been noted in Table 3. More details on x-pipeline can be found in Chapter 5.2.

Long Duration Search

The long-duration search targets the section of parameter space most likely to contain a GW coincident with the quasi-periodic oscillations in the tails of giant flares. These QPOs last for hundreds of seconds and have been observed at frequencies ranging from 18 to 2384 Hz.

For this search we use the Stochastic Transient Analysis Multi-detector Pipeline (STAMP) [95]. STAMP calculates the cross-power of the two most sensitive detectors in the network and uses it to produce a time-frequency map where the brightness of each pixel indicates the signal-to-noise ratio (SNR) of that pixel. We then use STAMP's seedless clustering algorithm to generate a sufficiently

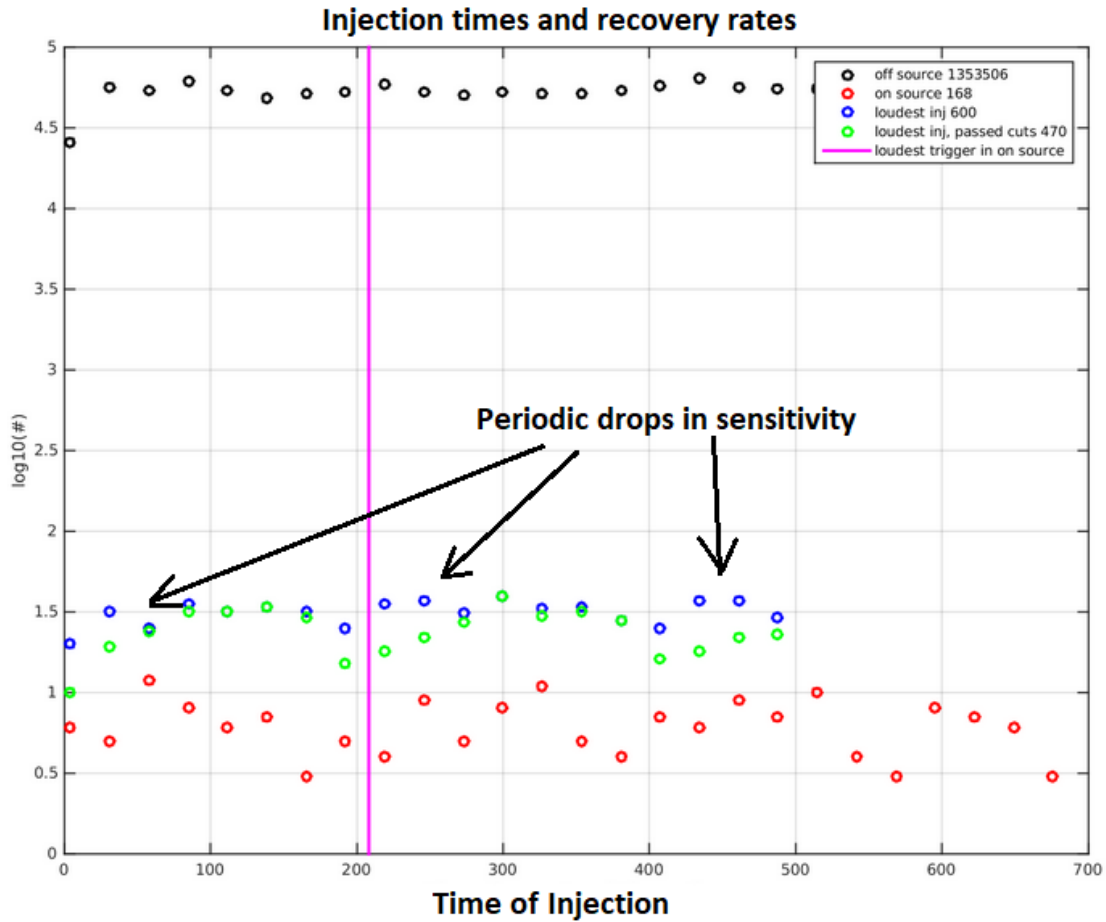


FIGURE 24. A histogram of the time distribution at which the 1600 Hz sine-Gaussian injections were made into the dummy on-source window of Trigger 2668, and rates at which they were recovered. 1200 injections are made at each injection amplitude, the loudest 600 of which are shown here in blue to be approximately uniformly distributed in time. Only 470 of these (in green) passed all of the pipeline cuts. We see repeating occurrences where the injections have a noticeably decreased probability of passing all the pipeline cuts, and this happens with approximate 224 s periodicity. We see the efficiency curves increase in Figure 25, and we also see the periodicity in injection recovery percentage vanish.

Burst	Delayed on-source search	Centered on-source search
2652	Background Asymmetry Factor = .3726 Background length = 8090s Frequency Range = 300Hz to 4000Hz	Background Asymmetry Factor = .3858 Background length = 9056s
2653	Background Asymmetry Factor = .4711 Background length = 10790s Frequency Range = 65Hz to 4000 Hz Error Region = 1 deg.	
2655	Background Asymmetry Factor = 0.5677 Background length = 10790s	Background Asymmetry Factor = .5225 Background length = 10790s
2656	Background Asymmetry Factor = 0.4331 Background length = 10790s	Background Asymmetry Factor = .4775 Background length = 10790s
2660	Background Asymmetry Factor = 0.3421 Background length = 10790s	Background Asymmetry Factor = .3403 Background length = 10790s
2661	Error Region = 1 deg.	
2668	Error Region = 1 deg.	Frequency Range = 85 - 4000Hz
2669	Background Asymmetry Factor = 0.8993 Background length = 10790s	Background Asymmetry Factor = .854 Background length = 10790s
2670	Background Asymmetry Factor = 0.1015 Background length = 10790s	Background Asymmetry Factor = .1459 Background length = 10790s
2671		Background length = 10790s
2673	Frequency Range = 60Hz to 4000Hz Error Region = 1 deg.	

TABLE 3. Parameters used in the centered on-source and delayed on-source short-duration searches. When no value is specified, the search was run with the default parameters, including frequency ranging from 50-4000 Hz, a symmetric background window 10800s in length, and 0 degree error region. The background asymmetry factor is defined as the fraction of the background time before the burst time, with 0.5 corresponding to a symmetric background. The error region is defined as the 1σ uncertainty in the sky position of the source. Using a non-zero error region on a point source can sometimes increase the search sensitivity because it counters the effects of the earth's rotation during the on-source window.

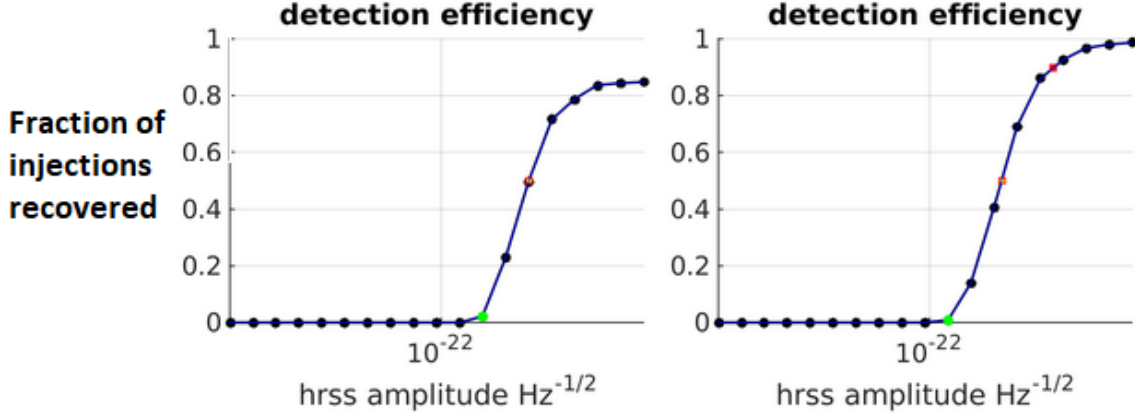


FIGURE 25. The efficiency curves of the 1600 Hz, elliptically polarized sine-Gaussian waveform injected into the off-source segment containing the most significant event (the ‘dummy on-source segment’) of trigger 2668. We use a dummy on-source for injection studies so that the sensitivity can be maximized without viewing the results, and the efficiency curve shows the fraction of injections at each h_{rss} of injection that are recovered with a higher significance than the loudest event in the dummy on-source. The plot on the left shows the efficiency curve when the pipeline is run with no uncertainty in the position of the magnetar, and we see that it asymptotic to approximately 0.9. On the right side we have the efficiency curve with 1 degree of uncertainty, and this efficiency rises to unity.

high number of clusters such that they adequately cover the time-frequency map, and the loudest of these clusters is kept, treated as a potential GW, and compared to its counterparts in the background [96].

In the on-source time-frequency map, three points in time-frequency space are randomly generated, and these define a quadratic Bezier curve, which becomes the cluster. This is repeated 2×10^7 times for a total of 2×10^7 independent clusters. To restrict ourselves to nearer monochromaticity as the QPOs suggest, we discard the clusters that vary in frequency by greater than 10%. The total SNR of each remaining cluster is then calculated by summing the SNRs of each pixel that it passes through, according to equation (3) of [96]. This then becomes the SNR of the loudest on-source cluster.

Search Name	Pipeline	On-source Window [s]	On-source Interval [s]	Off-source Window [s]	Frequency Range [Hz]
Centered on-source	x-pipeline	8	$[-4, +4]$	10,800	50 – 4000
Delayed on-source	x-pipeline	500	$[+4, +504]$	10,800	50 – 4000
Long-duration	STAMP	1604	$[-4, +1600]$	58,800	24 – 2500

TABLE 4. On-source, off-source and frequency range of searches performed. The off-source interval is centered around the magnetar burst time.

Background time-frequency maps are generated by combining 36 data segments from one detector with 36 time-shifted data segments from the second detector, for a total of 1260 maps. The loudest cluster in each map is found using the same algorithm as in the on-source, and then the loudest cluster in the on-source can be compared to the distribution of loudest clusters from each background map.

The long-duration search has an on-source window that is 1604s in duration and extends from $[-4s, 1600s]$ around the time of each flare. The frequency range of the search is 25 Hz to 2500Hz, and the background is 58,800s long, centered at the time of the flare.

A summary of the basic parameters of the short and long-duration searches is given in Table 4. It should be noted that both of the short-duration search on-source windows are contained in the on-source window of the long-duration search. We have established that the search parameters are sufficiently different so as to not encrue a trials factor. It also needs to be noted that the on-source time in the delayed search is contained in the background of the centered search. This is of greater concern, because we are then acknowledging that there might be a gravitational-wave signal in the background of the centered search. We mitigate this by performing the delayed searches first, and only proceeding with the centered

search in the absence of such a GW. X-pipeline as a built-in 16s buffer separating the on-source and off-source data, and the 16s of the delayed search contains the on-source of the centered search, so we do not need to worry about a GW from the centered search in the background of the delayed search.

3.4 Results

We now discuss the results of both the short-duration and long-duration searches. The short-duration search results are presented in terms of a p-value, which is the probability of that result happening under the null hypothesis. In practice the p-value for the short duration search is calculated as the fraction of clusters in the background which have a detection statistic that is greater than that of the loudest on-source cluster.

The results of the long-duration search are presented as the Fraction of Background Segments (FBS) in which the loudest cluster is louder than that of the on-source [14], and calculated as in Equation 3.5. The results of the short-duration search are presented as a p-value, calculated similarly to the fraction of background segments (FBS), but including all surviving events in the background.

$$\text{FBS} = \frac{N_{\geq}}{N_{\text{total}}} \quad (3.5)$$

The sensitivity of both searches is estimated by injecting waveforms into the data, and determining the amplitude of injection at which the waveforms are recovered with 50% efficiency, $h_{\text{RSS}}^{50\%}$. For x-pipeline, the injections are made into the on-source window, and are considered to be recovered when their detection statistic is greater than that of the loudest on-source event. We compute this amplitude in terms of the root-sum-squared strain, given by:

$$h_{rss} = \sqrt{\int |h_+(t)|^2 + |h_\times(t)|^2 dt} \quad (3.6)$$

where h_+ and h_\times are the two polarizations. We use the $h_{rss}^{50\%}$ value as a strain upper limit to calculate the energy upper limits, above which we can assume that there is a 50% probability of detecting an event. For the ringdown and sine-Gaussian waveforms in the short-duration search, we use the approximation for narrow-band sources given in by equation 17 of [97]:

$$E_{GW} = \frac{2}{5} \frac{c^2 \pi^2}{G} d^2 h_{rss}^2 f_0^2. \quad (3.7)$$

This equation is derived for narrow-band gravitational waves, and the ringdown and sine-Gaussian waveforms are sufficiently narrow-band for this to be an accurate approximation. The energies of WNB waveforms are derived using the isotropic emission approximation given by equation 11 of [97]:

$$E_{GW} = \frac{c^2 \pi^2}{G} d^2 h_{rss}^2 f_0^2, \quad (3.8)$$

which is made using the narrow-band approximation. We note that our WNB waveforms are not narrow-band; the first two are 100 Hz wide, and the last two are 900 Hz wide. A numerical study has shown that given the low and high frequency limits of WNB injection, the narrow-band energy approximation given in Equation 3.8 merely needs a correction factor to reach to appropriate value. These correction factors are 1.037 for the 100-200 ms waveforms, and 1.2231 for the 100-1000 ms waveforms [98].

In order to perform these calculations, we approximate the distance to SGR 1935+2154 as 9 kpc [18], the distance to J1818.0-1607 as 4.8 kpc [17], and the distance to the magnetar emitting the unknown flares as 3.8 kpc [19].

3.5 Short-Duration Results

An additional requirement to run x-pipeline is that greater than 95% of the data in the on-source window be present and of good quality, and for this reason we were able to run the short duration searches on each flare in Table 2 except for triggers 2651 and 2655, which had missing on-source data. This requirement also prevented us from running the delayed on-source search on trigger 2671. All of the remaining triggers were analyzed, and their p-values are reported in Table 5.

The lowest p-value present in the centered search is 8.6×10^{-3} from trigger 2656, and the lowest p-value present in the delayed search is 3.5×10^{-3} . Figure 26 shows the cumulative probabilities of obtaining a a specific p-value from our search randomly given how many analysis have been performed. It is obvious that both the p-values from triggers 2653 and 2656 fall furthest outside the 90% probability zone, and we discuss both the astrophysical implications and noteworthy detector characteristics and data quality of these flares in Section 3.5.

The injections in both components of the short-duration search include a series of sine-Gaussian chirplets described by [99]:

$$\begin{bmatrix} h_+(t) \\ h_\times(t) \end{bmatrix} = \frac{1}{r} \sqrt{\frac{G E_{GW}}{c^3} \frac{5}{f_0 Q} \frac{1}{4\pi^{\frac{3}{2}}}} \times \begin{bmatrix} (1 + \cos^2 \iota) \cos(2\pi f_0 t) \\ 2 \cos \iota \sin(2\pi f_0 t) \end{bmatrix} \exp \left[-\frac{(2\pi f_0 t)^2}{2Q^2} \right] \quad (3.9)$$

Burst	Long-Duration FBS	Centered (8 s) p-value	Delayed (500 s) p-value
2651	9.1×10^{-1}	-	-
2652	2.1×10^{-1}	1.0	4.1×10^{-1}
2653	7.7×10^{-1}	1.8×10^{-2}	3.5×10^{-3}
2654	8.5×10^{-1}	9.9×10^{-2}	6.6×10^{-1}
2655	7.8×10^{-1}	1.0	7.3×10^{-1}
2656	9.7×10^{-1}	8.6×10^{-3}	5.2×10^{-1}
2657	1.6×10^{-1}	6.7×10^{-2}	4.8×10^{-1}
2660	2.2×10^{-2}	4.8×10^{-1}	4.9×10^{-1}
2661	9.0×10^{-1}	1.9×10^{-1}	7.4×10^{-1}
2665	8.2×10^{-1}	-	-
2668	9.9×10^{-1}	1.0	4.3×10^{-1}
2669	-	1.0	6.3×10^{-1}
2670	-	2.9×10^{-1}	7.8×10^{-1}
2671	-	3.4×10^{-1}	-
2673	6.8×10^{-1}	1.0	4.8×10^{-1}
2674	5.9×10^{-1}	1.0	5.0×10^{-2}

TABLE 5. The resulting FBS and p-values from both the short-duration and long-duration searches [14]. A p-value of 1 indicates that there were no clusters in the on-source window that survived the veto cuts. x-pipeline constrains the number of loud clusters it can generate to a rate of 1 cluster per 4 s, meaning that it is more probable for a shorter on-source window not to have any surviving clusters. Table entries of ‘-’ indicate that no value is recorded, because no search was run. Bursts 2669-2671 are from the magnetar with no identified source, and the long-duration search was not conducted on these. Bursts 2651 and 2665 were missing segments of data from the on-source window such that the short-duration searches could not run, and burst 2671 had data missing in the delayed on-source window such that the delayed on-source search could not be run.

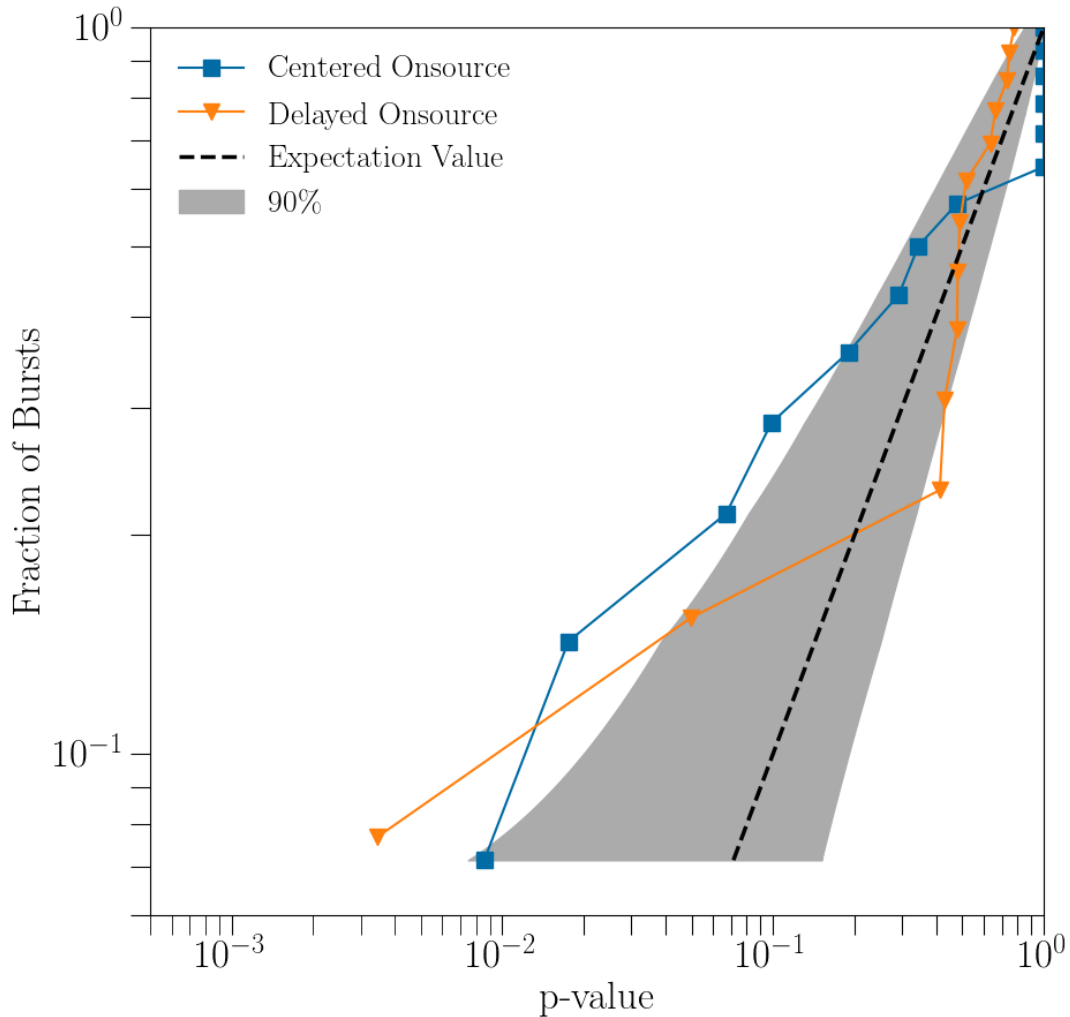


FIGURE 26. The p-values of the centered and delayed on-source searches plotted along with the cumulative probability of each p-value [14]. The dotted line indicates the expectation value for each p-value, and the shaded band indicates the region in which 90% of the p-values should fall. We note several analyses with p-value=1 in the centered search – this is the case because none of those on-source times contained loud clusters that survived the x-pipeline cuts. The lowest p-values in the delayed and centered searches are coming from Trigger 2653 and 2656 respectively, and are discussed in greater detail in Section 3.5.

where f_0 is the central frequency of the injection, t is the time elapsed since the waveform's peak intensity, r is the distance to the source, and ι is the inclination of the source as measured along the angular momentum axis, where $\cos \iota = 1$ indicates optimal orientation for gravitational-wave detection. Q is the decay constant, indicating how many cycles have a large quadrupolar mass moment. This equation is recreated in the x-pipeline injection code using a time constant, $\tau = \frac{Q}{2^{\frac{3}{2}}\pi f_0}$:

$$h(t) = h_{rss} \exp\left(\frac{-t^2}{4\tau^2} + i2\pi t f_0\right) \frac{1}{(2\pi\tau^2)^{\frac{1}{4}}} \quad (3.10)$$

$$h_+(t) = \text{real}(h) \times \frac{1}{2}(1 + \cos^2 \iota) \quad (3.11)$$

$$h_\times(t) = \text{imag}(h) \times \cos \iota. \quad (3.12)$$

The short-duration search injects Sine-Gaussian chirplet waveforms with elliptical polarization ($-1 \leq \cos \iota \leq 1$) at central frequencies 70 Hz, 90 Hz, 145 Hz, 290 Hz, 1100 Hz, 1600 Hz, 2020 Hz, 2600 Hz, 3100 Hz, and 3560 Hz. These frequencies were chosen to span the frequency range where we would expect f -modes, but also to avoid the known sources of instrumental noise in all three detectors such that they can provide accurate sensitivity estimates. The time constant is standardized to be $\tau = \frac{1}{f_0}$, which makes $Q = 2^{\frac{3}{2}}\pi \approx 8.89$.

We also inject sine-Gaussian waveforms which are nearly circularly polarized, allowing ι to range from 0.996 to 1, which corresponds to ι varying by up to 5 degrees from circular polarization, at both 1600Hz and 2020Hz. We also inject white noise burst (WNB) waveforms, which are Gaussian-modulated noise bursts that are white across a certain frequency band. We inject four of these, at frequencies 100-200Hz and 100-1000Hz, and time durations 11ms and 100ms.

For the centered search we also inject ringdown waveforms, categorized by an exponentially damped sinusoid:

$$h_+ = \frac{h_{peak}}{2}(1 + \cos^2 \iota) \cos(2\pi t f_0) \times \exp\left(-\frac{t}{\tau}\right) \quad (3.13)$$

$$h_\times = h_{peak} \cos(\iota) \sin(2\pi t f_0) \times \exp\left(-\frac{t}{\tau}\right). \quad (3.14)$$

We inject 6 waveforms from the ringdown series, all of which were elliptically polarized with $\cos \iota$ drawn from a uniform distribution ranging from -1 to 1. We set the central frequencies of these waveforms to be 1500Hz (to match the O2 search), 1590Hz for ease of comparison to the search over the 2004 giant flare, and 2020 Hz to be compared with the sine Gaussian injection series. Each frequency had two waveforms injected at characteristic times 100ms and 200ms. Each injected ringdown waveform is preceded by a ‘ringup’ with a characteristic time $\frac{\tau}{10}$.

1200 injections are made for each waveform at each injection amplitude spanning three orders of magnitude. The detection efficiencies are linearly interpolated to find $h_{\text{rss}}^{50\%}$. These values for the most sensitive analysis as measured by each waveform in the centered search can be found in Tables 6, 7, and 8 for SGR J1818.0-1607, SGR 1935+2154, and the unknown source respectively. The analogous values for the delayed search can be found in Tables 9, 10, and 11 for each source respectively.

In Table 12 we give the energy upper limit for each trigger for both the sine-Gaussian waveform at 1600Hz, and the ringdown waveform at 1590Hz. We also give the energy ratio upper limit for the triggers for which we have electromagnetic energy information.

Injection Type	Frequency (Hz)	Duration/ τ (ms)	Burst	Centered (8 s)	
				$h_{\text{rss}}^{50\%}$ ($\text{Hz}^{-1/2}$)	$E_{\text{GW}}^{50\%}$ (erg)
Sine Gaussian	70	14.3	2674	6.9×10^{-23}	8.2×10^{42}
Sine Gaussian	90	11.1	2674	6.1×10^{-23}	1.1×10^{43}
Sine Gaussian	145	6.89	2674	5.7×10^{-23}	2.4×10^{43}
Sine Gaussian	290	3.45	2674	5.9×10^{-23}	1.0×10^{44}
Sine Gaussian	1100	0.909	2674	1.3×10^{-22}	7.5×10^{45}
Sine Gaussian	1600	0.625	2674	2.0×10^{-22}	3.7×10^{46}
Sine Gaussian	2020	0.495	2674	2.7×10^{-22}	1.0×10^{47}
Sine Gaussian	2600	0.385	2674	3.5×10^{-22}	2.9×10^{47}
Sine Gaussian	3100	0.323	2674	4.4×10^{-22}	6.4×10^{47}
Sine Gaussian	3560	0.281	2674	5.3×10^{-22}	1.2×10^{48}
Sine Gaussian*	1600	0.625	2674	1.2×10^{-22}	1.2×10^{46}
Sine Gaussian*	2020	0.495	2674	1.5×10^{-22}	3.2×10^{46}
Ringdown	1590	100	2674	2.1×10^{-22}	3.8×10^{46}
Ringdown	1590	200	2674	2.1×10^{-22}	4.0×10^{46}
Ringdown	1500	100	2673	2.6×10^{-22}	5.3×10^{46}
Ringdown	1500	200	2673	2.6×10^{-22}	5.3×10^{46}
Ringdown	2020	100	2674	2.6×10^{-22}	9.3×10^{46}
Ringdown	2020	200	2674	2.5×10^{-22}	8.7×10^{46}
WNB	100-200	11	2674	3.7×10^{-23}	2.8×10^{43}
WNB	100-200	100	2674	5.3×10^{-23}	5.7×10^{43}
WNB	100-1000	11	2674	7.0×10^{-23}	1.6×10^{45}
WNB	100-1000	100	2674	1.2×10^{-22}	4.6×10^{45}

TABLE 6. The central frequencies and damping times are shown for each of the waveforms used in the centered on-source search. We also show the most constraining $h_{\text{rss}}^{50\%}$ for each waveform considering only bursts from J1818.0-1607, and calculate the corresponding $E_{\text{GW}}^{50\%}$ using Equation 3.7 (and Equation 3.8 for the WNBs) assuming a source distance of 4.8 kpc [17]. We also provide the corresponding ratios of gravitational wave energy to EM energy, using the isotropic energies given in Table 2. All waveforms have elliptical polarization except for those marked by *, which are circularly polarized, and the WNBs, which have isotropic polarization.

Injection Type	Frequency (Hz)	Duration/ τ (ms)	Burst	Centered (8 s)	
				$h_{\text{rss}}^{50\%}$ ($\text{Hz}^{-1/2}$)	$E_{\text{GW}}^{50\%}$ (erg)
Sine Gaussian	70	14.3	2655	7.3×10^{-23}	3.2×10^{43}
Sine Gaussian	90	11.1	2668	5.8×10^{-23}	3.3×10^{43}
Sine Gaussian	145	6.89	2668	5.7×10^{-23}	8.4×10^{43}
Sine Gaussian	290	3.45	2655	5.8×10^{-23}	3.5×10^{44}
Sine Gaussian	1100	0.909	2655	1.3×10^{-22}	2.6×10^{46}
Sine Gaussian	1600	0.625	2655	1.9×10^{-22}	1.1×10^{47}
Sine Gaussian	2020	0.495	2655	2.4×10^{-22}	9.2×10^{46}
Sine Gaussian	2600	0.385	2655	3.3×10^{-22}	9.2×10^{47}
Sine Gaussian	3100	0.323	2655	4.1×10^{-22}	2.0×10^{48}
Sine Gaussian	3560	0.281	2655	5.1×10^{-22}	4.0×10^{48}
Sine Gaussian*	1600	0.625	2655	1.1×10^{-22}	3.8×10^{46}
Sine Gaussian*	2020	0.495	2655	1.4×10^{-22}	9.6×10^{46}
Ringdown	1590	100	2655	1.9×10^{-22}	1.1×10^{47}
Ringdown	1590	200	2655	1.8×10^{-22}	9.6×10^{46}
Ringdown	1500	100	2668	2.5×10^{-22}	1.8×10^{47}
Ringdown	1500	200	2668	2.3×10^{-22}	1.5×10^{47}
Ringdown	2020	100	2655	2.2×10^{-22}	2.4×10^{47}
Ringdown	2020	200	2655	2.2×10^{-22}	2.3×10^{47}
WNB	100-200	11	2668	3.8×10^{-23}	1.0×10^{44}
WNB	100-200	100	2668	5.3×10^{-23}	2.0×10^{44}
WNB	100-1000	11	2655	6.7×10^{-23}	5.1×10^{45}
WNB	100-1000	100	2655	1.1×10^{-22}	1.5×10^{46}

TABLE 7. The central frequencies and damping times are shown for each of the waveforms used in the centered on-source search. We also show the most constraining $h_{\text{rss}}^{50\%}$ for each waveform considering only bursts from SGR 1935+2154, and calculate the corresponding $E_{\text{GW}}^{50\%}$ using Equation 3.7 (and Equation 3.8 for the WNBs) assuming a source distance of 9 Kpc [18]. We also provide the corresponding ratios of gravitational wave energy to EM energy, using the isotropic energies given in Table 2. All waveforms have elliptical polarization except for those marked by *, which are circularly polarized, and the WNBs, which have isotropic polarization.

Injection Type	Frequency (Hz)	Duration/ τ (ms)	Burst	Centered (8 s)	
				$h_{\text{rss}}^{50\%}$ ($\text{Hz}^{-1/2}$)	$E_{\text{GW}}^{50\%}$ (erg)
Sine Gaussian	70	14.3	2669	4.2×10^{-23}	1.9×10^{42}
Sine Gaussian	90	11.1	2669	4.0×10^{-23}	2.8×10^{42}
Sine Gaussian	145	6.89	2669	3.3×10^{-23}	5.1×10^{42}
Sine Gaussian	290	3.45	2669	3.6×10^{-23}	2.4×10^{43}
Sine Gaussian	1100	0.909	2669	7.7×10^{-23}	1.6×10^{45}
Sine Gaussian	1600	0.625	2669	1.1×10^{-22}	7.1×10^{45}
Sine Gaussian	2020	0.495	2669	1.5×10^{-22}	1.9×10^{46}
Sine Gaussian	2600	0.385	2669	2.0×10^{-22}	5.9×10^{46}
Sine Gaussian	3100	0.323	2669	2.5×10^{-22}	1.3×10^{47}
Sine Gaussian	3560	0.281	2669	2.9×10^{-22}	2.3×10^{47}
Sine Gaussian*	1600	0.625	2669	6.2×10^{-23}	2.2×10^{45}
Sine Gaussian*	2020	0.495	2669	8.6×10^{-23}	6.6×10^{45}
Ringdown	1590	100	2670	1.1×10^{-22}	6.8×10^{45}
Ringdown	1590	200	2670	1.1×10^{-22}	7.0×10^{45}
Ringdown	1500	100	2669	1.8×10^{-22}	1.6×10^{46}
Ringdown	1500	200	2671	2.7×10^{-22}	3.6×10^{46}
Ringdown	2020	100	2670	1.3×10^{-22}	1.6×10^{46}
Ringdown	2020	200	2670	1.3×10^{-22}	1.6×10^{46}
WNB	100-200	11	2669	2.2×10^{-23}	6.2×10^{42}
WNB	100-200	100	2669	3.2×10^{-23}	1.3×10^{43}
WNB	100-1000	11	2669	3.9×10^{-23}	3.0×10^{44}
WNB	100-1000	100	2669	7.1×10^{-23}	1.0×10^{45}

TABLE 8. The central frequencies and damping times are shown for each of the waveforms used in the centered on-source search. We also show the most constraining $h_{\text{rss}}^{50\%}$ for each waveform considering only bursts from the unknown source, and calculate the corresponding $E_{\text{GW}}^{50\%}$ using Equation 3.7 (and Equation 3.8 for the WNBs) assuming a source distance of 3.8 kpc [19]. We also provide the corresponding ratios of gravitational wave energy to EM energy, using the isotropic energies given in Table 2. All waveforms have elliptical polarization except for those marked by *, which are circularly polarized, and the WNBs, which have isotropic polarization.

Injection Type	Frequency (Hz)	Duration/ τ (ms)	Burst	Delayed (500 s)	
				$h_{\text{rss}}^{50\%}$ ($\text{Hz}^{-1/2}$)	$E_{\text{GW}}^{50\%}$ (erg)
Sine Gaussian	70	14.3	2673	9.2×10^{-23}	1.4×10^{43}
Sine Gaussian	90	11.1	2673	8.7×10^{-23}	2.1×10^{43}
Sine Gaussian	145	6.89	2674	8.5×10^{-23}	5.4×10^{43}
Sine Gaussian	290	3.45	2674	9.1×10^{-23}	2.4×10^{44}
Sine Gaussian	1100	0.909	2674	2.0×10^{-22}	1.7×10^{46}
Sine Gaussian	1600	0.625	2674	2.9×10^{-22}	7.5×10^{46}
Sine Gaussian	2020	0.495	2674	3.9×10^{-22}	2.1×10^{47}
Sine Gaussian	2600	0.385	2674	4.9×10^{-22}	5.7×10^{47}
Sine Gaussian	3100	0.323	2674	6.1×10^{-22}	1.2×10^{48}
Sine Gaussian	3560	0.281	2674	7.1×10^{-22}	2.2×10^{48}
Sine Gaussian*	1600	0.625	2674	1.7×10^{-22}	2.6×10^{46}
Sine Gaussian*	2020	0.495	2674	2.1×10^{-22}	6.3×10^{46}
WNB	100-200	11	2673	5.6×10^{-23}	6.5×10^{43}
WNB	100-200	100	2673	7.8×10^{-23}	1.2×10^{44}
WNB	100-1000	11	2674	1.0×10^{-22}	3.3×10^{45}
WNB	100-1000	100	2674	1.8×10^{-22}	1.1×10^{46}

TABLE 9. The central frequencies and damping times are shown for each of the waveforms used in the delayed on-source search. We also show the most constraining $h_{\text{rss}}^{50\%}$ for each waveform considering only bursts from the J1818.0-1607, and calculate the corresponding $E_{\text{GW}}^{50\%}$ using Equation 3.7 (and Equation 3.8 for the WNBs) assuming a source distance of 4.8 kpc [17]. We also provide the corresponding ratios of gravitational wave energy to EM energy, using the isotropic energies given in Table 2. All waveforms have elliptical polarization except for those marked by *, which are circularly polarized, and the WNBs, which have isotropic polarization.

Injection Type	Frequency (Hz)	Duration/ τ (ms)	Burst	Delayed (500 s)	
				$h_{\text{rss}}^{50\%}$ ($\text{Hz}^{-1/2}$)	$E_{\text{GW}}^{50\%}$ (erg)
Sine Gaussian	70	14.3	2656	8.5×10^{-23}	4.4×10^{43}
Sine Gaussian	90	11.1	2656	7.4×10^{-23}	5.5×10^{43}
Sine Gaussian	145	6.89	2656	6.6×10^{-23}	1.1×10^{44}
Sine Gaussian	290	3.45	2656	6.7×10^{-23}	4.7×10^{44}
Sine Gaussian	1100	0.909	2656	1.5×10^{-22}	3.4×10^{46}
Sine Gaussian	1600	0.625	2656	2.2×10^{-22}	1.6×10^{47}
Sine Gaussian	2020	0.495	2656	2.9×10^{-22}	4.3×10^{47}
Sine Gaussian	2600	0.385	2656	4.0×10^{-22}	1.3×10^{48}
Sine Gaussian	3100	0.323	2652	5.2×10^{-22}	3.1×10^{48}
Sine Gaussian	3560	0.281	2652	6.2×10^{-22}	6.0×10^{48}
Sine Gaussian*	1600	0.625	2656	1.3×10^{-22}	5.2×10^{46}
Sine Gaussian*	2020	0.495	2656	1.7×10^{-22}	1.4×10^{47}
WNB	100-200	11	2656	4.1×10^{-23}	1.2×10^{44}
WNB	100-200	100	2656	6.1×10^{-23}	2.7×10^{44}
WNB	100-1000	11	2656	7.5×10^{-23}	6.4×10^{45}
WNB	100-1000	100	2656	1.5×10^{-22}	2.4×10^{46}

TABLE 10. The central frequencies and damping times are shown for each of the waveforms used in the delayed on-source search. We also show the most constraining $h_{\text{rss}}^{50\%}$ for each waveform considering only bursts from the SGR 1935+2154, and calculate the corresponding $E_{\text{GW}}^{50\%}$ using Equation 3.7 (and Equation 3.8 for the WNBs) assuming a source distance of 9 Kpc [18]. We also provide the corresponding ratios of gravitational wave energy to EM energy, using the isotropic energies given in Table 2. All waveforms have elliptical polarization except for those marked by *, which are circularly polarized, and the WNBs, which have isotropic polarization.

Injection Type	Frequency (Hz)	Duration/ τ (ms)	Burst	Delayed (500 s)	
				$h_{\text{rss}}^{50\%}$ (Hz $^{-1/2}$)	$E_{\text{GW}}^{50\%}$ (erg)
Sine Gaussian	70	14.3	2669	5.0×10^{-23}	2.7×10^{42}
Sine Gaussian	90	11.1	2669	4.6×10^{-23}	3.8×10^{42}
Sine Gaussian	145	6.89	2669	3.9×10^{-23}	7.0×10^{42}
Sine Gaussian	290	3.45	2669	4.1×10^{-23}	3.1×10^{43}
Sine Gaussian	1100	0.909	2669	8.8×10^{-23}	2.1×10^{45}
Sine Gaussian	1600	0.625	2670	1.3×10^{-22}	9.5×10^{45}
Sine Gaussian	2020	0.495	2669	1.7×10^{-22}	2.5×10^{46}
Sine Gaussian	2600	0.385	2669	2.4×10^{-22}	8.8×10^{46}
Sine Gaussian	3100	0.323	2670	3.0×10^{-22}	1.9×10^{47}
Sine Gaussian	3560	0.281	2670	4.0×10^{-22}	4.5×10^{47}
Sine Gaussian*	1600	0.625	2669	7.7×10^{-23}	3.3×10^{45}
Sine Gaussian*	2020	0.495	2670	9.5×10^{-23}	8.1×10^{45}
WNB	100-200	11	2669	2.5×10^{-23}	8.2×10^{42}
WNB	100-200	100	2670	3.6×10^{-23}	1.7×10^{43}
WNB	100-1000	11	2669	4.6×10^{-23}	4.4×10^{44}
WNB	100-1000	100	2669	8.2×10^{-23}	1.4×10^{45}

TABLE 11. The central frequencies and damping times are shown for each of the waveforms used in the delayed on-source search. We also show the most constraining $h_{\text{rss}}^{50\%}$ for each waveform considering only bursts from the unknown source, and calculate the corresponding $E_{\text{GW}}^{50\%}$ using Equation 3.7 (and Equation 3.8 for the WNBs) assuming a source distance of 3.8 kpc [19]. We also provide the corresponding ratios of gravitational wave energy to EM energy, using the isotropic energies given in Table 2. All waveforms have elliptical polarization except for those marked by *, which are circularly polarized, and the WNBs, which have isotropic polarization.

Burst	Source	Ringdowns		Sine Gaussians	
		$E_{\text{GW}}^{50\%}$ (erg)	Eratio	$E_{\text{GW}}^{50\%}$ (erg)	Eratio
2652	SGR 1935+2154	3.2×10^{47}	2.2×10^8	8.0×10^{46}	5.6×10^7
2653	SGR 1935+2154	2.2×10^{47}	1.9×10^8	7.3×10^{46}	6.4×10^7
2654	SGR 1935+2154	7.8×10^{47}	-	2.7×10^{47}	-
2655	SGR 1935+2154	1.1×10^{47}	1.9×10^7	3.8×10^{46}	6.6×10^6
2656	SGR 1935+2154	1.4×10^{47}	6.4×10^6	4.9×10^{46}	2.2×10^6
2657	SGR 1935+2154	1.8×10^{47}	6.6×10^7	6.4×10^{46}	2.3×10^7
2660	SGR 1935+2154	3.6×10^{47}	3.0×10^8	1.3×10^{47}	1.1×10^8
2661	SGR 1935+2154	3.2×10^{47}	2.4×10^8	1.2×10^{47}	9.0×10^7
2668	SGR 1935+2154	1.4×10^{47}	1.8×10^8	4.6×10^{46}	6.0×10^7
2669	unknown	7.3×10^{45}	-	2.2×10^{45}	-
2670	unknown	6.8×10^{45}	-	2.5×10^{45}	-
2671	unknown	2.2×10^{46}	-	7.9×10^{45}	-
2673	Swift J1818–1607	6.6×10^{46}	-	2.0×10^{46}	-
2674	Swift J1818–1607	3.8×10^{46}	-	1.2×10^{46}	-

TABLE 12. The gravitational wave energy at 50% detection efficiency for every analysis included in the centered on-source search. We include the ratio of the gravitational wave energy upper limit to the isotropic EM energy for the triggers for which the EM energy is known. We specifically present the energies pertaining to the elliptically polarized 1600 Hz sine Gaussian waveform, and the 1590 Hz ringdown waveform with 100 ms damping time. The parameters of each of these waveforms make them plausible representations of gravitational wave from excited f -modes. The burst numbers are consistent with those used in [1].

Investigations into Triggers 2653 and 2656

We now discuss the triggers with the lowest p-values in the short-duration search, trigger 2653 in the delayed search, and trigger 2656 in the centered search.

Trigger 2653: The loudest event in the delayed on-source search over this trigger was identified with a p-value of 3.5×10^{-3} , and is the outlier in Figure 26. x-pipeline identifies this event as extending from 32Hz to 224Hz, with a peak frequency of 97Hz. It began at GPS time 1256877062.14 and lasted for 31ms.

There are several arguments for why this event is likely not astrophysical. We first consider its frequency. Gravitational waves coincident with excited f -modes are thought to be in kiloHertz frequency range, and the frequency of the loud event from trigger 2653 is much too low. Although there are non-radial oscillation modes that could potentially make gravitational wave signals at the lower frequencies (such as buoyancy modes (g -modes)), these are poorly modeled and it is difficult to imagine a scenario in which one would be as loud as what we have observed.

Next we consider the parameters with which x-pipeline made its observation. This loudest event was detected as a cluster of 8 adjoined pixels in time-frequency space, when the time-scale of the fast Fourier transform used to make the map was $\frac{1}{64}$ s. The time-frequency maps are standardized such that the energy contribution to each pixel from each detector is on average 1 unit. The single-detector energy contributions were unbalanced in this case, with 165 units coming from the LIGO Hanford data (H1), and only 6 coming from the LIGO Livingston data (L1) and 13 from Virgo. The antenna factors, calculated as $F_{\text{detector}}^2 = F_+^2 + F_\times^2$ (see Chapter 2.3

for details), for each detector at the time of this flare were:

$$F_{H1}^2 = .406 \tag{3.15}$$

$$F_{L1}^2 = .085 \tag{3.16}$$

$$F_{V1}^2 = .312. \tag{3.17}$$

Since the antenna factor at LHO was 5.7 times greater than that at LLO, it would be sensible to assume that Hanford would contribute 5.7 times more energy to such an event if it were an astrophysical event in the direction of the source, SGR 1935+2154. But H1 contributed 27.5 times as much energy as L1, giving us evidence to suggest that this event was an instrumental artifact in H1.

It is also critical to note that x-pipeline detected another event in the same 500s on-source window, at approximately 50s before the loudest event. This had the same p-value, but was slightly higher frequency at 224Hz. It also had a disproportionately high energy contribution from H1. Although x-pipeline does not reconstruct the loudest events in time-frequency space to show their morphology, we make spectrograms of the H1 data at the time of these loudest two events and observe that each of them has a loud and low-frequency noise artifact at approximately .3s from the time of the event, neither of which was picked up by x-pipeline (possibly due to a lack of coherence).

It is reasonable to wonder whether there might be a class of double-glitches in H1 to which these two events belong. We use Omicron [100], gravitational-wave transient software, to search for more double-glitches in the H1 in the days surrounding Trigger 2653, and find more instances of double-glitches spaced out by .15 to .3 s in the surrounding time. In Figure 27 we include the spectrogram of

both the loudest event detected in Trigger 2653, and a nearly identical double-glitch identified by Omicron outside of the background.

It is also important to note that these double-glitches can still exist in the background of our search without significantly lowering the p-value of the on-source events. If they are incoherent with L1, they are unlikely to be counted as a loud cluster by x-pipeline. Even if they are sufficiently coherent across detectors, each only counts as one loud background event, regardless of their energetics, and has a minimal effect on the p-value.

Trigger 2656:

We now turn our attention to the detection characteristics of the loudest event seen in the centered search on trigger 2656, and discuss its implications and plausibility. A lightcurve of the electromagnetic data of trigger 2656 is shown in Figure 1. x-pipeline reports this event's frequency as ranging from 1560-1608 Hz, with a peak frequency of 1577 Hz, and the duration of the event was 63 ms. Both the frequency and damping time are within the range that we expect for gravitational waves produced by f -modes.

There are good energy arguments which imply that the loud event in trigger 2656 is unlikely to be astrophysical. x-pipeline does not return values of the h_{rss} of its loud clusters. However, we can obtain a crude approximation of the h_{rss} of this event by examining the injection recovery rates. Specifically, x-pipeline uses the significance of the loudest on-source event as the benchmark significance to determine the $h_{\text{rss}}^{50\%}$ of each waveform, so the $h_{\text{rss}}^{50\%}$ of the waveform that most closely replicates the properties of the loudest event is the best available approximation of the h_{rss} of the loudest event. Given the frequency and time duration properties of the event, we choose the ringdown waveform at 1590 Hz with a damping time of

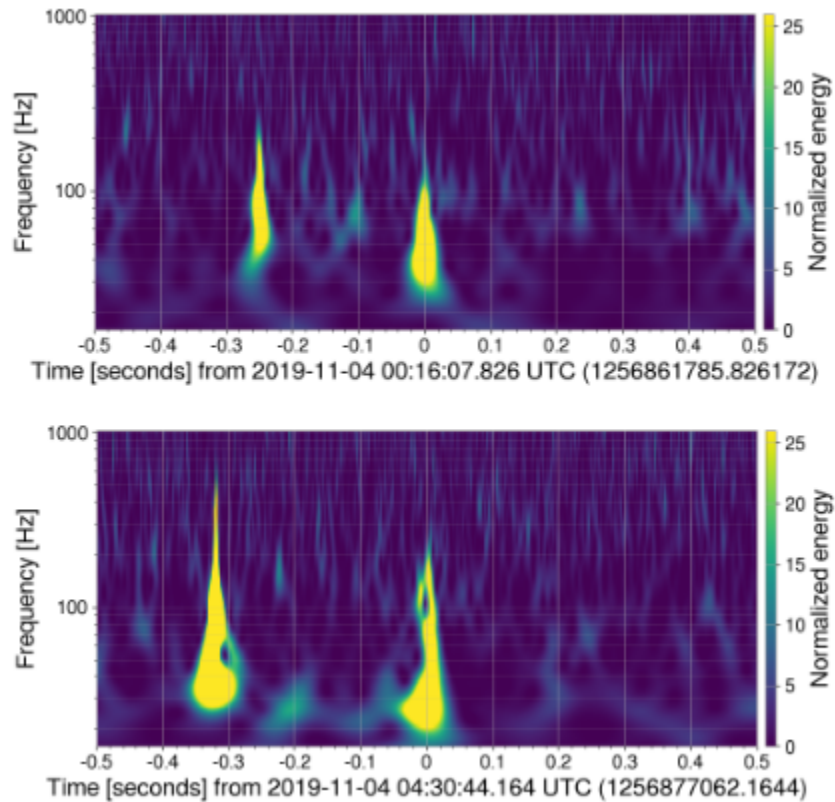


FIGURE 27. Spectrograms of H1 data at the time of the loudest event in the delayed search over trigger 2653 (top) and at the time of a Omicron-identified glitch with a similar morphology (bottom) [14]. We see that in each case the event is accompanied by a loud burst of instrumental noise in the same approximate frequency range, and separated by ~ 0.3 s. The presence of glitches with such similar properties in the background data, at other points in the on-source, and at times before and after the event bolsters the idea that new class of instrumental artifact, the double-glitch, was present around the time of trigger 2653 and was detected during the delayed search.

100 ms to be the closest waveform, and for this waveform the sensitivity is $h_{\text{rss}}^{50\%} = 2.1 \times 10^2 \text{ Hz}^{-\frac{1}{2}}$, as shown in Table 12. This indicates a gravitational wave energy of $E_{\text{GW}} = 1.4 \times 10^{47}$ erg, which in itself is not untenable, given that the binding energy of a neutron star is 10^{54} erg. But then this would imply a gravitational-wave energy to EM energy ratio of $\frac{E_{\text{GW}}^{50\%}}{E_{\text{EM}}^{\text{iso}}} \approx 10^6$, which is much greater than current models predict.

A further argument for why this event is likely not astrophysical comes when we consider that it came 3.1 s before the time of the EM burst. There are no known models that allow for gravitational waves to be emitted so long before the EM burst. We also note that, when taking into account the number of analyses that we ran, the probability of getting this low of a p-value is approximately $\approx 29\%$.

Figure 28 shows the spectrograms of the loudest event found in the centered search over trigger 2656. We see that the ambient noise is in a normal state in both H1 and L1, but that the loud trigger is only visible in Livingston. While it is true that the antenna factors for Livingston are higher than for Hanford, this difference does not account for the difference in the energies detected in L1 and H1, which makes it probable that this is an instrumental artifact in L1. We run a data quality monitoring tool, iDQ [101], and find the probability of this event being a glitch 62% and 23% in L1 and H1 respectively.

3.6 Long-Duration Results

All of the triggers listed in Table 2 met the necessary criteria for analysis in the long-duration search and were analyzed, except for triggers 2669, 2670 and 2671 from the unknown source. Given that STAMP is a computationally expensive

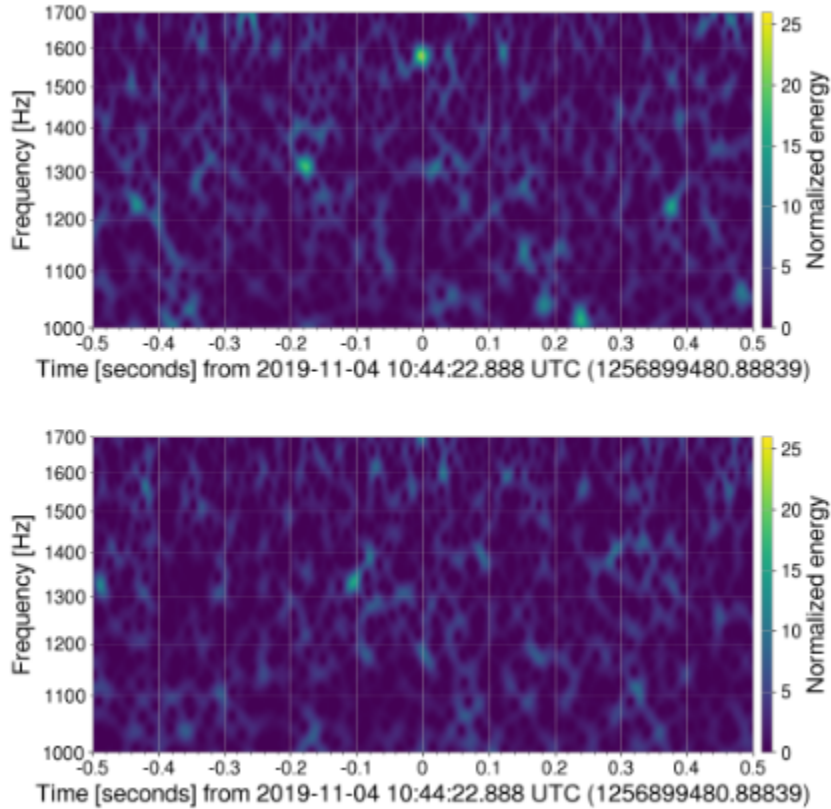


FIGURE 28. Spectrograms of the loudest event in the centered search for both L1 (top) and H1 (bottom) [14]. The event is visible in L1 as a higher energy region of time-frequency space just below 1600Hz. No such high-energy region is readily visible in H1. We also see similar noise in L1 at lower frequencies both before and after the time of the event, which adds credence to it being a glitch in L1 only. We also see that the ambient noise at the time of the run is in a normal state.

Frequency	τ	Half Sine-Gaussian		Ringdown	
Trigger	(s)	$h_{\text{rss}}^{50\%}$ ($\text{Hz}^{-1/2}$)	$E_{\text{GW}}^{50\%}$ (erg)	$h_{\text{rss}}^{50\%}$ ($\text{Hz}^{-1/2}$)	$E_{\text{GW}}^{50\%}$ (erg)
150 Hz	150	1.3×10^{-22}	1.3×10^{44}	1.4×10^{-22}	1.5×10^{44}
2674	400	1.4×10^{-22}	1.5×10^{44}	1.4×10^{-22}	1.6×10^{44}
750 Hz	150	2.0×10^{-22}	8.1×10^{45}	2.2×10^{-22}	9.6×10^{45}
2674	400	2.2×10^{-22}	9.9×10^{45}	2.4×10^{-22}	1.1×10^{46}
150 Hz	150	9.7×10^{-23}	2.6×10^{44}	1.0×10^{-22}	2.9×10^{44}
2656	400	1.0×10^{-22}	2.9×10^{44}	1.1×10^{-22}	3.3×10^{44}
750 Hz	150	1.4×10^{-22}	1.4×10^{46}	1.5×10^{-22}	1.7×10^{46}
2656	400	1.6×10^{-22}	1.7×10^{46}	1.7×10^{-22}	1.9×10^{46}

TABLE 13. Upper limits for h_{rss} and E_{GW} for both the half sine-Gaussian and ringdown waveforms at both 150 Hz and 750 Hz. We present the burst with the most sensitive upper limits from each source, which were trigger 2656 from SGR 1935+2154, and trigger 2674 from Swift J1818.0-1607. No long-duration analysis was run on the unknown source.

directional search and given that detection was unlikely since a sky position was unknown, we chose to save time by not running the analysis on the flares from the unknown source. All of the resulting FBS results are displayed in Table 5. No remarkably low FBS values were recorded for the long-duration search, with the smallest one being 2.2×10^{-2} .

We inject waveforms chosen to give us robust sensitivity in the frequency range of the quasi-periodic oscillations. These include half sine-Gaussians and ringdowns at frequencies 55 Hz, 150 Hz, 450 Hz, 750 Hz, and 1550 Hz. Each waveform is injected with time durations of 150 s and 450 s at each frequency. We standardize the sensitivity using the $h_{\text{rss}}^{50\%}$ of both waveforms injected at 150 Hz and 750 Hz. These sensitivities are presented in Table 13, where we present the upper limits for the most sensitive burst from each source.

In the O3 search we were most sensitive to trigger 2656 (from SGR 1935+2154), and its sensitivity is increased over the most constrained results of O2

by a factor of 1.2 to 2, depending on the waveform under consideration. While the detectors did indeed gain sensitivity for the O3 observing run, it is also important to note that with more magnetar flares to analyze (16 in O3 versus four in O2), there is a higher probability in O3 of having a flare occurring at a time and sky-location where the LIGO detectors have high antenna factors, indicating more optimal sensitivity in the direction of the flare. Graphical depictions of the gains in sensitivity over O2 are displayed in Figure 31.

We also note that the lowest energy upper limits are actually set by trigger 2674 from Swift J1818.0-1607, due to its closer proximity (the energy upper limit is proportional to $\frac{1}{\text{distance}^2}$). These upper limits, $E_{\text{GW}}^{50\%}$, are 1.3×10^{44} erg for the 150 s half sine-Gaussian at 150 Hz, and 8.1×10^{45} erg for the 150 s half sine-Gaussian at 750 Hz.

3.7 Sensitivity of the 2-component short-duration search

The 2-component structure of the short-duration search was a new element of the search implemented for O3. Including the delayed on-source search gives us sensitivity to short-duration signals in conjuncture with where the QPOs would be in the EM data, if the flares in O3 were giant flares. This same end could have been achieved with one long on-source window extending from $[-4, +500]$ s around the time of the flare, but we separated it into two separate searches so that we could maintain high sensitivity at the time of the flare, where most of the EM energy was emitted and a gravitational wave was most probable.

We now discuss the effectiveness of this double on-source window method at raising the sensitivity at the time of the flare. We measure the $h_{\text{rss}}^{50\%}$ of each waveform that is common to both searches (this just excludes the ringdowns), and

calculate a ratio of these sensitivities as measured in the centered search and in the delayed search:

$$\text{Ratio}_{\text{Sens}} = \frac{h_{\text{rss}}^{50\%}(\text{centered})}{h_{\text{rss}}^{50\%}(\text{delayed})}. \quad (3.18)$$

A histogram of these ratios including all waveform upper limits from all analyses that were common to both searches is shown in Figure 29. The median value of this ratio is .83, meaning that generally speaking the $h_{\text{rss}}^{50\%}$ of the centered search is 83% that of the delayed search. In Figure 30 we plot the most constrictive $h_{\text{rss}}^{50\%}$ for each waveform that was common to the centered and delayed searches, along with the sensitivity curves of each detector. In each case, the centered search was more sensitive. So this method did successfully raise the sensitivity of the search at the time of the flare.

We should also address the spread in Figure 29, because it is true there is a peak at the ratio .83, but that there are significant numbers of boxes and waveforms which have far different ratios. x-pipeline makes injections into the on-source window's data, and then records the value of $h_{\text{rss}}^{50\%}$ at which the injections are recovered with a greater significance than the loudest on-source event. When two distinct on-source windows are used for the same trigger, they will definitely have different events which set the threshold significance above which we consider an injection to be recovered. We also note that glitches of specific frequencies might change the pipeline cuts applied to one on-source window but not the other, changing the sensitivity as measured by each specific waveform.

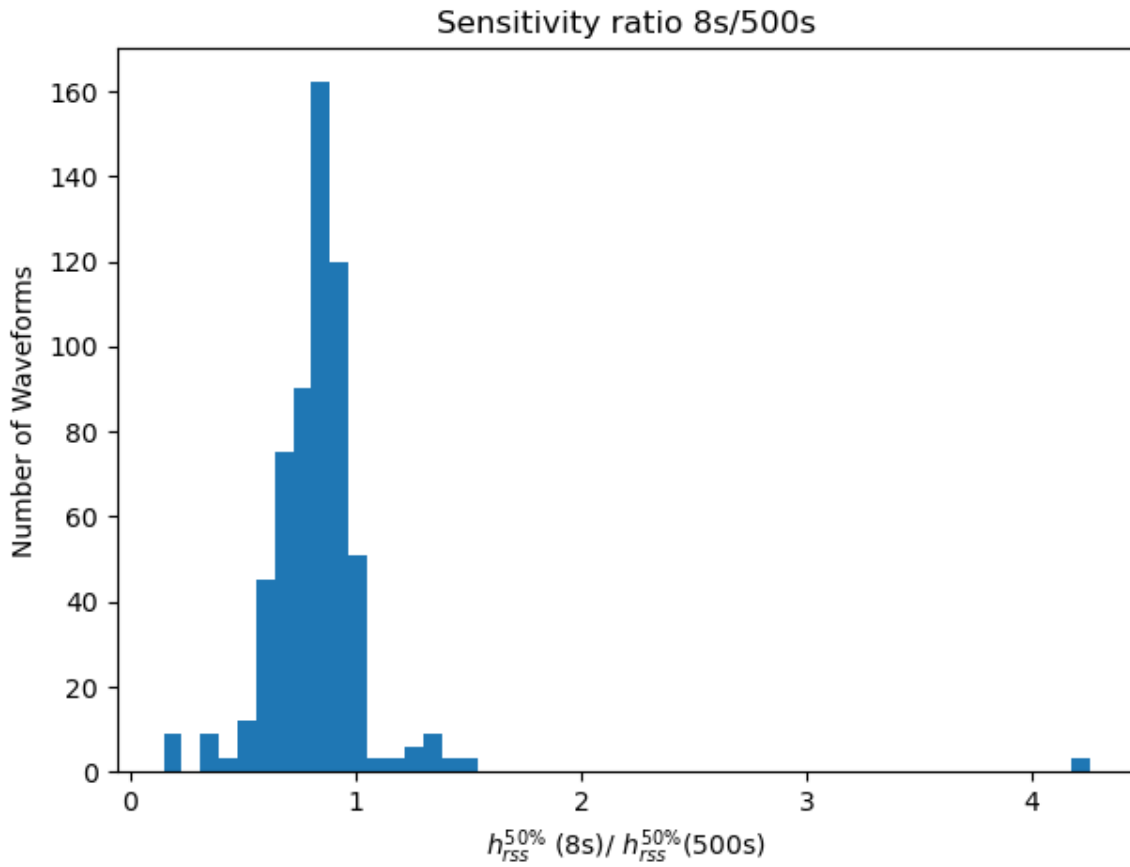


FIGURE 29. A histogram of the ratio of sensitivities between the centered and delayed searches, as measured by the $h_{RSS}^{50\%}$ for each waveform common to both searches injected into each trigger analyzed by both searches. The median $h_{RSS}^{50\%}$ for the centered search is found to be 83% of its counterpart in the delayed search.

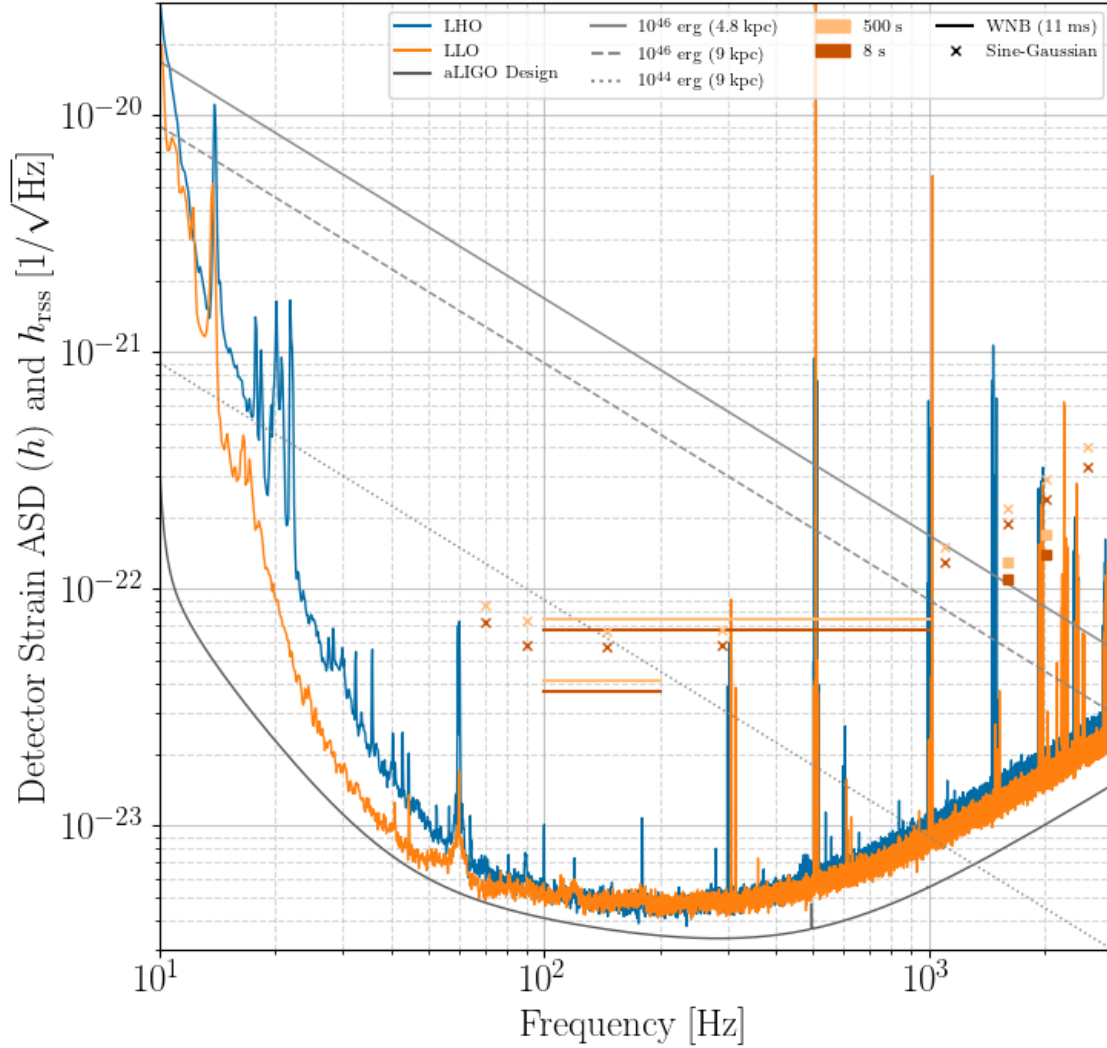


FIGURE 30. The best 50% detection $h_{\text{rss}}^{50\%}$ of each waveform (from either SGR 1935+2154 or J1818.0-1607) included in both the centered and delayed searches, overlaid with the O3 sensitivity curves from Hanford and Livingston. These include both circularly and elliptically polarized sine Gaussians, and White Noise Bursts (here we show the WNB's of 11 s duration). In every case we see that the centered on-source search has better sensitivity.

3.8 Conclusion

We search for gravitational-wave counterparts to 13 x-ray bursts of galactic magnetars SGR 1935+2154 and J1818.0-1607, as well as three EM bursts from an unknown source that are presumed to be magnetars. We use STAMP and x-pipeline to search for long and short duration gravitational wave signals respectively, and find no evidence of a gravitational-wave transient associated with any of these EM bursts. Our search spanned the parameter space most likely to contain the gravitational waves from f -modes, as well as long duration signals which could have been caused by Alfvén modes or torsional modes in the magnetar’s crust. The lowest p-value in our study which still corresponds to an event that has physically plausible parameters was 8.6×10^{-3} , but the probability of returning a p-value this low given the number of runs in the study is $\approx 29\%$. Hence, this result is statistically consistent with the null hypothesis.

We inject waveforms into the data to calculate the $h_{\text{rss}}^{50\%}$, above which 50% of the signals can be expected to be detected. For the short duration searches we inject sine-Gaussian chirplet waveforms ranging in frequency from 70 Hz to 3560 Hz, ringdowns between 1500 Hz and 2020 Hz, and white noise bursts ranging from 100 Hz to 1000 Hz. For the long duration search we inject ringdowns and half sine Gaussians at frequencies ranging from 55 Hz to 1550 Hz. We calculate the gravitational wave energy at 50% detection efficiency using Equation 3.7. For the short-duration search on bursts from known sources (SGR 1935+2154 and J1818.0-1607), this limit ranges from 1×10^{46} erg and 3×10^{47} erg, when considering the most sensitive analysis as measured by each of the waveforms with frequencies falling between 1500 Hz and 2020 Hz. We see a factor of improvement in sensitivity of 1.1 over the results of O2 when comparing the WNB waveforms,

which are the only waveforms which have exactly the same parameters. Comparing the circularly polarized waveforms near 1500 Hz and 2000 Hz, we see factors of sensitivity improvement of 1.5 and 1.7 respectively, which are shown in Figure 31.

The lowest $h_{\text{rss}}^{50\%}$ in the long-duration search is set by trigger 2656 from SGR 1935+2154, where $h_{\text{hrss}}^{50\%} = 8.7 \times 10^{-23} \text{ Hz}^{-\frac{1}{2}}$ for the 450 Hz ringdown WF, and the corresponding energy was $E_{\text{GW}}^{50\%} = 1.9 \times 10^{45} \text{ erg}$. Due to its closer proximity, the most constraining burst in terms of gravitational wave energy comes from trigger 2674 of J1818.0-1607, and is calculated to be $E_{\text{GW}}^{50\%} = 2.8 \times 10^{43} \text{ erg}$ at 55 Hz.

We also have EM energy data assuming isotropic emission for all of the bursts from SGR 1935+2154 except trigger 2654, and we use these to place constraints on the ratio of gravitational wave energy to EM energy, $\frac{E_{\text{GW}}^{50\%}}{E_{\text{EM}}^{\text{iso}}}$. For both the short-duration and long-duration searches the most constrained of these ratios is set by trigger 2656. For the short-duration search this ratio is $\frac{E_{\text{GW}}^{50\%}}{E_{\text{EM}}^{\text{iso}}} = 6.4 \times 10^6$ when considering the ringdown waveform at 1590 Hz and 100 ms duration. The long duration search sets this ratio to be $\frac{E_{\text{GW}}^{50\%}}{E_{\text{EM}}^{\text{iso}}} = 3.3 \times 10^3$, when considering the half sine-Gaussian waveform at 55 Hz with damping time of 150 s. While the upper limits on the gravitational wave strain energy are the best to date, the best upper limits on the gravitational wave to EM energy ratio were previously set in a study on the 2004 giant flare from SGR 1806-20, largely because its EM energy was so much higher.

The O4 observing run is set to begin in May, 2023, during which it is expected that LHO, LLO and VIRGO all reach higher sensitivities, and higher duty factors. The gravitational wave detector network will also be joined by KAGRA in O4, and even though KAGRA is not yet operating at high sensitivity, having more detectors in different regions of the world increases the probability of having

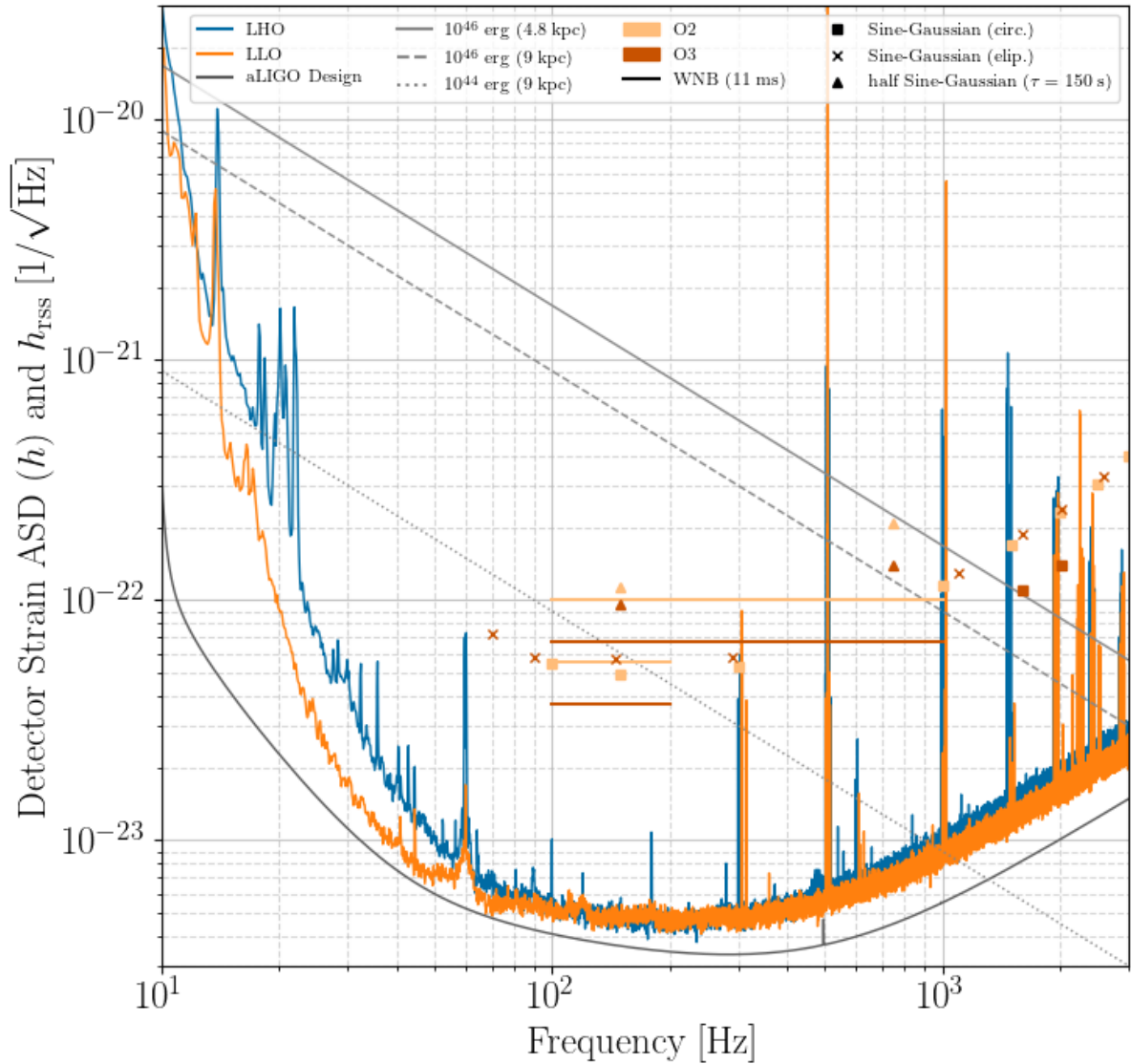


FIGURE 31. The 50% detection $h_{\text{rss}}^{50\%}$ of several waveforms from O3 with their corresponding waveforms from O2, overlaid with the O3 sensitivity curves from Hanford and Livingston. For each waveform we present the lowest $h_{\text{rss}}^{50\%}$ value coming from either SGR 1935+2154 or J1818.0-1607. The waveforms marked by 'x' represent elliptically polarized sine Gaussians, of which there were none injected in O2.

at least two detectors in the network with high antenna factors in the direction and at the time of a magnetar x-ray flare. The O4 paper plans also include plans for a stacked analysis over repeated EM triggers from the same source, a full discussion of which is available in Chapter V.

CHAPTER IV

O3 FAST RADIO BURST SEARCH

Abstract: Fast Radio Bursts, milliseconds-duration electromagnetic bursts in radio frequencies, happen far outside of Milky-Way galaxy and lack any conclusive progenitor theory. In this chapter we present the search for gravitational-waves coincident with FRBs during O3. We explore the current data and population of FRBs, introduce leading progenitor models, and present the minimally-modeled coherent searches over both repeating and non-repeating FRB. This study finds no evidence of a gravitational wave associated with any of the FRB triggers, but we detail several steps that were taken to optimize the sensitivity of the search. The upper limits on the root-sum-squared strain amplitude prove not to be physically relevant given the great distances to the sources, but this study serves as a proof of concept for future gravitational-wave searches over FRB sources.

4.1 Introduction to Fast Radio Bursts

FRBs are short, highly energetic radio pulses that last milliseconds in duration, and have properties that indicate sources far outside of Milky Way galaxy. They have become an increasingly scrutinized phenomenon within the astrophysics community since their first detection in 2007 [15], and even with the technological advancements of both electromagnetic and gravitational-wave observatories, the progenitors of FRBs remains an open mystery. A population of hundreds of FRBs have been detected since the initial one, and the corresponding progenitor theories have had to evolve in recent years to accommodate this population's properties. Progenitor models generally include gravitational-wave

emission, and the short durations of the radio sources imply a compact nature. We now discuss the history of FRB detections, and introduce the properties of these FRBs and their population.

The first detection of an FRB was found in the 1.4 GHz observation band in 2001 data from the Parkes telescope. This FRB was coined the ‘Lorimer burst’ after its discoverer [15], had an energy flux density of 30Jy and lasted for a duration of just under 5 ms. A Waterfall plot of the Lorimer burst is shown in Figure 32.

Light slows down by varying amounts based on its frequency as it passes through electron-rich environments, leading to a delayed time of arrival for the lower frequencies. We use this delay to calculate a Dispersion Measure (DM), which is the number of electrons that the light passes through en route to the detector, and use it to approximate the distance to the source of an FRB. The DM can be measured from the electromagnetic data as:

$$DM \propto \Delta t \left(\frac{1}{\nu_1^2} - \frac{1}{\nu_2^2} \right)^{-1} \quad (4.1)$$

where Δt is the difference in the arrival times of light of frequencies ν_1 and ν_2 [15].

This is just the number density of electrons integrated along the line of sight, broken up into three components representing source galaxy, the inter-galactic medium, and the Milky Way:

$$\begin{aligned} DM &= \int n_e dl \\ &= \int_{\text{source galaxy}} n_e dl + \int_{\text{inter-galactic medium}} n_e dl + \int_{\text{Milky Way}} n_e dl \end{aligned} \quad (4.2)$$

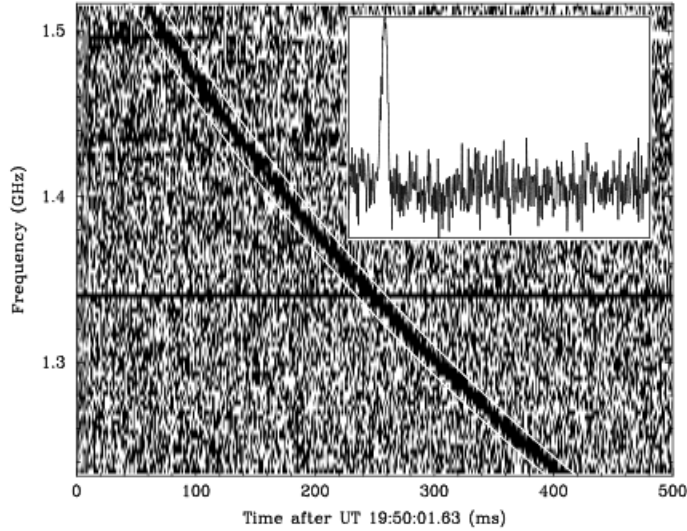


FIGURE 32. This is the waterfall plot of the Lorimer burst showing the difference in arrival times of photons of different frequencies in the first-discovered FRB [15].

We can use the NE2001 electron density model [102] to approximate the galactic contribution to the dispersion measure, and we can use population arguments to approximate the contribution of the host galaxy. We then attribute the unaccounted-for portion of the dispersion measure to the intergalactic medium, and assuming an electron density of three per cubic meter, we can calculate a distance to the source.

For the Lorimer burst, the DM was found to be 375 pc cm^{-3} , indicating that it originated far outside of our galaxy, and was also not associated with the Small Magellanic Cloud, which was angularly nearby. No other burst-like events were observed in a 90-hour observation span around the time of the Lorimer burst, and when the small field of view of the Parkes telescope ($\frac{1}{10^5}$ of the sky) is accounted for, it became apparent that FRBs would be much more prevalent in an all-sky survey, and could provide a useful tool for studying deep space phenomena.

The subsequent search for FRBs yielded 73 detections as of July, 2018 [103]. Nearly all of these were in the 1.3-1.5 GHz frequency range, which is the observation band of both the Parkes [104, 105] and ASKAP [106, 107] telescopes. Approximations of FRB event rates, when considering events with fluences greater than $10^{42} \frac{\text{erg}}{\text{s}}$ ranged from $3.5_{-2.4}^{+5.7} \times 10^4 \frac{1}{\text{Gpc}^3 \text{yr}}$ [108]. There was a sharp increase in the rate of FRB detections in 2018, when the Canadian Hydrogen Intensity Mapping Experiment (CHIME) radio telescope began its commissioning phase [109]. The CHIME detector consists of four 20m by 20m semi-cylindrical reflectors, and is sensitive to approximately 200°^2 of the sky at any given point in time, a huge improvement over previous observatories. Between July 25th, 2018 and March 28th, 2021, CHIME has publicly announced and released the data for 632 FRBs [103, 110], and of these most recent 100, 84 were identified as repeats of a previous FRB source. CHIME's sensitivity band is much broader than that of the previous detectors and somewhat lower, extending from 400 MHz to 800 MHz. Even though CHIME has a lower frequency range, many of the bursts it has detected were also detected by other detectors sensitive to higher frequencies, and so it is accepted that they come from the same population of FRBs.

A few interesting phenomena have surfaced in recent years amidst all of the FRBs that CHIME has detected. For nearly the first decade of observation, each FRB was detected as coming from a distinctly different sky location, indicating that they were all from different sources and that they could be caused by a transient, one-time event like a compact binary binary. But in 2016, FRB 121102 was observed to repeat 11 times [111] by the Arecibo telescope. This forced FRB emission theories to broaden enough to allow for FRBs to result from repeatable events. FRB 212201 opened the question of whether all FRBs repeat (and some

repeats have simply not been observed, or may have not happened yet), or whether two distinct classes exist: repeaters and non-repeaters.

In 2017, FRB 212201 was followed up through a joint observing effort by the Karl Jansky Very Large Array (VLA) and Arecibo, and better-localized to a star-forming region of a dwarf galaxy[112]. This environment is typically associated with long GRBs and supernovae. More follow-up observations were done on FRB 212201, and several instances of bursts were observed to be clustered over spans of several hours of time. These were also observed at much higher frequencies, up to 8 GHz [113, 114, 115]. As of 2020, the CHIME/FRB collaboration had detected 18 additional repeating FRBs [116, 117]. The sky locations and dispersion measures of these events were indistinguishable from the distributions of their non-repeating counterparts. However, their time durations do seem to be somewhat wider. A different emission mechanism could be responsible for this difference, and leads us to investigating the causes of the two classes of FRB as independent.

In 2020, CHIME announced the detection of the first periodically repeating source, FRB 180916 [118]. This source has a burst period of $16.35 \pm .18$ days, and CHIME has left open the possibility of high-frequency aliasing. In CHIME's limited exposure to FRB 180916, they detected 28 bursts between September of 2018 and October of 2019. The second periodic repeater was discovered shortly afterwards to have a 157 day period [119]. At this point it is necessary to have up to three emission models; one for non-repeaters, one for repeaters, and one for periodic repeaters. The model for periodic repeaters needs to be broad enough to accommodate periods spanning an entire order of magnitude and extending up to 157 days, a dubious feat for leading neutron star spin models.

To distinguish between repeaters and non-repeaters and try to close any open questions as to the overlap in their populations, 20 (supposedly) non-repeating FRBs were followed-up for 1,100 hours [107]. None of these FRBs were observed to repeat. The absence of repeats provides evidence that non-repeating FRBs really do exist as a separate class, given that repeating FRBs generally repeat several times an hour when they are active. Another possible distinction between the repeating and non-repeating FRBs is that of their host galaxies; it is more difficult to have a precise sky-localization of a non-repeating FRB, but a few have indeed been well-localized. In 2019, ASKAP localized FRB 180924 to a region 4 kpc from the center of a massive spiral galaxy with a very low rate of star formation[120], and FRB 190523 was localized to a region containing a galaxy at redshift $z = .66$ [121]. This host galaxy is about 100 times more massive than that housing the source of FRB 121102, and it's star formation rate is less than one hundredth that of FRB 121102's galaxy. It is entirely possible that non-repeating FRBs generally originate from older stellar populations.

There are still many open mysteries pertaining to the progenitors of these FRBs, with each competing model providing an adequate explanation for a subset of FRBs. The necessary condition to produce gravitational waves is the presence of a non-zero mass quadrupole moment, and those with high enough amplitudes might be detectable with ground-based detectors like Advanced LIGO and Virgo. Merger-based theories obviously produce the biggest mass quadrupole moment, so a search for gravitational waves is probably best suited for those coincident with non-repeating FRBs. The FRB theory catalogue [122] contains several models for both repeating and non-repeating FRBs that meet this necessary condition, and we discuss them here.

A persistent theory for the progenitors of repeating FRBs is an association with the x-ray flaring behavior of young, short-lived magnetars [123]. These magnetars have a magnetized nebula powered by the newly-formed magnetar’s spin-down. In these models, the FRB is described as being emission from the nebula in the supernova ejecta [124]. These theories were bolstered after FRB 121102 was localized to a galaxy with similar properties to those containing super-luminous supernovae, and emitting long GRBs. Under this model, the age of the magnetar responsible for FRB 121102 can be constrained to between 10s to 100s of years based on energy and dispersion measure arguments of the FRB. Even though this model might produce gravitational waves during the core-collapse of a supernova, no such gravitational waves have been detected, and especially not at the typical distances to FRBs. If this is indeed a correct model to explain a subset of FRB progenitors, then a search for gravitational waves from this population is not likely to provide further enlightenment.

There does exist an alternative formation channel of long-lasting, stable magnetars. Depending on the uncertainty in the maximum stable mass of a neutron star, M_{TOV} , it is approximated that up to 3% of BNS mergers could result in a stable magnetar [125]. From an experimental standpoint, this theory is appealing because it allows for magnetars to exist in older stellar populations, as well as FRBs. The host galaxy of FRB 180924 would fit this category in terms of star formation rate and stellar population age, and be much more apt for BNS mergers than the host galaxy of FRB 121102. Obviously the most detectable gravitational wave here would be produced when the two neutron stars merge, and while it is true that the LIGO collaboration has indeed detected BNS mergers [126],

given that less than 3% of these mergers result in a stable magnetar, it is unlikely that we will detect the gravitational waves from one's birth.

Since CHIME's periodicity observations, new repeated FRB emission theories have had to allow space for some FRBs to repeat from a periodically-occurring mechanism. A range of models have attributed it to the magnetar's rotational period [127], binary companions [128], and procession of the magnetar spin axis [129]. A binary companion with an orbital period of 16 days would produce gravitational waves of far lower frequency than the observation band of ground-based detectors, and would be a much better target of observation for future spaced-based observatories, specifically LISA.

The FRB emission theories for non-repeating FRBs include cataclysmic, one-off events that aren't repeated, but because most of them involve merger scenarios, they show much more potential as far as producing detectable gravitational waves. One appealing theory involves the merger between a primordial black hole (PBH), assuming they exist, and a neutron star [130]. The mass of the PBH in such a model falls in the range $10^{-16}M_s < M_{PBH} < 10^{-9}M_s$. The PBH enters the neutron star and loses kinetic energy due to both gravitational drag, and gravitational waves. As the PBH comes to rest at the core of the neutron star and accretes it, the neutron star collapses into a black hole of the same mass. The magnetosphere undergoes magnetic reconnection, and powers an FRB. A noteworthy element of this model is that it does not require the neutron star to have a strong magnetic field ($B \approx 10^{12}G$, less than that of a magnetar) in order to produce FRBs with the typical energy and time properties that have been observed. The amplitude of the gravitational waves produced by any merging system depends in part on the masses of the merging bodies, so when a PBH has a mass of $< 10^{-9}M_s$, the possibility

of detecting a resulting gravitational wave at the current sensitivities of Advanced LIGO and Advanced Virgo, is low.

Aside from any theories attributing FRBs to magnetars, the real smoking gun occurred on April 28th, 2020, when the first-ever (and still the only) FRB was detected from a galactic source by CHIME [33, 131] and STARE2 [132]. The sky-localization and dispersion measure indicate an origin consistent with the location of SGR 1935+2154, a well-known magnetar at a distance of ≈ 9 kpc which was actively flaring in the third observing run of Advanced LIGO and Virgo, and which we search for gravitational waves from in this thesis. The FRB came a day after a ‘flare forest’ of x-ray bursts from SGR 1935+2154 consisting of at least 35 discrete flares [133], and coincident with a hard x-ray flare [134]. This was the first signal in radio frequencies from SGR 1935+2154, and although it remained actively flaring for several days following the burst forest and FRB, no more FRBs were detected from it.

The galactic FRB had a two-component structure, each component being a few ms wide, and separated by about 30 ms. It is common for repeating FRBs to have multiple components, but the frequency of these components generally decreases in time [116, 117, 135]. The galactic FRB rose in frequency, with most of the first pulse being detected between 400-600 MHz and the second pulse being detected between 600-800 MHz. This is not the first repeating FRB with an increasing frequency substructures, but it does beg the question of whether or not this is a typical FRB.

Gravitational waves would be produced in the event of an FRB exciting non-radial modes of oscillation in a magnetar’s core, and also in the event of a merger scenario. The only previous gravitational wave follow-up study on FRBs

is one which was conducted on 6 such events detected by Parkes in between 2007 and 2013 [136]. The search spanned two minutes before and after each FRB, and used x-pipeline to search data from LIGO, GEO [137] and initial Virgo [138]. No evidence of a gravitational wave was found in association with any of the FRBs in the study, and the sensitivity of the detectors was so low that the strain and energy upper limits lacked astrophysical relevance. The study did however provide a framework for future multi-messenger gravitational wave follow-up studies.

In this chapter we report on the gravitational wave follow-up search to the FRB detections made by CHIME during O3a, which extended from April 1st, 2019 to September 30th, 2019 [16]. This was a two-part search, including searches with PyGRB, a pipeline specifically used to target signals from binary inspiral mergers. We also use x-pipeline to provide sensitivity to minimally modeled signals. In this chapter we neglect to discuss the methods and results of the PyGRB component of the search, because I was very minimally involved. The remainder of this chapter is organized as follows: we first introduce the data and the triggers provided by CHIME during O3a. We then discuss the search methods, including the searches run on both repeaters and non-repeaters. We then present the results of the search, and estimates of the search's sensitivity.

4.2 The FRB Sample

As part of a memorandum of understanding between CHIME and the LIGO-Virgo-KAGRA (LVK) collaboration, CHIME provided burst details for 806 FRBs in the date range of O3, 338 of which happened during O3a, 168 of which are published in the first CHIME event catalog [139]. CHIME provided a detection time, total DM, and sky location information for each FRB in the sample. We use

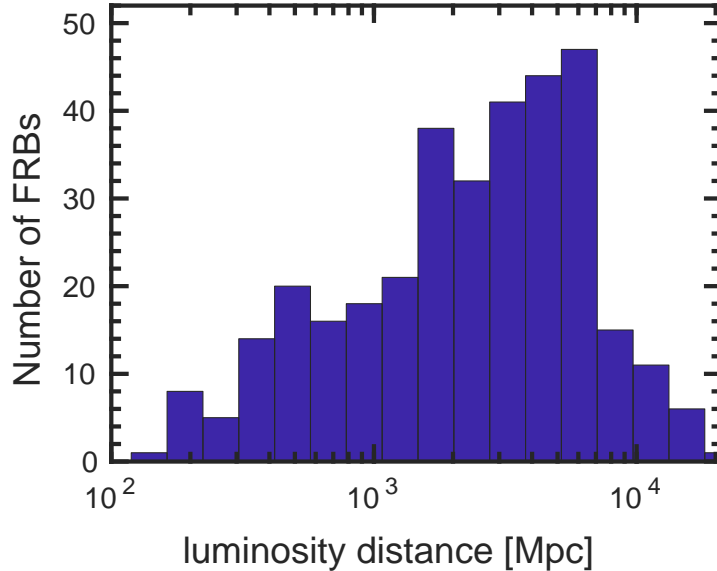


FIGURE 33. A histogram of the posterior luminosity distance values of each FRB in the CHIME FRB sample of 806 bursts [16]. Each of these luminosity distances has a very high uncertainty with the 90% credible interval commonly spanning hundreds of Mpc, making it difficult to prioritize which events to analyse. It should be noted that a very low percentage of these fall within the aLIGO detection range; the closest FRB in the sample is FRB 20190425A, for which the median distance is 133 Mpc, with a 90% confidence interval ranging from 13 Mpc to 386 Mpc.

this to approximate the luminosity distance of each of the sources in our sample, a histogram of which is shown in Figure 33.

These distance approximations indicate a large number of FRBs detected from greater distances, which is sensible given that the sky volume increases as the distance³. It is also important to note the high percentage of these bursts that fall at distances greater than ≈ 1000 Mpc, and compare that to the current binary inspiral range of the detectors, most notably ≈ 115 Mpc and ≈ 140 Mpc for LHO and LLO respectively.

A further complication arises in considering the form of the sky localizations given by CHIME, which consist of a series of possible values of the right ascension

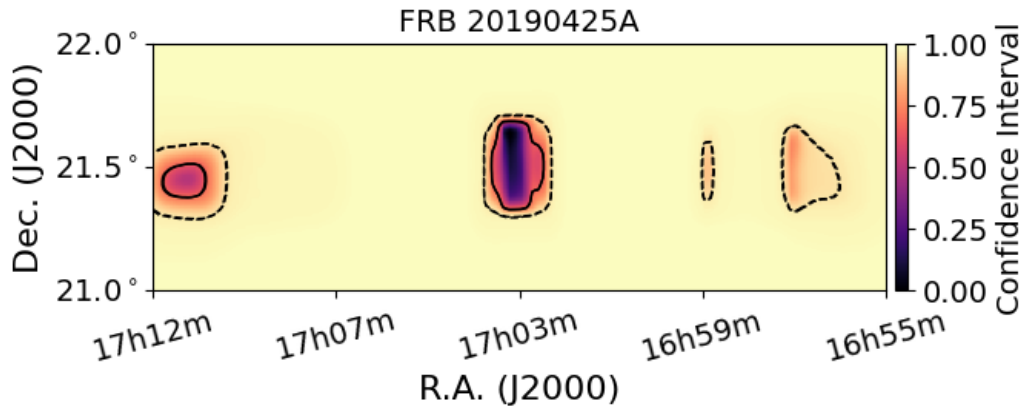


FIGURE 34. An example output of the localization data provided by CHIME, including each of the sky localization islands [16].

(RA), accompanied by the 95% confidence interval contours of each one. The end result is a series of dis-connected ‘islands’, each of which could be the true sky-location of the burst. An example CHIME sky-localization map is given in Figure 34.

The necessary conditions for a gravitational-wave search to be conducted on a given FRB is that at least two detectors are in observation mode for at least 90% of the on-source time window, and that the data quality be of a reasonable level during that time. The search is limited by both person-power and computational resources, and so FRB triggers were prioritized based primarily on detector network, and then secondly on luminosity distance. We terminated our search efforts when the distance to the sources under consideration started to become ridiculously high in comparison to the observational sensitivity of the aLIGO facilities. We ran on a total of 11 repeated FRBs from the nearest three sources, which were FRB 20180916B (seven repeats), FRB 20180814A (two repeats), and FRB 20180814A (two repeats). The details of the repeated bursts are given in Table 14. We also ran the minimally modeled search on 29 non-repeating FRBs.

FRB Name	UTC Time [s]	R.A.	Dec.	DM	D_L -Low [pc cm ⁻³]	D_L -high [Mpc]
FRB20190817A	14:39:52	4 ^h 21 ^m 08 ^s	73°47'	189.5	19.5	539.2
FRB20190929C	11:58:29	4 ^h 22 ^m 25 ^s	73°40'	191.6	20.8	550.1
FRB20190518A	18:13:33	1 ^h 58 ^m 14 ^s	65°46'	350.5	148.1	149.9
FRB20190518E	18:20:57	1 ^h 57 ^m 50 ^s	65°43'	350.0	148.1	149.9
FRB20190519A	17:50:16	1 ^h 43 ^m 44 ^s	65°48'	350.0	148.1	149.9
FRB20190519C	18:10:41	1 ^h 58 ^m 00 ^s	65°47'	348.8	148.1	149.9
FRB20190809A	12:50:40	1 ^h 58 ^m 16 ^s	65°43'	356.2	148.1	149.9
FRB20190825A	11:48:18	1 ^h 58 ^m 07 ^s	65°42'	349.6	148.1	149.9
FRB20190825B	11:51:54	1 ^h 58 ^m 04 ^s	65°23'	349.9	148.1	149.9
FRB20190421A	08:00:04	13 ^h 51 ^m 57 ^s	48°10'	225.9	125.1	1260.8
FRB20190702B	03:14:36	13 ^h 52 ^m 25 ^s	48°15'	224.4	125.8	1257.5

TABLE 14. Details of the 11 repeating FRBs events provided by CHIME[16]. Repeaters are determined by the CHIME events with the same sky positions and DM. The detector network indicates the detectors that were in observing at the time of the FRB; V1 = Virgo, H1 = Hanford, and L1 = Livingston. For FRB 20190518A and its associated repeats, we list only the distance of the source as obtained by galaxy localization [20]. There are no islands of sky position on these events by virtue of being repeated events from the same source.

4.3 Methods

Although there are multiple different progenitor theories for both repeating and non-repeating FRBs, the range of progenitor theories for non-repeating FRBs is somewhat less constrained because it includes binary merger scenarios. We design the gravitational wave search to be minimally modeled so as not to assume physics that we lack evidence for, and to have a basic minimum of sensitivity to gravitational waves across a broad range of parameter space. We use x-pipeline for this minimally modeled coherent search [51] on both the repeating and non-repeating FRBs. A more complete description of x-pipeline is available in Chapters 3.3 and 5.2.

In an effort to make the x-pipeline search of non-repeating sources both computationally efficient and have robust sensitivity to many different signal parameters, we search in the frequency range of 32 Hz to 2000 Hz, with an on-source window extending from [-600 s, 120 s] around the time of the FRB to allow for a broad range of time offsets between the FRB and the gravitational wave. Injected waveforms included elliptically polarized sine Gaussians (given by Equation 3.9) with central frequencies at 70 Hz, 90 Hz, 145 Hz, 290 Hz, 650 Hz, 1100 Hz, and 1995 Hz, with damping times $\tau = \frac{1}{f}$. We also included ringdown waveforms at central frequency 1500 Hz with envelope times of 100 ms and 200 ms, and the same WNB waveforms as used in the magnetar search. We also include a series of Accretion Disk Instability (ADI) waveforms, a BNS and a neutron star black hole (NSBH) waveform.

The islands in the sky-position estimates are dealt with by generating circular sky-position grids over each island with radii that cover the uncertainty of the island. Each of these circles is populated with evenly spaced points, and for each

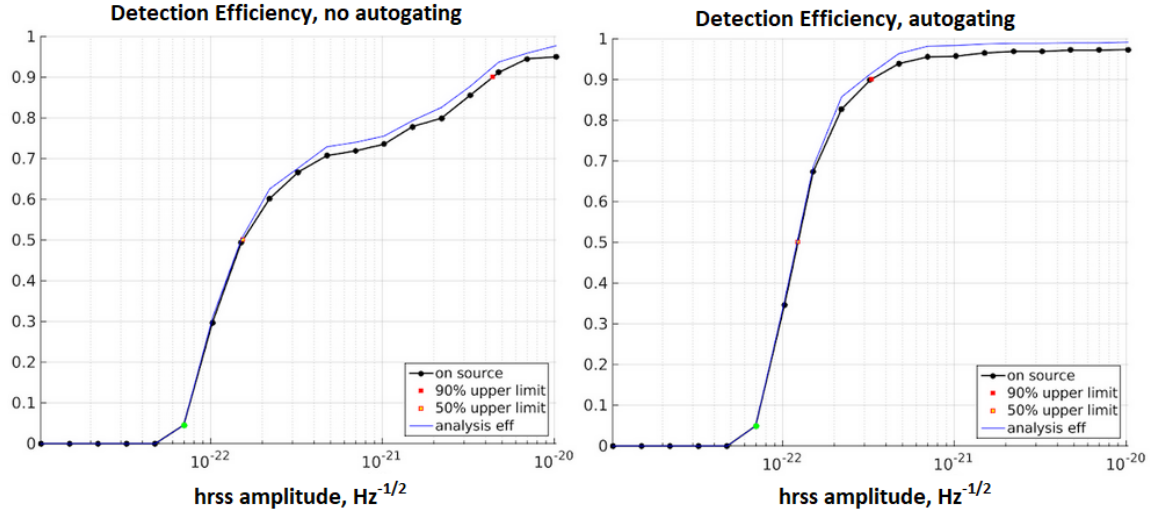


FIGURE 35. The detection efficiency curves of one of the ADI waveforms injected into FRB 37888771. The plot on the left is without autogating, and the plot on the right is with autogating. The ADI waveform is a long-duration waveform, and one which normally has sensitivity limitations due to short-duration transients. We see that when autogating is applied the efficiency curve is smoother and approaches unity faster, and we also see that it has lower values of h_{RSS}^{50} and h_{RSS}^{90} , meaning it has higher sensitivity as measured by this ADI waveform.

of these points a coherent data stream is generated with appropriate time offsets.

Each of these data streams was then searched.

One relevant upgrade to x-pipeline between O2 and O3 was the development of an autogating [94] algorithm, which constitutes an additional method of suppressing incoherent noise in the analysis. Autogating increases the sensitivity of the longer duration signals, which has previously been limited by short-duration noise transients, by applying a gate over the whitened data in an individual detector if the average energy in a 1 s span of time exceeds a specific threshold in that detector only. Figure 35 shows the improvement in the sensitivity curves of one of the ADI waveforms before and after autogating is applied. Autogating is only sometimes beneficial to the analysis, and is only sometimes used in the analyses over non-repeating FRBs.

Given that the leading models for repeating FRBs include active magnetars as their source, we structure the search for gravitational waves associated with repeating FRBs very similarly to the centered on-source component of the magnetar search, which is detailed in Chapter 3.3. We use an 8 s on-source window centered at the time of the FRB, a 3 hour background time taken symmetrically about the FRB time, and a block time of 64 s. The frequency range of the search is from 50 Hz to 4000 Hz, which is notably higher than that of the search over non-repeaters to give sensitivity in the f -mode frequency range.

Injected waveforms include a series of elliptically polarized sine-Gaussian chirplets at frequencies 70 Hz, 90 Hz, 145 Hz, 290 Hz, 1100 Hz, 1600 Hz, 1995 Hz, 2600 Hz, and 3560 Hz, and circularly polarized sine Gaussians at 1600 Hz and 1995 Hz. With the exception of the WNBs, these are all short-duration waveforms. It is important to note that under the magnetar hypothesis, there is no need for long duration waveforms such as the ADIs during an 8 s on-source search centered over the time of the FRB. Any long duration gravitational waves which could be produced would be in the hundreds of seconds after the FRB, and we neglect to search in that region of parameter space with a long-duration, but computationally expensive pipeline such as STAMP.

The sensitivity curves of short-duration waveforms do not normally benefit from autogating because they have a higher probability of being gated by the autogating algorithm, effectively lowering the detection efficiency. Example efficiency curves showing this effect are shown in Figure 36. We therefore run all of the analyses over the repeating FRBs without autogating, and use a higher minimum frequency of analysis to mitigate low-frequency glitches.

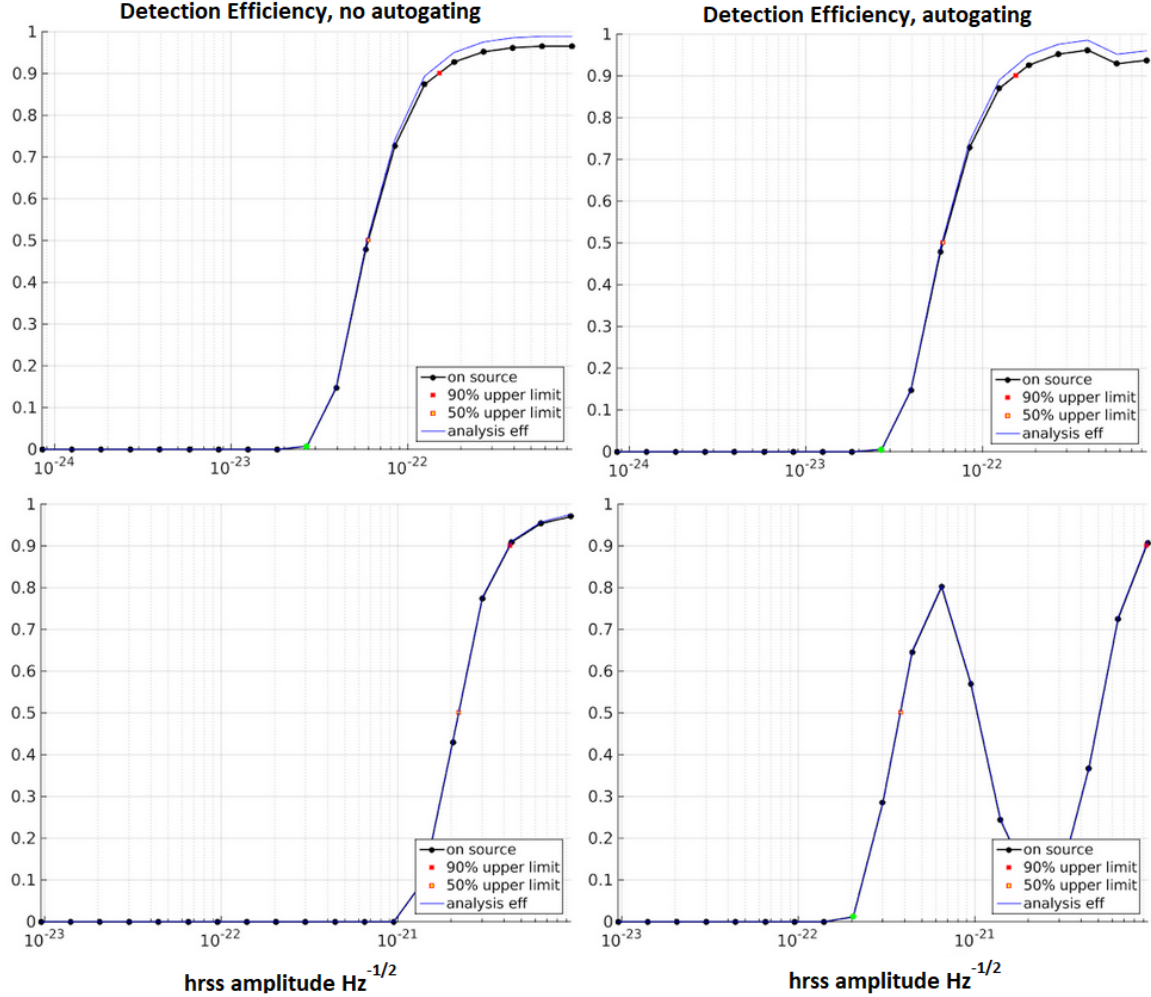


FIGURE 36. The detection efficiency curves of the elliptically polarized sine Gaussian waveforms at 650 Hz. The top row is injected into FRB 37888771 and the bottom row is FRB 39069820. The left side plots are with no autogating, and the right side plots are with autogating applied. We see that at higher values of the h_{rSS} injection amplitude there is a drop in the fraction of injections recovered in the autogated analyses. This is because the injections are loud enough such that the average energy over the 1 s span of time exceeds the autogating threshold in 1 detector but not in the other, and the injection is gated. The detection efficiency normally rises at even higher amplitudes because the autogating algorithm canceled if the energy requirement is met in multiple detectors.

4.4 Results

Neither the searches over repeating FRBs or non-repeating FRBs returned any p-values low enough to be considered interesting. The lowest one in the search over non-repeaters was 1.9×10^{-2} , and when we take into account that 32 analyses were run on non-repeaters, the probability of obtaining at least one p-value at this level is $\approx 54\%$. The lowest p-value for the analyses over the repeaters was 1.3×10^{-1} . The cumulative probability of each p-value in both the searches over non-repeaters and repeaters is found in Figure 37.

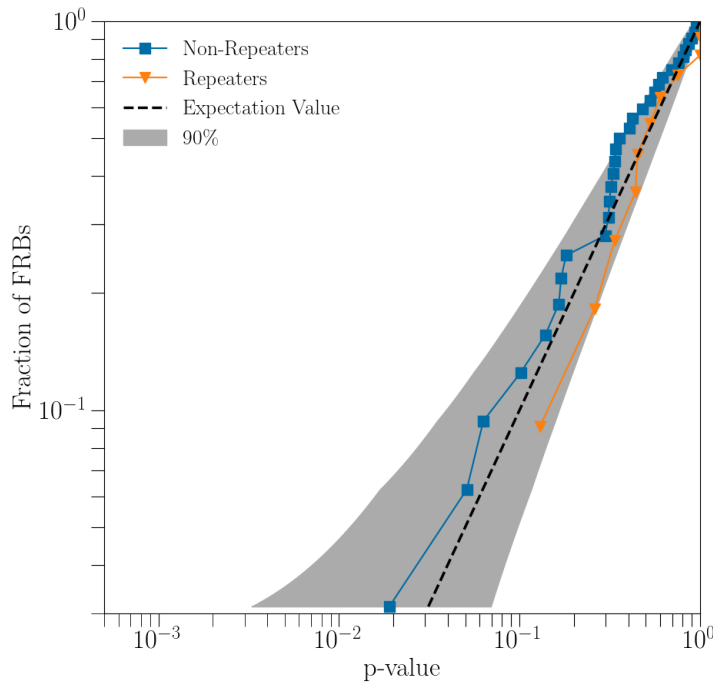


FIGURE 37. The cumulative distribution of the p-values from all the analyses over both repeating FRBs and non-repeaters. We include the 90% band encompassing the range in which each p-value has a 90% chance of falling, numerically calculated [16]. There are two repeaters with p-values of 1; this indicates that no on-source events survived the pipeline cuts.

As in the case of the O3 magnetar search, we standardize the sensitivity of the search by the threshold root-sum-square of the integrated gravitational-wave strain with 50% injection recovery efficiency ($h_{\text{rss}}^{50\%}$) and corresponding gravitational-wave injection energy with 50% recovery efficiency ($E_{\text{GW}}^{50\%}$). Median values for the $h_{\text{rss}}^{50\%}$ of an elliptically polarized sine-Gaussian at 1600 Hz for non-repeaters is $2.0 \times 10^{-22} \text{ Hz}^{-\frac{1}{2}}$, and for repeaters this is $1.4 \times 10^{-22} \text{ Hz}^{-\frac{1}{2}}$. There are two plausible reasons for the increased sensitivity of the search on repeaters as measured by the 1600 Hz sine-Gaussian chirplet; the first is that x-pipeline weights the importance of all waveforms equally when making cuts to optimize their sensitivity. Since the search on repeaters included fewer low-frequency and longer-duration waveforms, the emphasis was placed more heavily on the waveforms which more closely resembled the astrophysical models of an f -mode. The second reason being that the short-duration waveforms such as the sine-Gaussian series were systematically reduced in sensitivity by the autogating procedure often used in the non-repeater case. In Figure 38 we give histograms of the values of $h_{\text{rss}}^{50\%}$ of the 1600 Hz sine-Gaussian chirplet with elliptical polarization for both the search on repeating and non-repeating FRBs.

As in the case of the O3 magnetar search, the $E_{\text{GW}}^{50\%}$ is calculated for the sine Gaussians using the narrow-band approximation given by Equation 3.7, and for the white noise bursts using Equation 3.8. It should be noted that the gravitational-wave energy is proportional to the distance² to the source, and since we have such poorly-constrained measures of the luminosity distance to these sources, the limits on the gravitational-wave energy are even less accurate. However, even if we assume the most optimistic possible values of the luminosity distance, we still calculate values of $E_{\text{GW}}^{50\%}$ that are sizable percentages of a neutron star's mass, and

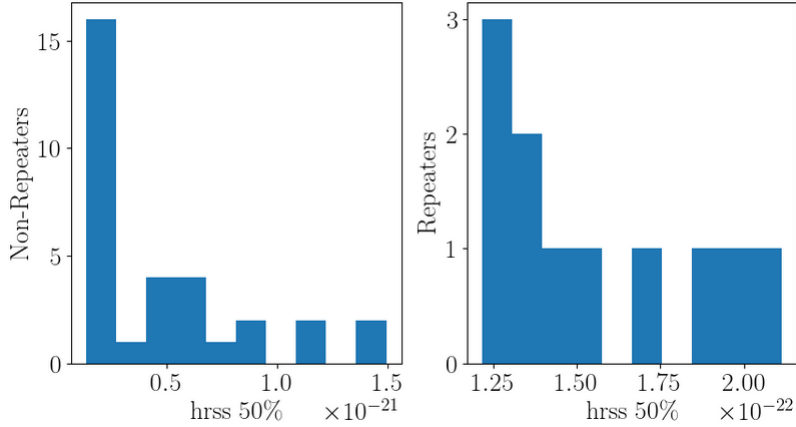


FIGURE 38. Histograms showing the $h_{\text{rss}}^{50\%}$ of the 1600 Hz elliptically polarized sine Gaussian waveform for both the non-repeaters (left) and the repeaters (right). The search over repeaters generally has lower values of $h_{\text{rss}}^{50\%}$, and so is a more sensitive search as measured by this waveform.

in many cases many times greater than a neutron-star mass. This energy threshold of $E_{\text{GW}}^{50\%}$ is obviously non-physical for the case of repeating FRBs by virtue of the magnetar still having to exist to repeat again.

4.5 Conclusion

We used x-pipeline to search for short-duration (ms to s) gravitational waves of non-specified signal morphology associated with FRBs during double detector time of O3. This search included 11 FRBs from repeating sources, and 32 FRBs which are non-repeating.

We searched for signals within an 8 s window centered at the time of each repeated FRB, and in a window $[-60, +600]$ s around each non-repeating FRB. No evidence was found for any of the searches that might indicate an associated gravitational wave. We standardize the sensitivity of the searches by constraining the value of $h_{\text{rss}}^{50\%}$. For the repeaters the median $h_{\text{rss}}^{50\%}$ was $1.4 \times 10^{-22} \text{ Hz}^{-\frac{1}{2}}$, and for the non-repeaters this was $2.0 \times 10^{-22} \text{ Hz}^{-\frac{1}{2}}$.

Associated energy thresholds, $E_{\text{GW}}^{50\%}$, contain an inherently high amount of uncertainty due to the poorly constrained luminosity distances to the FRB sources. Even when calculated using the most optimistic distance values, the energy thresholds are approximately equal to the binding energy of neutron stars. For repeaters, this makes them non-physical. For non-repeaters, the only physically plausible mechanism would be a binary merger with such a high energy budget that multiple solar masses worth of energy can be lost to gravitational waves.

A more sensitive search is needed in order for gravitational waves to advance any progenitor theories of FRBs. The O4 observing run is scheduled to begin in May of 2023, and the current LIGO and Virgo detectors are expected to reach higher sensitivity. The detector network will also be joined by the Kamioka Gravitational Wave Detector (KAGRA) in O4. While KAGRA is not at design sensitivity, its sensitivity will increase throughout the run and having it online will increase the probability of having detectors available with high antenna factors at the time of any given FRB.

There are also plans for the O4 papers to include a stacked analysis over repeated burst sources, specifically from FRBs and magnetar x-ray flares. Past studies have indicated that stacking can yield improvements in sensitivity of $N^{\frac{1}{4}}$, where N is the number of bursts [80], and preliminary studies on the significance of x-pipeline events seem consistent with this estimate, however the effects of stacking on the $h_{\text{rss}}^{50\%}$ remains an open question. More details on stacking are given in Chapter V. The highest number of repeats included in our study is seven, coming from the source of FRB 20190518A. Stacking could provide lower $h_{\text{rss}}^{50\%}$ values especially if we get a high number of repeats from a source at a lower distance.

CHAPTER V

A SEARCH FOR REPEATED, LOW-SNR TRANSIENTS

Abstract: The burst analysis plans for O4 include a ‘stacked’ analysis, where the gravitational-wave strain data from multiple externally triggered events is combined and then subjected to a search for gravitational waves. Here we present the methods of doing the stacking by introducing a new branch of x-pipeline, an existing LIGO burst search pipeline. We define a p-value, and discuss how its minimum possible value depends on the x-pipeline search parameters, but for the standard input parameters this minimum p-value is 1.47×10^{-7} . We perform the stacking process on stacks varying in size up to 17 triggers, and demonstrate that the mean detection statistic (S) in an unstacked analysis that is needed to detect a stacked event with a p-value of 5×10^{-4} drops from 12.9 (one trigger) to 4.9 (17 triggers), and is approximated by $S = 1.78 + 11.32 \times N^{-0.46}$. Injecting a 100 ms ringdown waveform at 1590 Hz into the unstacked analyses and running the normal x-pipeline post-processing shows that the root-sum-squared injection amplitude needed to make a detection (in the stacked case) is reduced by 25% with 5 triggers in the stack. We show that this stacking method becomes obsolete with greater than 93 triggers in the stack, and study minor changes to the input parameters which can increase this number. We also introduce a weighting scheme, and shown that it yields similar increases in sensitivity as more triggers are stacked.

5.1 Introduction to and history of stacked searches

In Chapter III we have presented and discussed the search for gravitational waves associated with the x-ray flares of magnetars during O3. We found no

evidence for any such candidates, but we placed limits on the value of $h_{\text{rss}}^{50\%}$ for which we would expect to detect a gravitational wave with 50% probability if one were present. One noteworthy feature of this study is the high number of p-values that fall just outside of the band in which one would expect to find 90% of the p-values if they were uniformly distributed, shown in Figure 26. Three of the 14 triggers analyzed in the centered search had p-values falling outside of this 90% band, with two more just inside of it. While these numbers are not extreme enough to provide surprise, they should inspire us to develop a mechanism of analyzing multiple bursting events simultaneously, in the hopes of raising our sensitivity to signals consistently associated with a magnetar flare, and with consistent properties. For the rest of this dissertation we will refer to the simultaneous analysis of multiple triggers as ‘stacking’.

The first pipeline specially used for stacking magnetar flares was called Stack-a-flare [80], which was an extension of a previously used excess power search pipeline called Flare Pipeline, used in the first LIGO searches for gravitational waves associated with flaring magnetars [140]. Stack-a-flare included two discrete algorithms by which gravitational-wave strain data could be stacked: Time stacking (T-stacking) and Power stacking (P-stacking). T-stacking would combine the time-series data at the time of each flare, and perform discrete Fourier transforms to make a time-frequency map for each detector. These maps were then combined into one and compared to the background. The P-stacking algorithm did the Fourier transform on each event individually, and then stacked the time-frequency maps of each flare. The SNR ratio in the T-stack scenario was found to go as $N^{\frac{1}{2}}$ where N is the number of triggers in the stack, while the P-stacking SNR went as $N^{\frac{1}{4}}$, the difference arising from the noise being Gaussian in the T-stacking case, and

gamma-distributed in the P-stacking case. The T-stacking case, however, allows very little room for uncertainty in the arrival time of the gravitational wave, making P-stacking the obvious choice.

A first stacked search was performed on the flare storm of SGR 1900+14 in 2006, treating the points in the light curve with the sharpest rise times as discrete flares [141]. When 11 of these flares were stacked the $h_{\text{rss}}^{90\%}$ at 90% detection efficiency for a Ringdown waveform at 1590 Hz, and 200 ms damping time was found to be $7.4 \times 10^{-22} \text{Hz}^{-\frac{1}{2}}$. For a stack of 18 flares weighted by their fluence, this number was $1.3 \times 10^{-21} \text{Hz}^{-\frac{1}{2}}$.

5.2 Description of x-pipeline

x-pipeline [51, 52] is a coherent GW search pipeline used for minimally modeled, targeted searches on bursts with a known time and sky location. Whitened strain data is converted into time-frequency maps with the brightness of each pixel reflecting the SNR of that pixel. Neighboring pixels are then combined into clusters, the SNRs of which are the sum of the SNRs of the constituent pixels. Each cluster in the on-source is a potential gravitational wave event, and is assigned a p-value. Injections are then made into the on-source data to determine the amplitude of injection which is detected with greater significance than the most significant on-source event. x-pipeline has been used historically to search for short-duration gravitational wave transients from electromagnetic burst sources, most notably in LIGO’s GRB searches [94, 94], and as discussed in Chapters 3.3 and 4.3, it was also used to search for GWs in the O3 magnetar search [14] and the O3a FRB search [16].

We now discuss the specific search methods employed by x-pipeline which make it adaptable to a stacked search. The x-pipeline targeted search algorithm can be broken up into two stages, the first stage of which determines a list of non-Gaussian transients in the background. It records the time, frequency, energy, and significance statistics of these transients. The post-processing stage then assigns one segment in the background to be a stand-in on-source for optimization (called a *dummy on-source*). Waveforms are then injected into the dummy on-source data, and the algorithm records $h_{\text{rss}}^{50\%}$. Cuts on the energy measures are then made to optimize the $h_{\text{rss}}^{50\%}$, and then a p-value is calculated for each surviving event in the dummy on-source. This p-value is calculated to be:

$$P = \frac{\text{Number of background events louder than loudest on-source event}}{\text{Number of total background events}} \quad (5.1)$$

This process can be repeated as many times as the analyst wishes with different input analysis parameters, and when the results are optimized, the same cuts and injections are used on the on-source data to calculate an actual p-value, and the $h_{\text{rss}}^{50\%}$ sensitivity limits.

Historically in most searches [14, 16, 82, 93, 94], the background in x-pipeline is taken to be 10800 s in duration. This number is somewhat arbitrary; the advantage to making it large is that it allows more background events and can yield a more precise p-value and cuts. But it also makes the assumption that the strain data and detector characteristics are reasonably homogeneous throughout the duration of the background – or at least that the data at any given time in the background are representative of the on-source data. This is not always a good assumption given that the BNS inspiral range is always changing, but we validate

it by choosing our background time range to be symmetric about the time of the burst.

The background is handled in the first stage of the x-pipeline algorithm by being broken into segments of time (*blocks*) determined by the *blocktime*, which is a standard input in the parameters file. x-pipeline necessarily receives blocktime lengths which are a power of 2, the lowest possible one being 64 s. Sixteen seconds are then removed from the beginning and end of each blocktime to be used to whiten the data. It is assumed that whitening the data in this way will remove stationary noise and ensure that the brightest 1% of pixels will be distributed independently of frequency in the absence of any non-Gaussianity. This leaves

$$2^n - 32 \tag{5.2}$$

seconds of usable data in each block in which to search for background events.

We can effectively create more blocks of time to expand the background by time-sliding the data from one (or two in the case of a three-detector network) detectors. We perform two different types of time-slides, the first is called *time lags*. The goal of performing time lags is to match each block of data from one detector with a different block of data from the other detector(s). A time lag translates the start and ending times of each block of data from a detector by a fixed amount (an integer multiple of the usable time), and then combines it with the data from the first detector at the new time, which has not been translated. In the case of a three detector network, the data from the 3rd detector is translated by the same amount and in the opposite direction. This effectively creates new blocks of time for the background, to which the contributions from each detector come from independent times.

The total number of blocks in the background is just a combinatorics problem. Let B denote the number of blocks of unslid data in one detector. Since time-sliding one detector means aligning each block from the slid detector with one from the unslid detector, the total number of blocks in the background of a two detector network is then B^2 . Counting the number of blocks in the background when including the time lags from the 3rd detector is more complicated because after each time lag is performed, an additional two blocks in the unslid detector no longer have two corresponding blocks in the slid detector. We can also only perform $\frac{B}{2}$ time lags in each direction before the three-detector time overlap becomes null. Then the number of blocks after the time lags in the three-detector case is:

$$\begin{aligned}
 B_{tot} &= B + \sum_{i=1}^{\frac{B}{2}} B - 2i \\
 &= \frac{B}{2}
 \end{aligned}
 \tag{5.3}$$

where i indicates the time lag number, and the first B represents the $i = 0$ case of the unslid data. Effectively this means that including a 3rd detector in the network cuts the size of the background in half.

The second type of time-slide is the circular time slide, in which the timeseries data within each time-lagged block is translated by multiples of a given amount of time. In a standard x-pipeline run, where the maximum size of the time-pixel is 2 s with 50% overlap, the minimum time translation which can be preformed without data appearing within the limits of multiple Fast Fourier Transforms (FFTs) to create the pixels is 3 s. Preforming the circular time slides consists of translating the data from the second detector in the network forward in time by integer multiples of 3 s and commuting the section of the timeseries

that protrudes off of the end of that of the first detector’s timeseries to the start of the timeseries for full alignment with the first detector. Then the FFTs are done. In the case of a three-detector network the third timeseries is translated in the opposite direction. Each circular time slide is assumed to produce an independent block of time to be included in the background. So this method then expands the background by a factor of:

$$\frac{\text{blocktime} - 32}{\text{circular time slide length}}. \tag{5.4}$$

FFTs are then done on each block of timeseries data in the background. The FFT lengths are $\frac{1}{2^n}$ with 50% overlap, and in the standard x-pipeline runs, $-1 \leq n \leq 7$. The FFT leaves a time-frequency map displaying the energy contained in each pixel. x-pipeline assigns an SNR to each pixel, and makes note of the pixels whose SNR falls above a given percentage (the brightness percentage) threshold set by the analyst. In the standard x-pipeline runs this is set at 1%. Neighboring pixels are combined into ‘clusters’ whose SNR’s are the linear combination of that of their constituent pixels. Each of these clusters in the on-source is taken to be a potential gravitational wave, and it is assumed that each of the clusters in the background is an instrumental noise artifact.

Along with time and frequency information, x-pipeline calculates and stores several measures of the energy for each of these clusters. x-pipeline projects the strain data onto a basis defined by the detector response functions, and an orthogonal projection defines a null data stream. The incoherent energy is the energy associated with the auto-correlated portion of the null data. The incoherent energy is normally associated with glitches, and is given by Equation 2.40 of [51]. For the case of a 2-detector network, x-pipeline calculates and stores:

- loghbayesiancirc – a measure of the energy that x-pipeline produces, but we do not directly use for stacking.
- standard or maximum likelihood energy. This is the energy of a gravitational-wave transient \tilde{h} which maximizes the likelihood ratio of the strain data occurring under the gravitational-wave hypothesis and the null hypothesis. This is given by Equation 2.17 of [51], and is used as the default detection statistic. In practice this is the maximum amount of energy in the whitened data which remains consistent with the gravitational wave hypothesis in a specific sky direction.
- circular energy - The energy projected into a circularly polarized basis.
- circular incoherent energy
- circular null energy
- circular null incoherent energy
- powerlaw – a measure of the energy that x-pipeline produces, but we do not directly use for stacking.
- Energy in detector 1, standardized such that Gaussian noise has 1 unit of energy per time-frequency pixel
- Energy in detector 2
- Right ascension associated with the cluster
- Declination associated with the cluster

For the 3-detector network it stores these and additionally it calculates and stores the null energy, null inclination, and energy in the third detector. Each of these cluster-specific energy measures becomes a parameter which x-pipeline then uses to make cuts in the post-processing stage.

The post-processing procedure in x-pipeline makes three different optimal fixed ratio veto cuts on the above energy measures. These are the null $\frac{I}{E}$, circular $\frac{E}{I}$, and the circular null $\frac{I}{E}$. It also makes three optimal veto threshold cuts (alphaLinCutCirc) on the same quantities. After all cuts, a portion of the clusters are rejected. The optimal cuts are chosen by injecting waveforms (which replicate gravitational waves from astrophysically interesting sources) into the dummy on-source window, and calculating the $h_{\text{rss}}^{50\%}$ when considering the clusters remaining after each combination of cuts. The cuts are then tuned to optimize the $h_{\text{rss}}^{50\%}$ in the dummy on-source window.

5.3 Modifications to x-pipeline to Enable Stacking

The post-processing stage of the x-pipeline analysis uses exclusively the clusters generated in the processing stage rather than the raw data itself. These clusters, which are saved as dictionaries in hdf5 files, are each potentially gravitational-wave candidates and contain fields such as the peak frequency, peak time, number of pixels included, and several measures of energy. Stacking these clusters would merely mean choosing a means of combining together the properties of specific clusters into stacked clusters, and feeding this second round of stacked clusters into the post-processing of x-pipeline. X-pipeline would then generate a p-value for the on-source stacked cluster, and perform injections into the raw data (which are also stacked) to calculate the $h_{\text{rss}}^{50\%}$.

We want the stacking algorithm to be robust in handling discrete flares (which occur spaced out by several hours as happened in O3b), and flare forests (when many flares happen in a few minutes, as happened in April 2020 a day before the galactic FRB). We choose to treat these as two discrete astrophysical processes, and stack flares of each type with other flares of the same type. We now introduce two very similar stacking methods.

Stacking Discrete Flares

Most x-pipeline analyses [14, 82, 93, 94] are conducted with a background length of 10800 s. For a discrete flare, all or most of this time will be present around the flare without the background including another flare.

We define an on-source time window around each flare as $[-1s, 4s]$. Any cluster whose peak time falls into that time window around any of the flare times is put into the on-source time-bin of its flare. The clusters are then further broken up into frequency bins every 100 Hz ranging from 1000 Hz to 3000 Hz, the entire f -mode range. The most significant cluster in each time-frequency bin is then kept, and the other clusters are discarded.

The same process is then repeated for every 5 s time-bin in the off-source data. The loudest cluster in each time-frequency bin is kept and used in forming the background, and the others are discarded.

The on-source clusters from every flare are added together according to their frequency bin, and the same happens with every off-source time and frequency bin. Since the background contains no gravitational waves, when the significances are summed they should become more Gaussian with higher numbers of flares that are stacked. But if there were consistently low-significance gravitational waves in a

frequency bin for multiple flares, they would become relatively more significant in relation to the background as they were stacked together.

Stacking Flare Forests

The stacking of clusters accompanying flares during a flare forest is done largely in the same way as in the discrete flares case. The biggest difference is in that all of the flares lie close together, and an independent x-pipeline analysis cannot be run on each one of them. We get around this issue by adjusting the blocktime that x-pipeline originally runs with to be wide enough to include all of the flares in the forest. Then there is one block of data for the on-source, and each other block is part of the background.

For the purposes of stacking the clusters, we include a smaller on-source window around each of the flares, which we define to be $[-1 \text{ s}, 4 \text{ s}]$. All clusters falling in the on-source window of one flare will be stacked with the clusters in the on-source windows of the other flares, again by 100 Hz wide frequency bins. The difference comes in that the clusters in each off-source segment must be stacked with clusters in off-source segments which are spaced out at the same intervals as the flares themselves. This means that every off-source time block (after time slides) from the original x-pipeline analysis will provide one stacked time-bin in the background of the stacked analysis when the stacking happens on a flare forest, whereas in the discrete case this would be:

$$\frac{\text{blocktime}}{\text{on-source length}}. \tag{5.5}$$

The standard x-pipeline injection code ensures that injections are made uniformly across the on-source window. In the case of stacking the flares in a flare

forest, injections need to be made into the discrete on-source windows in the on-source block of time. The dummy on-source windows need to be set such that they are separated in the dummy time block by the same time intervals as the flares are separated by.

5.4 P-values and measures of sensitivity in stacking

In both types of stacking, our end result is a p-value, which is the probability of an event with a given significance happening under the null hypothesis (that there is no gravitational wave). This p-value is computed as:

$$\text{p-value} = \frac{\text{number of background time-frequency bins louder than on-source}}{\text{total number of time-frequency bins}}, \quad (5.6)$$

which is similar to Equation 5.1, but referring to time-frequency bins rather than x-pipeline events.

The minimum achievable p-value depends on the size of the background distribution of time-frequency bins. For now, we restrict ourselves to calculating the size of the background assuming one frequency bin, and provide a justification for this choice in Chapter 5.5. Following the discussion of background size in Chapter 5.2, we approximate the size of the background. A stacked analysis only concerns itself with gravitational waves very near the time of the trigger, and so should be using a smaller on-source window than any of the previous x-pipeline searches. We can then also use the smallest possible blocktime, 64 s, which will optimize the sensitivity of the search because the earth has less time to rotate away from the source direction. For a 64 s blocktime this implies 32 s of usable time per block, and 337 blocks of time in each detector (assuming a 10800 s background).

After time lags the total number of blocks in the background is $337 \times 337 = 113569$. We have sufficient usable data to do 10 circular time slides, which gives us a total of 1135690 independent background time blocks.

For the case of discrete bursts we assume an on-source length of 5 s. Then we have 6 time-bins in every independent block of time in the background in each frequency bin. So the background would contain $1135690 \times 6 = 6814140$ time-bins. Then the lowest possible p-value for the case of discrete bursts is:

$$P_{min}(\text{discrete}) = \frac{1}{6814140} \quad (5.7)$$

$$= 1.47 \times 10^{-7}. \quad (5.8)$$

The statistics of the flare forest case is not as obvious. As detailed in Chapter 5.3, the blocktime is set by the time span of the flare forest, and the number of time blocks after time slides determines the number of time-bins in the background.

In the event of a non-detection as indicated by the p-value distribution, we seek to determine the mean $h_{\text{RSS}}^{50\%}$ of an unstacked GW that we would have a 50% probability of being recovered after stacking. We can examine a distribution of the significances of background time-bins at each frequency to determine the significance of the stacked on-source time-bin that would have yielded a specific p-value cutoff that we arbitrarily deem to be interesting. Then the mean significance of the unstacked cluster that would constitute a detection would be

$$\frac{\text{significance of stacked flares}}{N} \quad (5.9)$$

where N is the number of flares that are stacked.

We then make injections into the raw detector data to determine the $h_{\text{rss}}^{50\%}$ of the injected signal which would produce clusters of that mean significance 50% of the time. Then this number becomes our $h_{\text{rss}}^{50\%}$ upper limit for detecting gravitational waves reminiscent of each waveform.

The goal of a stacked search is to lower the $h_{\text{rss}}^{50\%}$ of an unstacked EM event. The stacking methods we describe make it possible to do so by lowering the significance threshold that unstacked clusters must have on average for the stacked version to reach detection at a specific p-value. There are several parameters of the search that could be modified to optimize the $h_{\text{rss}}^{50\%}$ when working with a dummy on-source window:

1. The size of the frequency bins. Since the frequency of GW emission is star-dependent, we should expect that sub-threshold gravitational waves (which would benefit from stacking) would all be in a narrow frequency band. But too narrow of a band gives more frequency bins that encrue trials factors, and increase the probability of a false detection.
2. The time span included in the on-source window around each flare. If this time span becomes too small then we risk excluding a gravitational wave. We are limited on the long side by the amount of noise we are okay with adding to the on-source.
3. The time-step in the time-frequency maps on which x-pipeline identifies bright pixels to form clusters from. This effectively changes the aspect ratio of the pixels. The default timesteps are $\frac{1\text{s}}{2^N}$ where $-1 \leq N \leq 7$. Lowering the time-step might make the analysis more sensitive to short-duration signals.

4. A cutoff significance, above which we assume the cluster is due to detector noise.
5. A cutoff χ^2 value of significances of clusters, outside of which we should assume a product of instrumental noise.
6. A multiplicative weighting factor to account for the fluences in different bursts, to better constrain the ratio $\frac{\text{Gravitational Wave Energy}}{\text{Electromagnetic Energy}}$ per flare.
7. The superdecimate rate. This is a parameter of x-pipeline which limits the number of clusters that are kept by the algorithm by fixing a time rate at which the clusters can occur. The standard x-pipeline runs use a superdecimate rate of $\frac{1}{4}$, meaning that 1 cluster is allowed per 4 seconds of usable time in the background. There is no necessity for these clusters to be uniformly distributed in time.
8. A cutoff percentile of pixel brightness which signals x-pipeline to make a cluster. The default for most x-pipeline analysis [14, 16, 82, 93, 94] is 1%. Raising this means that more pixels in each time-frequency map are identified as bright pixels. The number of total clusters that x-pipeline keeps after the first stage of processing is set by the superdecimate rate, so the bright pixel percentage would not effect the number of clusters. The extra bright pixels could, however, fall adjacent to the pixels in the brightest 1%, which would mean that the total significance of the expanded cluster would rise. Raising this parameter might make the distribution of significances of the clusters.

We preform sensitivity studies to attempt to optimize the properties of stacked searches.

5.5 Sensitivity Studies

Bright pixel percentage

We have previously introduced and discussed in Chapter 3.2 the three x-ray flare events which came from an unknown source. We assume that these all came from the same source (they occurred in the same 33-hour time window). Since in nearly every emission model, the properties of the gravitational wave are dependent on the properties of the star, these three flares are a viable candidate for stacking. We use the results of the O3 x-pipeline runs on these flares to adjust parameters and optimize the sensitivity of the stacked search. We define specific parameters with which to run our sensitivity studies aimed at tweaking other parameters to optimize the search sensitivity. We define the on-source window to be $[-1 \text{ s}, +4 \text{ s}]$ around the time of the flare, and we search between frequencies 1000 Hz and 3000 Hz. Since the signals we expect to be produced are short duration, we conservatively set our maximum time-step size in x-pipeline to be .25 s.

In order to find the optimal percentile of pixel brightness to create a cluster, we run the analysis stage of x-pipeline on each of the three triggers varying the cutoff acceptance brightness from 1% to 5%. The clusters in the background of these analysis each contain a significance relative to the other clusters in the same flare. We combine the clusters from each of these triggers run with different brightness cutoffs and histogram the distributions in Figure 39. This histogram shows that when the cutoff brightness percentile threshold is raised to allow more dimly lit pixels, the distributions move to higher significance and broaden. Given that the significance of a cluster is the sum of the significance of its constituent pixels in the time-frequency maps, we would expect this to happen because each

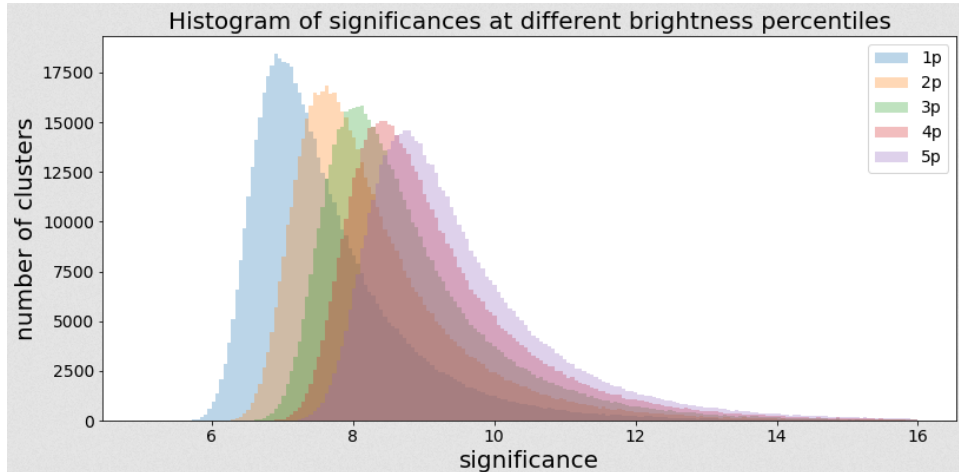


FIGURE 39. Histograms of the distributions of significance values of all clusters from x-pipeline runs on triggers 2669, 2670, and 2671 from [1], all of which were from an unidentified source. The different distributions represent the percentile of pixels in a time-frequency map that the pipeline considers to be bright enough to be included in the clusters, and we plot the distributions of brightness cutoffs between 1 percent and 5 percent. In these distributions we only consider clusters with central frequencies between 1000 and 3000 Hz, and use timesteps of $\frac{1}{2^N}$, where $2 \leq N \leq 7$.

cluster effectively gained some pixels. These distributions also become less peaked, so choosing one with a higher pixel acceptance rate might make it easier to reject clusters above a threshold significance, and still have a sufficiently broad range of significances.

Superdecimate Rate

We now turn our attention to the superdecimate rate, which is the number of clusters that x-pipeline keeps per second of data, averaged over each block of time it analyzes. The standard x-pipeline runs in previous LIGO/Virgo papers [14, 16, 82, 93, 94] use the x-pipeline default rate of $\frac{1}{4}$. The total number of clusters in these studies are fixed so that on average there exists one cluster for

every 4 seconds. This is a default parameter in the pipeline which has never been investigated for optimization.

For the purposes of stacking, low values of the superdecimate rate will result in a lower percentage of time-frequency bins containing an event before stacking, resulting in a more sharply-peaked distribution of significance values after stacking. Depending on the number of triggers, there might even be large numbers of time-frequency bins with zero significance after stacking. A high superdecimate rate means fewer time-frequency bins without constituent clusters, but it also means that more low-significance noise is included in the data. Since the purpose of stacking is to search for low-significance but consistently present gravitational waves, the parameters of the first stage of the x-pipeline runs should reflect the need to include an elevated number of clusters. This would be done with a higher superdecimate rate.

Since the effects of the superdecimate rate on the sensitivity of an unstacked x-pipeline analysis have never been studied, we run x-pipeline on four different triggers from O3, using four different values for the superdecimate rates. We standardize the sensitivity of the runs by the $h_{\text{rss}}^{50\%}$ of the ringdown waveform at 1590 Hz with a characteristic damping time of 100 ms. These sensitivities are plotted for all four runs against their superdecimate rates in Figure 40 and the percentage of difference in sensitivity between the most and least sensitive superdecimate rate is displayed for each trigger in Table 15.

It is clear that for most of the triggers, the superdecimate rate has very little effect on the sensitivity of the run, at least for the rates in our sample. Trigger 2652 is the exception to this; a superdecimate rate of $\frac{1}{4}$ seems to yield sensitivity that is $\approx 15\%$ lower than the runs with either higher or lower superdecimate rates.

Trigger Number	% change in sensitivity
2652	15.1%
2654	0.00%
2655	0.37%
2656	0.54%

TABLE 15. We show the percent change in sensitivity as measured by the $h_{\text{rss}}^{50\%}$ of the 100 ms ringdown waveform at central frequency 1590 Hz when comparing the runs at the most and least sensitive superdecimate rate. For trigger 2652 this change is 15.1%, and specifically there is an outlier superdecimate rate of $\frac{1}{4}$ which reduces the sensitivity of this run. The other superdecimate rates yield a nearly constant sensitivity for trigger 2652. The other triggers have very negligible differences in their sensitivities when run with different superdecimate rates.

It is not obvious a priori that any given rate yields a more sensitive search than any other rate. So in choosing a superdecimate rate for the stacked search, it would likely be beneficial to choose a higher rate such that a higher percentage of time-frequency bins are populated.

Frequency range and bin sizes

Astrophysical models attribute the f -mode gravitational wave frequency to a combination of the mass, radius, and EOS of the neutron star producing it. These properties are star-dependent, not flare-dependent, so we reasonably assume that these flares from the same magnetar fall within the same frequency bin, and that we should be able to make those bins quite small without excluding a flare. We now examine the practicality of these assumptions.

As a preliminary method of investigating the evolution of the significance of a stacked as more triggers are added to the stack, we treat the first 57 background segments of the delayed short-duration search over magnetar x-ray trigger 2656 as

Sensitivities at different superdecimate rates

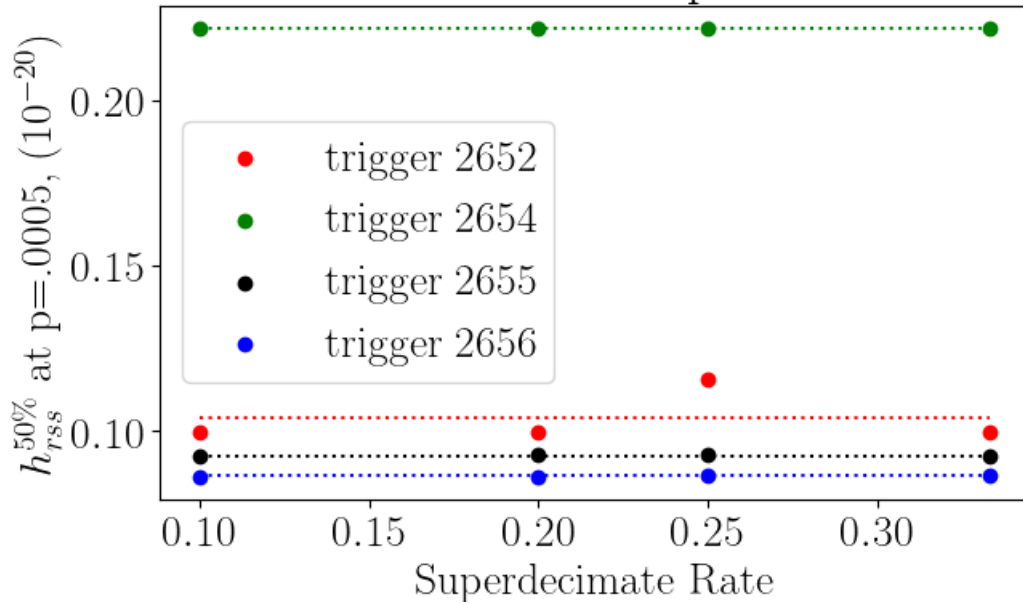


FIGURE 40. A plot of the sensitivities of the searches on four different magnetar triggers in O3 done at four different superdecimate rates ranging from $\frac{1}{10}$ to $\frac{1}{3}$. The sensitivity is standardized by the $h_{\text{rss}}^{50\%}$ of the ringdown waveform at 1590 Hz with damping time 100 ms. The superdecimate rate is a parameter of x-pipeline which determines the rate at which the clusters are allowed to appear in the data. The standard x-pipeline runs are done with a superdecimate rate of $\frac{1}{4}$, meaning that there is 1 cluster per 4 seconds of data on average, but that the clusters need not be uniformly distributed in time. The mean sensitivities for each trigger across all superdecimate rates are plotted as dashed lines.

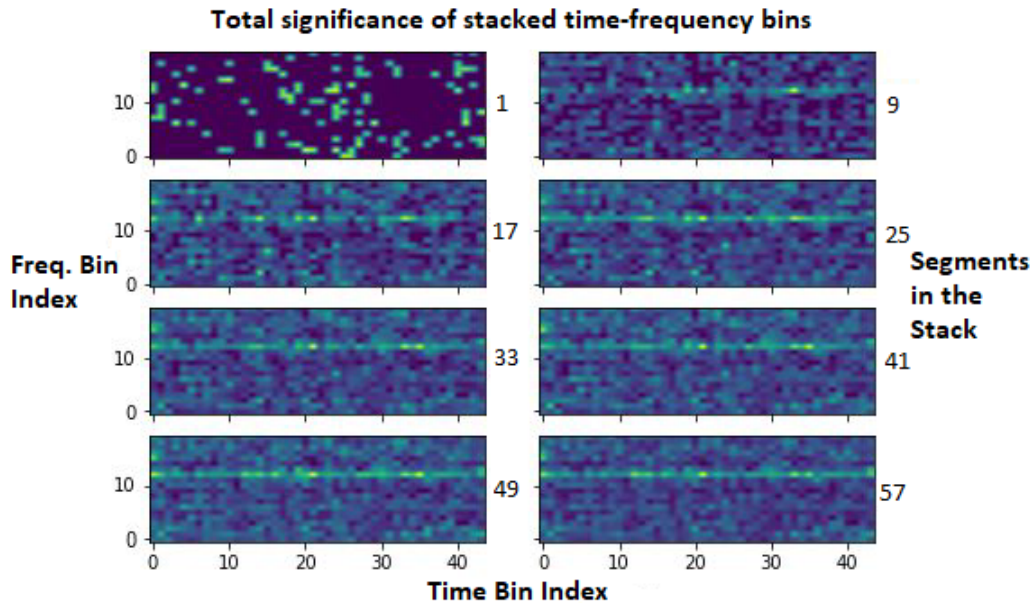


FIGURE 41. We plot the evolution of the distribution of stacked significances with the number of triggers in the stack ranging from 1 to 57. The frequency bins are 100 Hz wide and span from 1-3 kHz, with their index given on the left of each subplot. Time bins are 5 s in duration, with their index on the horizontal axis. For the purpose of saving computing resources, for this preliminary study we use background segments from the delayed short-duration search over Trigger 2656 described in Chapter 3.3, and stack them as though they were independent triggers. We see that the total significance of the stacks tend toward a mean significance as more triggers are added, and we also see that certain frequency bins have disproportionately high significance.

independent triggers. We then stack the clusters falling between 1000-3000 Hz with significance less than a cutoff of 13.

In Figure 41 we show these significances for every time-frequency bin for $N = 1 + 8k$, where N is the number of triggers in the stack, and k is an integer ranging from 1 to 7. There are two noteworthy elements of this figure: as more triggers are added to the stack, the significance of each time-frequency tends toward a mean value. Secondly we note that certain frequency bins have a higher significance than others, which is surprising because x-pipeline whitens the data before the first stage of processing when the bright pixels are identified. Non-

stationary noise in a detector would not have been whitened adequately, and so it is likely that the significance preference toward specific frequency bins is due to wandering lines in the noise spectrum.

It is obviously not reasonable to compare the significance of one frequency bin at the on-source time to the significance distribution of the off-source times of a different frequency bin given the frequency-dependent distribution of background clusters. So then each on-source time-frequency bin can only be compared to the background distribution at the same frequency. This would leave a distribution of p-values, one for every frequency. It also needs to be noted that we would expect at most one of these on-source stacked time-frequency bins to contain a gravitational wave; so when we examine the distribution of p-values, we care about low outliers, not the mean of the distribution.

But when we have multiple p-values and we are merely concerned with the lowest, we can calculate a total probability of having at least one p-value less than a specific value by:

$$\text{Prob}(p \leq P) = 1 - (1 - P)^F \tag{5.10}$$

where F is the number of p-values, each corresponding to a frequency bin. So if we assume that a p-value of 5×10^{-4} constitutes a threshold below which an event becomes interesting, and we have a distribution of 20 frequency bins, the probability of achieving this p-value if the p-values followed a uniform distribution from $0 < p \leq 1$ is:

$$\text{Prob}(p \leq 5 \times 10^{-4}) = 1 - (1 - 5 \times 10^{-4})^{20} \quad (5.11)$$

$$= 1 \times 10^{-2}. \quad (5.12)$$

The effective p-value drops as we increase the number of frequency bins, which effectively means that the significance of each of the events in the stack would have to be greater to yield the same effective p-value. There are various strategies that one could employ to mitigate this; we could merely restrict the frequency range of our search, and then be aware that there is some probability that we miss a stacked gravitational wave which fell outside of our restricted frequency range. We could also raise the frequency bin size such that we can cover the same frequency band but with fewer bins, but this would mean reduced ability to perform any parameter estimation on the signal if one were found. The last option is to wait for theorists to provide us with tighter physically motivated restrictions on the frequency range at which we should expect to see such a gravitational wave.

5.6 The Mean Significance required to produce a given p-value

We now demonstrate that stacking multiple bursts reduces the mean cluster significance per burst necessary to produce a specific p-value, and we investigate how this mean significance changes in relation to how many bursts are stacked. We do this by running the first stage of x-pipeline on the nine magnetar x-ray flares from O3b, and also on eight non-repeating FRBs from O3a. We stack the outputs of the FRB runs along with the magnetar runs so that we can extend our studies of

the p-value beyond the number of magnetar bursts available in O3. We run these searches with 64 s blocktimes, 10800 s backgrounds, a bright pixel percentage of 1%, and the rate of clusters standardized at 1 cluster per 4 s of background data (averaged over the entire background). We constrain the frequency range to 1500 Hz to 1900 Hz, and make no impositions as to how these clusters are distributed over that range.

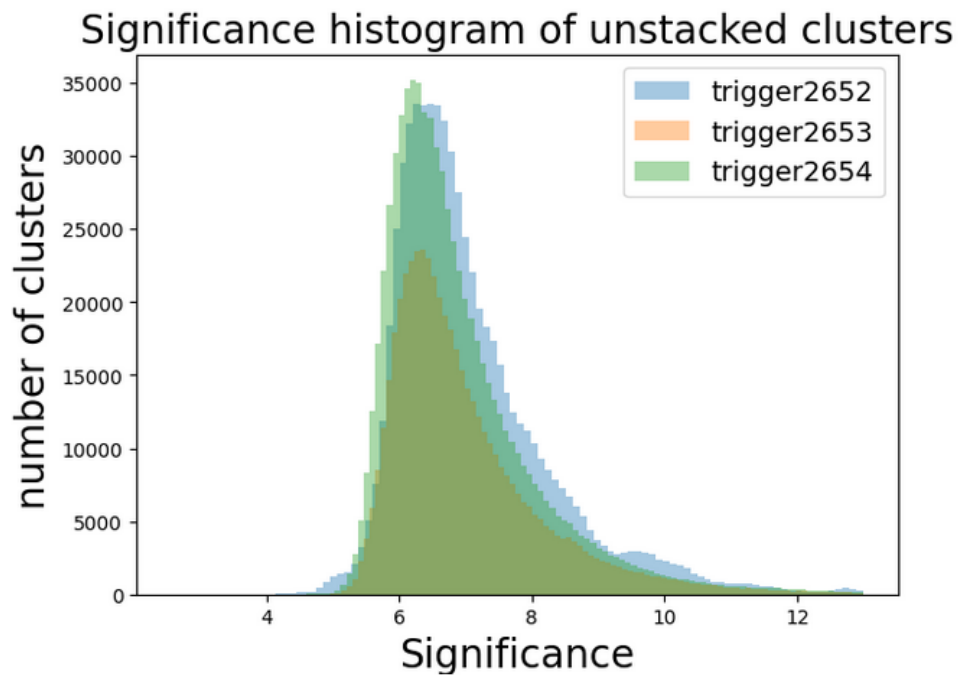


FIGURE 42. Histogram of the significance values of the clusters generated by the runs on triggers 2652, 2653, and 2654 before stacking, between 1500 and 1600 Hz. The overlap of these distributions shows that the significance of the clusters in the x-pipeline output is independent of the sensitivity of the detector network. Trigger 2653 has fewer clusters because it has less background time available, and a higher percentage of its clusters could fall in a frequency bin not shown here. We also see an overpopulation of clusters with significance approximately 10 in trigger 2652; this could be caused by a specific type of glitch being more common in the background of that analysis, and might become a source of noise for the stacked search.

For this study we specifically examine clusters falling in the frequency bin from 1500 Hz to 1600 Hz. We also set a maximum significance on the clusters

of 13, disregarding louder clusters as more likely instrumental noise than low-significance astrophysical signals. A histogram of the significance of each cluster in the first three triggers from SGR 1935+2154 (2652, 2653, and 2654) is shown in Figure 42. We see that trigger 2653 has fewer clusters than the other two triggers. Trigger 2653 happened at a time when some of the background data did not pass the data quality ramifications to be included in the background, and so has fewer background clusters than the other two. It is also possibly the case that this analysis had non-stationary noise in a frequency band outside of the 1500 Hz frequency bin, and a lower percentage of the clusters fell in the frequency bin that we histogram here. We also see that in order for any of these triggers to have an on-source cluster with a low p-value (before stacking), the significance of that cluster would have to be quite high – likely higher than 13.

In Figure 43 we have included histograms of the number of time-bins that contain a total significance after a given number of bursts are stacked. When only two triggers are stacked most of the time-bins still have zero significance – this is because no clusters fell into those bins. This merely shows that if stacking is to be used for low numbers of triggers, then the analysis parameters need to be adjusted such that a greater total number of clusters are generated by the first stage of the algorithm. We see that as more triggers are stacked the distribution of significances becomes more broad, and also shifts to higher values.

A histogram of the stacked significances with more bins, presented in Figure 44, shows a periodicity of approximately 7 at lower significance values. This effect reflects the distributions of the unstacked significances (shown in Figure 42), which are sharply peaked and centered near a value reminiscent of this periodicity. During the stacking process, each stacked time-frequency bin either remains at

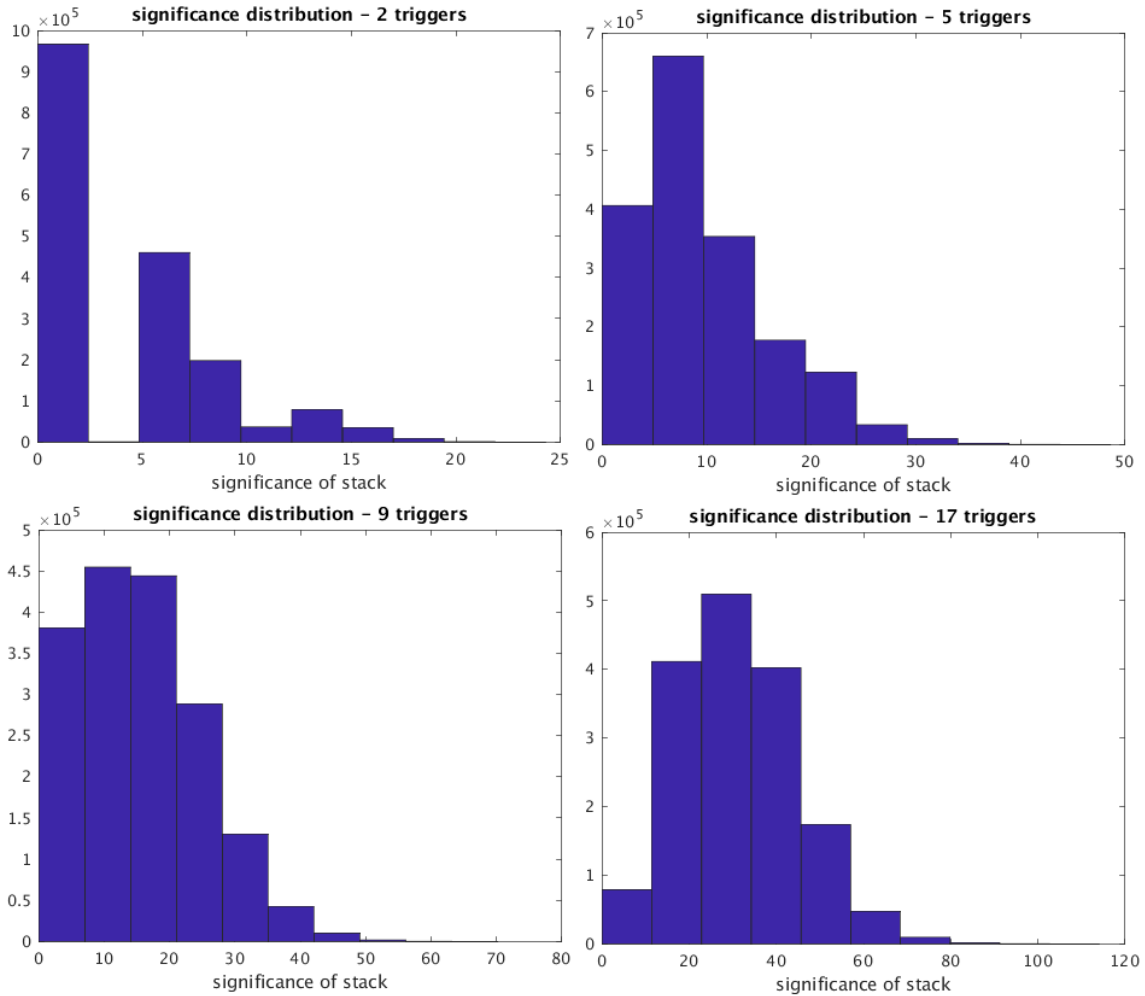


FIGURE 43. Histograms of the significance of the stacked triggers without weighting. The original x-pipeline runs are over a frequency range of 1500-1900 Hz at a cluster rate of 1 per 4 s, and these histograms show the triggers in the 1500-1600 Hz bin. We include the histogram for 2, 5, 9, and 17 triggers in the stack, and we see that the distribution moves to higher significance as more triggers are added to the stack.

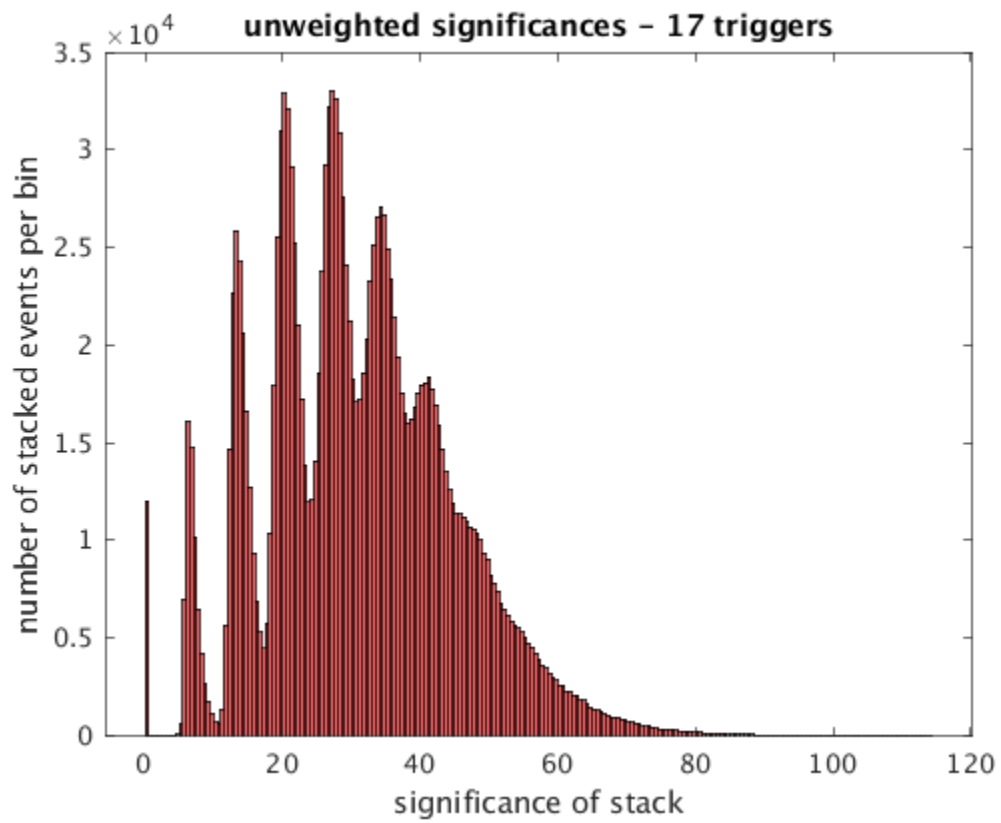


FIGURE 44. Histogram of the significances with 17 triggers in the stack, shown with smaller histogram bin width. There are periodic spikes at lower significance, but the higher significance part of this distribution is relevant for this analysis.

zero significance if no clusters fall into it, or else has a significance approximately proportional to the number of clusters it contains. We see a smoothing of this periodicity at around 40, which can be explained by the spread in the unstacked significance distribution.

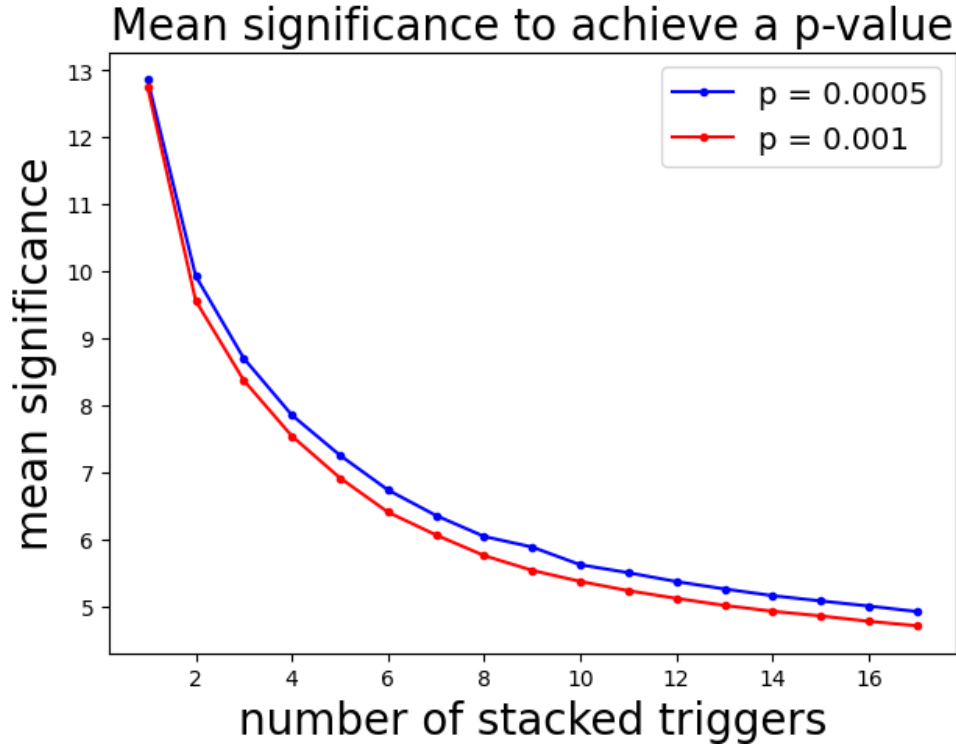


FIGURE 45. The mean significance required of the unstacked triggers for their stacked counterpart to have a specific p-value, 1×10^{-3} or 5×10^{-4} . The mean significance reduces with more triggers in the stack. This data is also displayed in Table 16.

Now assume that a p-value of 5×10^{-4} constitutes an event that is interesting. We can use the significance distribution of the stacked bins to estimate the threshold significance of the stack that would yield this p-value. The mean significance of the unstacked trigger is then this threshold divided by the number of triggers stacked. We note that with low p-values, the only part of the stacked

significance distribution that is important is the high-significance part of it, where the periodic spikes in Figure 44 have already faded away.

We have stacked 17 triggers (nine from SGR 1935+2154 and eight at the times of the FRBs), and calculated this mean significance threshold after each trigger is added to the stack in order. The results are plotted in Figure 45. This figure shows a sharp drop in the mean significance needed to achieve a specific p-value until about 10 triggers are stacked, and after that we do still see improvement, but it is minimal. At 17 triggers in the stack we see the requisite significance drop to 4.9, an incredible improvement from the > 13 required without stacking. The specific mean significance per trigger in the stack is given in Table 16 for stacks ranging in size from 2 to 17.

It must be noted that not all triggers should be weighted equally. The two most obvious reasons are fluctuations in the sensitivity of the detector network, and unequal fluences of the electromagnetic bursts. For the purpose of including weighting in our significance reduction demonstration we consider only weighting due to detector network sensitivity. We define the network sensitivity of each trigger as:

$$\text{Network Sensitivity} = \sum_{\text{Detector}} \text{BNS range} \times \text{Antenna Factor} \quad (5.13)$$

where the BNS range is the angle-averaged distance at which a binary neutron star inspiral involving stars of 1.4 solar masses can be detected with SNR= 8. Then the weight assigned to each trigger in the stack is:

$$W_{\text{trigger}} = \frac{\text{Network Sensitivity}}{\sum_{\text{triggers}} \text{Network Sensitivity}} \times N \quad (5.14)$$

Number of triggers	Mean Significance	
	$P = 5 \times 10^{-4}$	$P = 1 \times 10^{-3}$
1	12.87	12.75
2	9.93	9.56
3	8.70	8.37
4	7.85	7.54
5	7.25	6.91
6	6.73	6.40
7	6.35	6.06
8	6.04	5.75
9	5.88	5.53
10	5.62	5.37
11	5.50	5.23
12	5.37	5.11
13	5.25	5.01
14	5.15	4.92
15	5.08	4.85
16	5.00	4.77
17	4.92	4.71

TABLE 16. We show the mean significance needed in the unstacked triggers to give stacked p-values of 5×10^{-4} and 1×10^{-3} for all numbers of triggers in the stack ranging from 2 to 17. The values for 1 trigger in the stack are obtained through the normal x-pipeline post-processing stage of analysis, and include no stacking.

where N is the number of triggers in the stack. This weighting scheme has the property:

$$\sum_i W_i = N. \tag{5.15}$$

This effectively separates the distributions of significances from each trigger, but the mean significance from all triggers remains constant, as shown in Figure 46. We stack the same 17 triggers as in the unweighted case, and histogram the significances in Figure 47. We again see the distribution of stacked histograms move higher and become more spread out as more events are stacked.

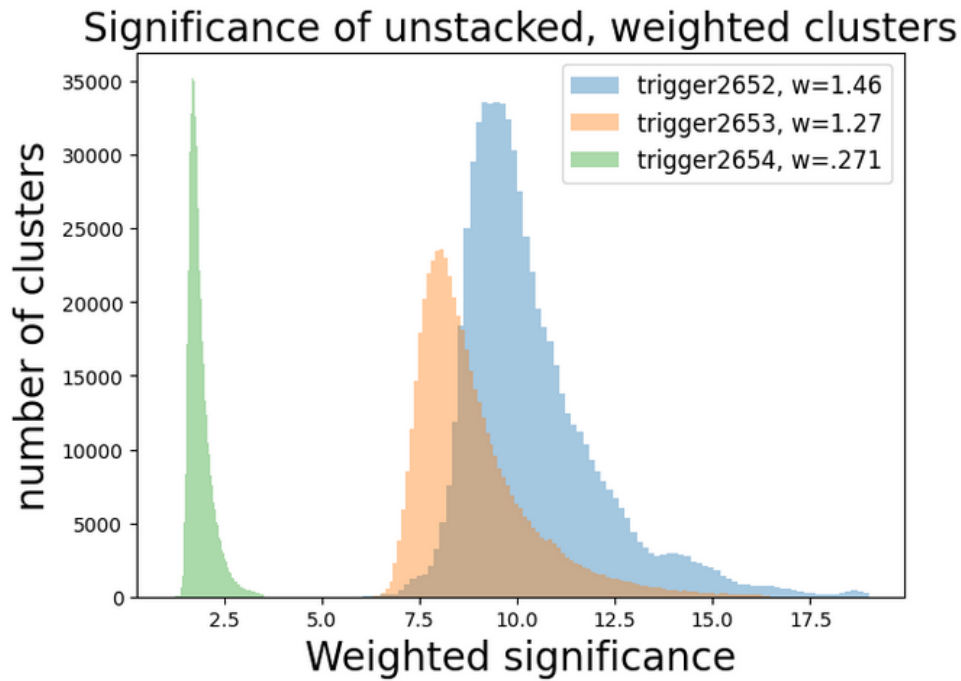


FIGURE 46. Histogram of the significance values of the clusters generated by the runs on triggers 2652, 2653, and 2654 before stacking, weighted by the network sensitivity. The distributions of sensitivity separate according to network sensitivity, and the total range of sensitivities increases over the unweighted case shown in Figure 42.

We again define the threshold for a p-value to be considered interesting at 5×10^{-4} . We stack the 17 flares as before to calculate the mean significance of

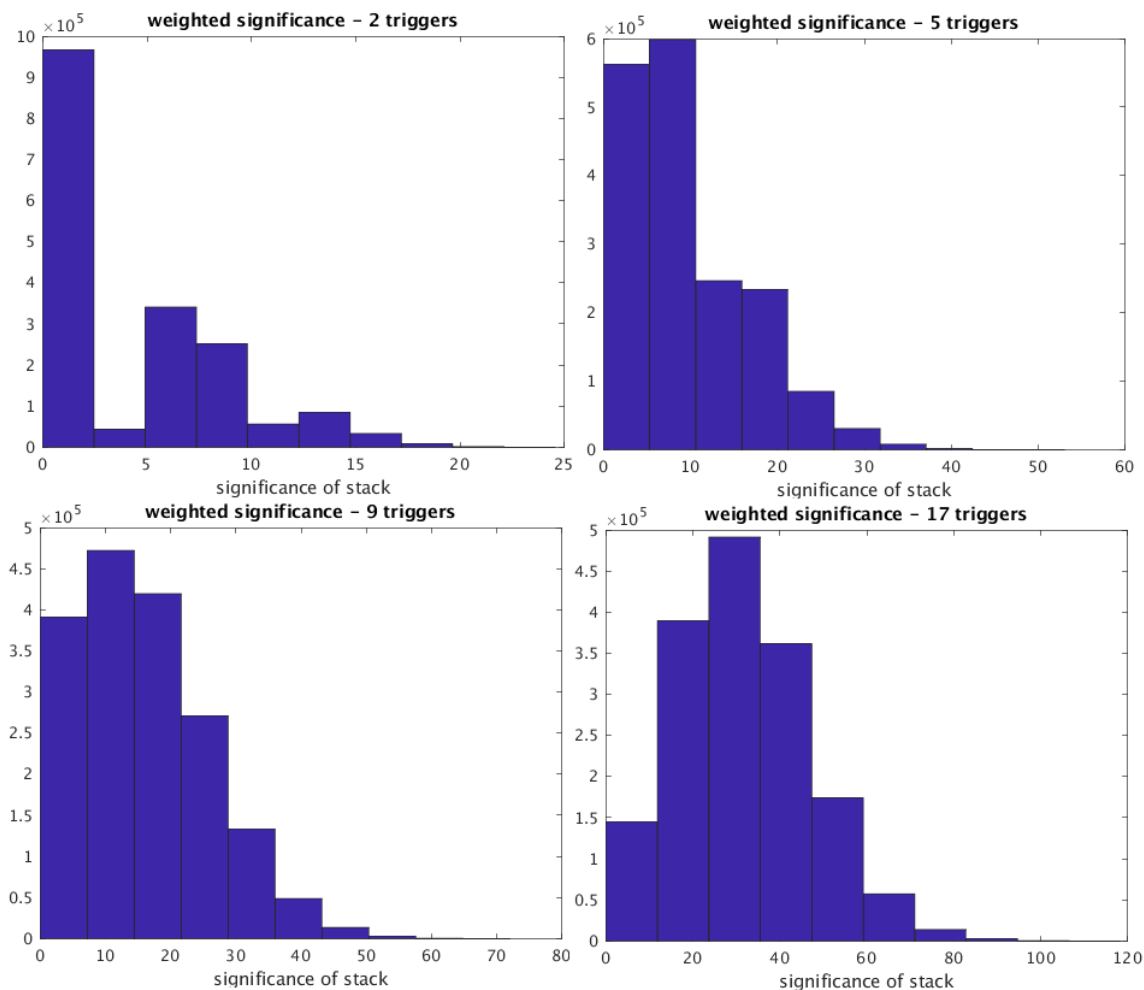


FIGURE 47. Histograms analogous to the ones shown in Figure 43, but with the significances weighted according to the sensitivity of the detector network. We see a similar result as in the unweighted case; the distributions move to higher significance with more triggers in the stack. There is also more distinct broadening of the distributions with more triggers. This is because the range of significance values of the unstacked triggers is wider in the weighted case, as evidenced in Figure 46.

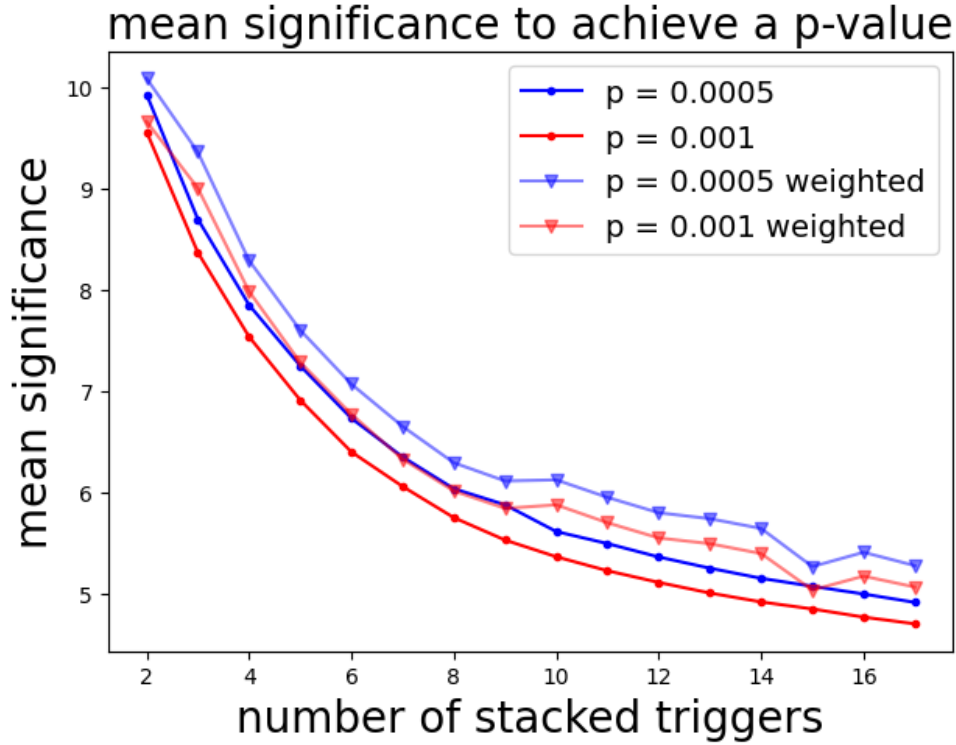


FIGURE 48. The mean significance required of the unstacked triggers for their stacked counterpart to have a specific p-value, 1×10^{-3} or 5×10^{-4} , when weighted according to network sensitivity. The weighted case is denoted by triangles, and is consistently somewhat higher than the unweighted case. This is to be expected when the sensitivity distributions spread out with weighting.

an on-source cluster that gives this p-value. We plot these mean significances in Figure 48.

The mean significance required of an unstacked cluster to create a specific stacked p-value is greater for the weighted search, independently of the number of triggers in the stack. This is a sensible outcome given that this threshold mean significance is determined by the high-significance end of the stacked significance distribution shown in Figure 49. The weighting scheme means that the high-significance constituent clusters in each stack become higher significance, and the distribution of stacked significances is more broad than in the unweighted case. We

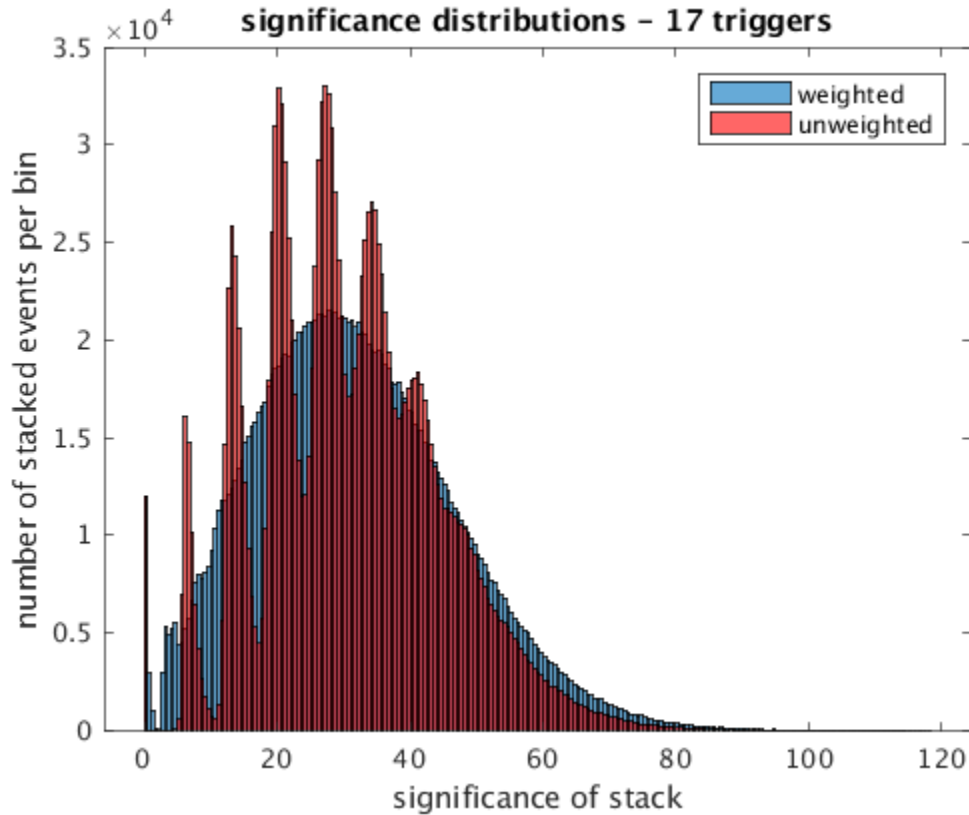


FIGURE 49. Histograms of the significances with 17 triggers in the stack, shown with smaller histogram bin width. There are periodic spikes at lower significance, but the higher significance part of this distribution is relevant for this analysis.

also note the absence of the periodicity shown in Figure 44, because the weighted clusters from each trigger are not centered around the same mean.

We have demonstrated that the mean significance of a cluster in each unstacked trigger can be as low as 4.9 and still register a stacked p-value of 5×10^{-4} in the case of unweighted significances. We can compare this number (and more broadly, the mean significances given in Table 16) to the distributions of unstacked significances in Figure 42, and see that the required mean significances of the unstacked clusters are very much on the low end of the distribution of available clusters. This is convenient from a proof of concept point of view, because

the requisite mean significance is certainly available after the first stage of the x-pipeline runs. It is possible that we could gain sensitivity by adjusting the parameters of the search such that the distribution of significances after the first stage of analysis is broadened; this could be achieved by lowering the black pixel percentage, as evidenced in Figure 39, and by raising the superdecimate rate.

5.7 A demonstration of the reduction of the $h_{\text{rss}}^{50\%}$ with stacking

In Section 5.6 we have established a series of values of the mean significance of a consistently present unstacked event that could be detected with a specific number of triggers in the stack. It should be noted, however, that the significance is a somewhat arbitrary property of a cluster produced by the first stage of an x-pipeline analysis. The significance of any given cluster is only comparable to other clusters in the analysis of the same trigger, as evidenced by the good overlap of significance distributions between the three triggers shown in Figure 42 when those three detector networks have vastly different sensitivities. The goal of this section is to establish sensitivity estimates in physical units.

We use the post-processing algorithm of x-pipeline to establish a value of $h_{\text{rss}}^{50\%}$ in an unstacked analysis which corresponds to the mean significance for a stacked detection. The process to find the $h_{\text{rss}}^{50\%}$ for a specific trigger corresponding to a given mean significance S is as follows:

1. We calculate a local p-value from the significance distribution of that trigger which corresponds to significance S . We do this by considering the significance distribution returned by x-pipeline for that trigger, and discarding all clusters with significance greater than 13 (the cutoff we used). The local p-value is then:

$$P_{\text{local}} = \frac{N_{\geq S}}{N_{\text{remaining}}} \quad (5.16)$$

where $N_{\text{remaining}}$ is the number of triggers that remain in the distribution after discarding the ones with significance greater than 13, and $N_{\geq S}$ is the number of remaining triggers with significance $\geq S$.

2. The x-pipeline post-processing algorithm takes as an input parameter a p-value by which to standardize its detection sensitivity for the closed boxes. We run the post-processing script with the input p-value set as the local p-value calculated in the first step.
3. The x-pipeline post-processing algorithm then makes injections into the dummy on-source window and calculates a value of $h_{\text{rss}}^{50\%}$ at which the injections are recovered with 50% efficiency with the false alarm probability set by the local p-value.
4. An approximation of the increase in sensitivity after stacking can be measured by the $h_{\text{rss}}^{50\%}$ as returned by the closed box of an unstacked trigger, with the p-value set to the local threshold as calculated in the first step.

We follow this procedure to calculate the $h_{\text{rss}}^{50\%}$ corresponding to a mean significance for different numbers of flares in the stack. We do this for both triggers 2655 and 2656 using the 100 ms ringdown waveform at 1590 Hz. These $h_{\text{rss}}^{50\%}$ values are displayed in Table 17. One difficulty we faced when determining the reduction in $h_{\text{rss}}^{50\%}$ (and why the reason why Table 17 is sparsely populated) is that we specify the significance in x-pipeline by choosing the dummy on-source window accordingly. But this method does not guarantee that the event of the significance we have chosen survives the pipeline cuts to give our $h_{\text{rss}}^{50\%}$ value.

Number of triggers	$h_{\text{rss}}^{50\%} (\times 10^{-22} \frac{1}{\sqrt{\text{Hz}}})$	
	trigger 2655	trigger 2656
1	2.17	2.03
2	1.85	1.75
3	-	1.62
5	1.36	1.51

TABLE 17. We show the $h_{\text{rss}}^{50\%}$ of two individual triggers, 2655 and 2656, which corresponds to the mean unstacked significance needed to make a detection of a stacked trigger with $p = 5 \times 10^{-4}$. We see a reduction in the $h_{\text{rss}}^{50\%}$ in both cases. An entry ‘-’ indicates that the post-processing was not completed.

For the post-processing runs that were able to finish however, Table 17 does show a reduction in $h_{\text{rss}}^{50\%}$ with more triggers added to the stack.

5.8 Efficacy of stacking N triggers

We have introduced a method of performing a stacked search over repeating burst signals from a consistent source which is an extension of an excess power search. This makes it more reminiscent of power stacking, although we note that our method is fundamentally different from power stacking in that we combine clusters of pixels from corresponding time-frequency bins rather than the individual pixels themselves. We can compare the efficacy of the method to previous methods, as well as make predictions on the number of triggers needed in the stack to achieve a specific improvement in the $h_{\text{rss}}^{50\%}$ by fitting functions to describe the mean significance to reach a specific stacked p-value.

We assume that the relationship between the mean significance to obtain a specific p-value (S) and the number of triggers (N) can be adequately described by an equation of the form:

$$S = b + m \times N^{-a} \tag{5.17}$$

where b , m , and a are constants. It is obvious that the relationship between S and N should contain an additive constant; this is a result of the superdecimate rate parameter causing a cutoff at the low end of the significance distributions at a significance of ≈ 4 . It appears visually that a power law could adequately describe the data in Figure 42. These equations of best fit for $p = 5 \times 10^{-4}$ and $p = 1 \times 10^{-3}$ are respectively:

$$S_{5 \times 10^{-4}} = 1.78 + 11.32 \times N^{-0.46} \quad (5.18)$$

$$S_{1 \times 10^{-3}} = 1.97 + 10.83 \times N^{-0.49}. \quad (5.19)$$

The accuracy of these equations can be determined from Figure 50, where they are plotted and overlaid with the data from which they were generated.

The significance of the least significant unstacked cluster from each of these analysis varies widely, but the mean value across all nine magnetar triggers analyzed in O3a is 3.19. This means that as we approach a cluster significance of 3.19, it becomes increasingly probable that a real gravitational wave event of that significance (even if one were present) would not be energetic enough to be included in the clustered output of the first stage of the x-pipeline analysis. Our analysis in this case would be meaningless, and necessitate the use of less restrictive x-pipeline analysis parameters (such as a higher superdecimate rate and a higher bright pixel percentage). We see from Table 16 that with 17 triggers in the stack, the mean unstacked significance would have to be 4.9 in order to achieve a p-value of 5×10^{-4} . Equation 5.18 implies that approximately 93 triggers are needed for this mean significance to drop as low as 3.19.

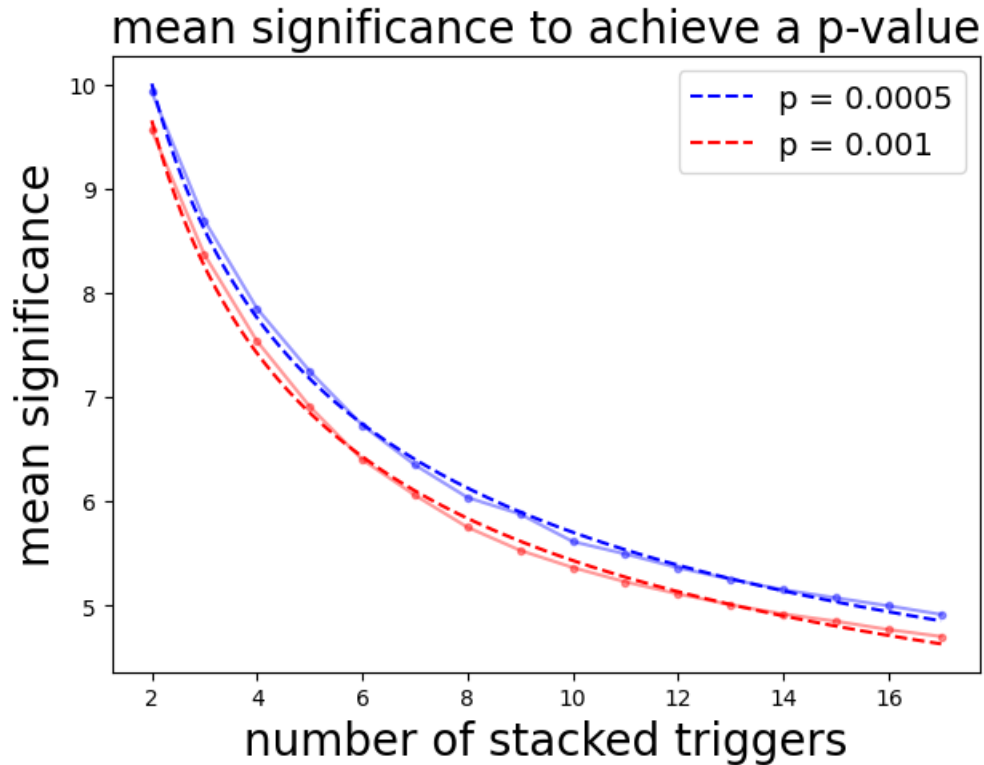


FIGURE 50. We plot the equations of best fit describing the relationship between the mean significance needed to achieve a specific p-value, and the number of triggers in the stack. We do this for both $p = 1 \times 10^{-3}$ and $p = 5 \times 10^{-4}$, and overlay it with the calculated mean significance for each stack size. The fit is done assuming that the mean significance (S) can be reasonably well-described by $S = b + m \times N^{-a}$, where b , m , and a are constants, and N is the number of triggers in the stack.

5.9 Conclusion

In this chapter we introduce a method of stacking in which we combine the cluster data from multiple individual x-pipeline analyses to search for lower-significance but consistently present gravitational-wave signals. Our method is reminiscent of the power-stacking method noted in [80] in that it combines properties of coherent time-frequency maps, however we are merely combining the unions of the brightest pixels from these maps and not the maps themselves.

A very preliminary study has shown that these clusters favor specific frequency ranges over others which is likely an effect of non-stationary noise in the data (the whitening process is most effective on stationary noise). This means that any realistic comparison between the on-source and the off-source data must happen within a given frequency bin, for example 1500-1600 Hz as used in the sections above. The present understanding of gravitational waves from magnetar flares is that the most detectable non-radial mode is the f -mode, and that the frequency is poorly constrained between approximately 1 and 3 kHz, as described in Chapter 1.3. Searching in 100 Hz frequency bins spanning this range would yield 20 independent p-values, and further statistics would be needed in order to make much of an astrophysical claim. The upshot, however, is that magnetar emission theory is a rapidly evolving field and there is every probability that at some point this frequency range will be further constricted, or at least further constricted on a star-by-star basis. This would allow tighter frequency bins to be used, and fewer of them.

The standard x-pipeline detection statistic is the significance of a cluster, and the significance of the clusters after the first stage of x-pipeline processing begins at approximately 3.2, and we define a significance cutoff at 13, with very few clusters

falling at values greater than this. The significance needed to make a detection with $p = 5 \times 10^{-4}$ with just one trigger is very nearly 13. We have demonstrated that this number is reduced with multiple triggers in the stack, and that it can go as low as 4.9 with 17 triggers, as shown in Table 16 and Figure 45.

Stacking could be useful as a method of analysis if large numbers of triggers come from the same source. There are tentative O4 LVK plans to include a paper including a stacked analysis over repeating sources, both magnetar flares, and repeating FRBs. Stacking would prove most useful if there was a source with a large number of events, on the order of tens.

CHAPTER VI

APPENDIX

6.1 Documentation of the new x-pipeline Stacking Features

Here we document the main new scripts and functions that have been added to x-pipeline to enable the stacked searches. All scripts live in the x-pipeline stacking branch, and also in the x-pipeline folder in the home directory of the LIGO computing cluster.

tfBinCluster.m The easiest way to identify an event as belonging to one time-frequency bin or another is to re-assign the relevant time and frequency fields to ones which fall on integer multiples of the time and frequency bin size. This function takes as arguments a cluster object saved by x-pipeline's pre-processing stage, a minimum and maximum frequency which define the range of frequencies we will stack, the frequency range of each bin (df), and the time-span of each bin (dt). This function bins all of the events in the cluster object, and then stores the original frequency and time fields as new unstacked fields, which will be ignored by the post-processing stages of analysis, but will remain available for follow-up on any interesting results.

The off-source files contain events resulting from circular time-slides, which are by default 3 s in length. These time-slid events are assigned the times of the unslid detector, which results in a higher time-density of events in the off-source data than in the on-source data. This provides a problem when we stack the loudest event per time-frequency bin to stack, and each off-source

bin has more events to choose from than the on-source bins. We mitigate this problem by assigning the time values of the slid off-source events to be

$$T_{\text{off-source}} = T_{\text{unslid detector}} + N \times L \quad (6.1)$$

where N is the number of circular time-slides of the event, and L is the amount of usable time used in the circular time-slide. The minimum `blockTime` on which the analysis is run is 64 s, and 16 s are removed from each end of that to be used for whitening the data. This leaves 32 s of usable time in which time-slides are done, so $L = 32$. This method of handling the time-slides does leave open the possibility of creating a 32 s periodicity in the events that is not present in the raw data. This could be the case if there were some excess noise in one detector which was heavily weighted enough to create an event in each time-slide, and then those events were assigned times exactly 32 s apart.

This script then takes as starting and stopping times the first and last event times, and steps through each interval in time-frequency space by steps of dt and df , and assigns each event to the lower bounds of time and frequency of the bin it resides in. The script then returns a binned version of the cluster object, where each event is already assigned to a time-frequency bin.

This script is an executable file that is called by Condor, and its arguments are inherently passed in as strings. We change them back to numbers using, for example:

$$df = \text{str2num}(df). \quad (6.2)$$

Running the script locally without Condor requires the str2num conversion lines to be commented out. Running locally also allows the user the option of downsampling the data to make the process run faster, by changing the hard-coded variable `time_reduction_factor`.

stackMultipleClusters.m This is the script where the stacking actually happens. It takes as arguments a lists of cluster objects, minimum and maximum frequencies defining the range of frequencies to stack, a maximum significance above which an event is discarded as being a loud glitch, the frequency bin size (`df`) and the time bin size (`dt`). For each cluster in the list it calls `tfBinCluster()` to bin each event in the cluster. It also calculates the minimum time-span of usable time that any of the clusters have. It uses this number so as not to include time-frequency bins that only have events of one cluster stacked into them, as this would make different treatment of the background and on-source. The number of events in the stacked cluster is definitively $N_{\text{time-bins}} \times N_{\text{frequency-bins}}$. The stacked cluster is defined as a copy of the first cluster in the list, and then its fields are redefined as vectors of zeros in the appropriate dimensions given the number of stacked events. We then cycle through each time and frequency bin and select the loudest event in that bin from each cluster to stack. The values for the significance and likelihood fields for each event in the stacked cluster become the sum of the significances and likelihoods of the loudest event from each unstacked cluster. This function then returns a cluster object which is the stacked events from all of the unstacked clusters passed in.

stackMultipleClusters3detPrebinned.m The same as the `stackMultipleClusters` script, but with two changes. This accepts a list of cluster objects whose

events are all pre-binned. This yields the same results, but makes run time much fast due to not having to bin each cluster before stacking it. It also assumes that we are stacking multiple events, some of which have two detectors in the network, and some having three. The triggers with three detectors have 14 different measures of the likelihood, and only 11 of these overlap with the two-detector case. We discard the extra three fields.

stackMultipleClusters3detPrebinnedWeighted.m Same as previous scripts.

Accepts a list of weighting factors.

stackingsetup.py This is the python wrapper to set up the runs to do the stacking. It takes as arguments the name of the source (ex. SGR 1935+2154), and a parameters file (.ini), which contains the parameters of the stacking. The parameters file also contains the address of a .txt file, which contains the relevent information on each trigger (name, run directory, detector network, gps time, network sensitivity, and fluence). This script runs in much the same way as grb.py does. It outputs and saves the run parameters, and checks that the proper parameters were received. It reads the run parameters and the output folder, and the individual burst info file.

Then it sets up the directory structure. The outputs from each individual x-pipeline run must be binned individually, so it sets up folders to store the binned outputs in. For example, it creates the ouput folder, then a folder for each individual burst in the output folder, then a binned_output folder in each of those, and in each binned_output folder it has a folder for the on-source, off-source, and ul-source files. It then sets up a different directory structure within each folder with addresses for which groups of files are

binned together in the same job in Condor. It then generates submission files and a .dag file to submit to Condor to run the binning.

It sets up an additional directory structure for the stacking. It uses the GPS time when the script was run as a unique identifier to produce a unique folder for the stacked outputs. This allows the user to run the stacking multiple times with different parameters, or redo it in the case of a mistake, without having to redo the binning stage. It creates address files which each contain a list of binned files, one from each x-pipeline run, to stack. It then sets up submission files and .dag files for condor, which each call the binary executable corresponding to `stackMultipleClustersFromAddress.m`. A similar process is being developed for the injections files.

tfBinClustersFromAddress.m This is the script that generated the binary executable that the .sub file calls. It takes as arguments the names of an address file holding a list of clusters from a single x-pipeline analysis that need to be binned. It also takes a raw output folder (where it finds the files needing to be binned), a save location to save the binned files, and the basic properties of the run read from the parameters file. It opens the address file, bins each file on the list according to the parameters, and saves each binned file in its respective binned folder.

stacking_params.ini This is an example parameters file of the search. All the parameters which are commonly applied to all of the x-pipeline analyses are given here, most notably `dt`, `df`, the minimum and maximum frequencies to stack, the minimum and maximum cluster significance values to consider, a boolean variable `weight_by_fluence`, and a boolean `review_mode` that

controls print statements. This file also indicates an output folder where the output of the stacking will be stored, and the address of a file containing the relevant properties of each burst (identifying name, analysis directory, detector network, gps time, network sensitivity, fluence).

For ease of development some scripts have hard-coded parameters that pertain to those of the standard x-pipeline runs, specifically the 3 s circular time slides, the superdecimate rate, and the block time. In the future, these will become fields in the parameters file such that the user can robust x-pipeline searches and stack the results.

stackMultipleClustersFromAddress.m This is the matlab file upon which the binary executable file for the stacking is based. It takes as a parameter the name of an address file, which contains a list of files to stack, and the parameters by which to stack them. It stacks the files, and saves the stack in the output folder.

tfBinClusterFromFilelist.m This script is the one that reads in the x-pipeline output clusters from their .mat files. It takes as arguments a list of file names, a folder where these files are found, and a folder in which to save the binned result. It then calls `tfBinCluster.m`, which effectively replaces the cluster object in the .mat file with a binned version. The .mat file with the binned version of the cluster is then saved in the save location, with the original file name.

REFERENCES CITED

- [1] K. Hurley. 2021. URL
<https://www.ssl.berkeley.edu/khurley/ipn3/sgrlist.txt>.
- [2] M. F. Corcoran. Nasa's heasarc: Archive. Feb 2022. URL
<https://heasarc.gsfc.gov/docs/archive.html>.
- [3] A. L. Watts et al. Detection with rhesi of high-frequency x-ray oscillations in the tail of the 2004 hyperflare from sgr 1806–20. *The Astrophysical Journal*, 637(2):L117, jan 2006. doi: 10.1086/500735. URL
<https://dx.doi.org/10.1086/500735>.
- [4] R. Johnston. Gravitational-wave related images, 2005. URL
<https://www.johnstonsarchive.net/relativity/pictures.html>.
- [5] LIGO Scientific Collaboration. Advanced ligo. *Classical and Quantum Gravity*, 32(7):074001, Mar 2015. ISSN 1361-6382. doi: 10.1088/0264-9381/32/7/074001. URL
<http://dx.doi.org/10.1088/0264-9381/32/7/074001>.
- [6] The LIGO Scientific Collaboration. LIGO: the laser interferometer gravitational-wave observatory. *Reports on Progress in Physics*, 72(7):076901, jun 2009. doi: 10.1088/0034-4885/72/7/076901. URL
<https://doi.org/10.1088/0034-4885/72/7/076901>.
- [7] D. Sigg. Laser interferometer gravitational-wave observatory, 2003. URL
<https://dcc.ligo.org/DocDB/0028/T970101/000/T970101-B.pdf>.
- [8] R. Adhikari. ALS glitches: Need detchar monitor. Dec 2018. URL
<https://alog.ligo-wa.caltech.edu/aLOG/index.php?callRep=45924>.
- [9] S. Dwyer. ALS work today, 2017. URL
<https://alog.ligo-wa.caltech.edu/aLOG/index.php?callRep=36645>.
- [10] J. Driggers. Length feedforward calculations. Oct. 2016. URL
<https://dcc.ligo.org/DocDB/0139/T1600504/001/LSCfeedforward.pdf>.
- [11] K. Merfeld et al. Prcl feedforward filter created, 2019. URL
<https://alog.ligo-wa.caltech.edu/aLOG/index.php?callRep=51553>.
- [12] S. Dwyer and K. Merfeld. Noise budget injections, 2019. URL
<https://alog.ligo-wa.caltech.edu/aLOG/index.php?callRep=51758>.

- [13] K. A. Strain and B. N. Shapiro. (83), jun 2012. URL <https://doi.org/10.1063/1.4704459>.
- [14] The LIGO-Virgo-KAGRA Collaboration. Search for gravitational-wave transients associated with magnetar bursts in Advanced LIGO and Advanced Virgo data from the third observing run, 2022. URL <https://arxiv.org/abs/2210.10931>.
- [15] D. R. Lorimer et al. A bright millisecond radio burst of extragalactic origin. *Science*, 318(5851):777–780, Nov 2007. ISSN 1095-9203. doi: 10.1126/science.1147532. URL <http://dx.doi.org/10.1126/science.1147532>.
- [16] The LIGO Scientific Collaboration, the Virgo Collaboration, the KAGRA Collaboration, and CHIME/FRB Collaboration. Search for gravitational waves associated with fast radio bursts detected by CHIME/FRB during the LIGO–Virgo observing run O3a. 2022.
- [17] Enoto et al. Detection of pulsed radio emission from new magnetar Swift J1818.0-1607, . URL <http://www.astronomerstelegam.org/?read=13553>.
- [18] S. Zhong et al. On the distance of sgr 1935+2154 associated with frb 200428 and hosted in snr g57.2+0.8. 898(1):L5, jul 2020. doi: 10.3847/2041-8213/aba262. URL <https://dx.doi.org/10.3847/2041-8213/aba262>.
- [19] S. A. Olausen and V. M. Kaspi. The McGill magnetar catalog. *The Astrophysical Journal Supplement Series*, 212(1):6, apr 2014. doi: 10.1088/0067-0049/212/1/6. URL <https://dx.doi.org/10.1088/0067-0049/212/1/6>.
- [20] B. Marcote et al. A repeating fast radio burst source localized to a nearby spiral galaxy. *Nature*, 577(7789):190–194, January 2020. doi: 10.1038/s41586-019-1866-z.
- [21] V. M. Kaspi and A. M. Beloborodov. Magnetars. *Annual Review of Astronomy and Astrophysics*, 55(1):261–301, aug 2017. doi: 10.1146/annurev-astro-081915-023329. URL <https://doi.org/10.1146/annurev-astro-081915-023329>.
- [22] E. P. Mazets et al. *Nature*, 282:261–301, 1979.
- [23] T. L. Cline et al. *The Astrophysical Journal*, 255:45–48, 1982.
- [24] C. Thompson and R. C. Duncan. *MNRAS*, 275:255–300, 1995.
- [25] C. Thompson and R. C. Duncan. *The Astrophysical Journal*, 73:322–342, 1996.

- [26] C. Kouveliotou et al. *Nature*, 393:235–237, 1998.
- [27] C. Kouveliotou et al. Discovery of a magnetar associated with the soft gamma repeater SGR 1900+14. *The Astrophysical Journal*, 510(2):L115–L118, jan 1999. doi: 10.1086/311813. URL <https://doi.org/10.10862F311813>.
- [28] G. L. Israel et al. The discovery of 8.7 second pulsations from the ultrasoft x-ray source 4u 0142+61. *The Astrophysical Journal*, 433:L25, sep 1994. doi: 10.1086/187539. URL <https://doi.org/10.10862F187539>.
- [29] F. P. Gavriil et al. Magnetar-like x-ray bursts from an anomalous x-ray pulsar. *Nature*, 419:142–144, September 2002.
- [30] V. M. Kaspi et al. A major soft gamma repeater-like outburst and rotation glitch in the no-longer-so-anomalous x-ray pulsar 1e 2259+586. *The Astrophysical Journal*, 588(2):L93–L96, apr 2003. doi: 10.1086/375683. URL <https://doi.org/10.10862F375683>.
- [31] R. C. Duncan. Global seismic oscillations in soft gamma repeaters. *The Astrophysical Journal*, 498(1):L45–L49, may 1998. doi: 10.1086/311303. URL <https://doi.org/10.10862F311303>.
- [32] S. P. Tendulkar et al. PROPER MOTIONS AND ORIGINS OF SGR 1806–20 AND SGR 190014. *The Astrophysical Journal*, 761(1):76, nov 2012. doi: 10.1088/0004-637x/761/1/76. URL <https://doi.org/10.10882F0004-637x2F7612F12F76>.
- [33] The CHIME/FRB Collaboration. A bright millisecond-duration radio burst from a galactic magnetar. *Nature*, 587(7832):54–58, nov 2020. doi: 10.1038/s41586-020-2863-y.
- [34] B. Grossan. Possible periodic windowed behavior in SGR19352154 bursts. *Publications of the Astronomical Society of the Pacific*, 133(1025):074202, jul 2021. doi: 10.1088/1538-3873/ac07b1. URL <https://doi.org/10.10882F1538-38732Fac07b1>.
- [35] D. Wen et al. GW170817 implications on the frequency and damping time of f-mode oscillations of neutron stars. *Phys. Rev. C*, 99:045806, Apr 2019. doi: 10.1103/PhysRevC.99.045806. URL <https://link.aps.org/doi/10.1103/PhysRevC.99.045806>.
- [36] K. Ackley et al. Neutron star extreme matter observatory: A kilohertz-band gravitational-wave detector in the global network. *Publications of the Astronomical Society of Australia*, 37:e047, 2020. doi: 10.1017/pasa.2020.39.

- [37] K. D. Kokkotas and B. G. Schmidt. Quasi-normal modes of stars and black holes. *Living Reviews in Relativity*, 2(1), sep 1999. doi: 10.12942/lrr-1999-2. URL <https://doi.org/10.129422Flrr-1999-2>.
- [38] N. Andersson. Two simple models for gravitational-wave modes of compact stars. *General Relativity and Gravitation*, 28:1433–1445, 1996. doi: 10.1007/BF02113773. URL <https://doi.org/10.1007/BF02113773>.
- [39] N. Andersson and K. D. Kokkotas. Towards gravitational wave asteroseismology. *Monthly Notices of the Royal Astronomical Society*, 299(4): 1059–1068, oct 1998. doi: 10.1046/j.1365-8711.1998.01840.x. URL <https://doi.org/10.10462Fj.1365-8711.1998.01840.x>.
- [40] O. Benhar and et al. Gravitational wave asteroseismology reexamined. *Physical Review D*, 70(12), dec 2004. doi: 10.1103/physrevd.70.124015. URL <https://doi.org/10.11032Fphysrevd.70.124015>.
- [41] C. Chirenti et al. Fundamental oscillation modes of neutron stars: Validity of universal relations. *Physical Review D*, 91(4), feb 2015. doi: 10.1103/physrevd.91.044034. URL <https://doi.org/10.11032Fphysrevd.91.044034>.
- [42] H. K. Lau et al. INFERRING PHYSICAL PARAMETERS OF COMPACT STARS FROM THEIR r -MODE GRAVITATIONAL WAVE SIGNALS. *The Astrophysical Journal*, 714(2):1234–1238, apr 2010. doi: 10.1088/0004-637x/714/2/1234. URL <https://doi.org/10.10882F0004-637x2F7142F22F1234>.
- [43] J. M. Lattimer et al. Constraining the equation of state with moment of inertia measurements. *The Astrophysical Journal*, 629(2):979–984, aug 2005. doi: 10.1086/431543. URL <https://doi.org/10.10862F431543>.
- [44] K. Ioka. Magnetic deformation of magnetars for the giant flares of the soft gamma-ray repeaters. *Monthly Notices of the Royal Astronomical Society*, 327(2):639–662, 10 2001. ISSN 0035-8711. doi: 10.1046/j.1365-8711.2001.04756.x. URL <https://doi.org/10.1046/j.1365-8711.2001.04756.x>.
- [45] K. Hurley et al. A giant periodic flare from the soft γ -ray repeater sgr1900+14. *Nature*, 397:41–43, 1999. doi: 10.1038/16199. URL <https://doi.org/10.1038/16199>.
- [46] M. Feroci et al. A giant outburst from SGR 1900+14 observed with the BeppoSAX Gamma-Ray Burst Monitor. *The Astrophysical Journal*, 515(1): L9, feb 1999. doi: 10.1086/311964. URL <https://dx.doi.org/10.1086/311964>.

- [47] P. M. Woods et al. Variable spin-down in the soft gamma repeater sgr 1900+14 and correlations with burst activity. *The Astrophysical Journal*, 524(1):L55, sep 1999. doi: 10.1086/312297. URL <https://dx.doi.org/10.1086/312297>.
- [48] A. Corsi and B. J. Owen. Maximum gravitational-wave energy emissible in magnetar flares. *Phys. Rev. D*, 83:104014, May 2011. doi: 10.1103/PhysRevD.83.104014. URL <https://link.aps.org/doi/10.1103/PhysRevD.83.104014>.
- [49] B. Zink et al. Are gravitational waves from giant magnetar flares observable? *Phys. Rev. D*, 85:024030, Jan 2012. doi: 10.1103/PhysRevD.85.024030. URL <https://link.aps.org/doi/10.1103/PhysRevD.85.024030>.
- [50] P. D. Lasky et al. Gravitational waves and hydromagnetic instabilities in rotating magnetized neutron stars, 2012. URL <https://arxiv.org/abs/1203.3590>.
- [51] P. Sutton et al. X-Pipeline: an analysis package for autonomous gravitational-wave burst searches. *New Journal of Physics*, 12(5):053034, May 2010. doi: 10.1088/1367-2630/12/5/053034.
- [52] M. Was et al. Performance of an externally triggered gravitational-wave burst search. *Phys. Rev. D*, 86(2):022003, July 2012. doi: 10.1103/PhysRevD.86.022003.
- [53] I. Newton. *Philosophiae Naturalis Principia Mathematica*. Reg. Soc. Praeses, 1686.
- [54] The LIGO and Virgo Collaboration. GW150914: The advanced LIGO detectors in the era of first discoveries. *Physical Review Letters*, 116(13), mar 2016. doi: 10.1103/physrevlett.116.131103. URL <https://doi.org/10.1103/physrevlett.116.131103>.
- [55] The LIGO and Virgo Collaboration. Tests of general relativity with GW150914. 116(22), may 2016. doi: 10.1103/physrevlett.116.221101. URL <https://doi.org/10.1103/physrevlett.116.221101>.
- [56] B. Schutz. *A First Course in General Relativity*. Cambridge University Press, The Edinburgh Building, Cambridge CB2 8RU, UK, second edition, 2009.
- [57] J. B. Hartle. *Gravity, and Introduction to Einstein's General Relativity*. International series of monographs on physics. Pearson, 2014. ISBN 978-93-325-3508-4.
- [58] J. D. E. Creighton. *Gravitational-Wave Physics and Astronomy*. WILEY-VCH, 2011. ISBN 978-3-527-40886-3.

- [59] A. A. Michelson and E. W. Morley. (83), jun 1887.
- [60] B. J. Meers. Recycling in laser-interferometric gravitational-wave detectors. *Phys. Rev. D*, 38:2317–2326, Oct 1988. doi: 10.1103/PhysRevD.38.2317. URL <https://link.aps.org/doi/10.1103/PhysRevD.38.2317>.
- [61] D. E. McClelland. An overview of recycling in laser interferometric gravitational wave detectors. *Australian Journal of Physics*, 48(6):953, January 1995. doi: 10.1071/PH950953.
- [62] A gravitational wave observatory operating beyond the quantum shot-noise limit. *Nature Physics*, 7(12):962–965, sep 2011. doi: 10.1038/nphys2083. URL <https://doi.org/10.10382Fnpphys2083>.
- [63] H. Vahlbruch et al. The GEO 600 squeezed light source. *Classical and Quantum Gravity*, 27(8):084027, apr 2010. doi: 10.1088/0264-9381/27/8/084027. URL <https://doi.org/10.10882F0264-93812F272F82F084027>.
- [64] R. Demkowicz-Dobrzański et al. Fundamental quantum interferometry bound for the squeezed-light-enhanced gravitational wave detector GEO 600. *Physical Review A*, 88(4), oct 2013. doi: 10.1103/physreva.88.041802. URL <https://doi.org/10.11032Fphysreva.88.041802>.
- [65] The LIGO Scientific Collaboration. Enhanced sensitivity of the LIGO gravitational wave detector by using squeezed states of light. *Nature Photonics*, 7(8):613–619, jul 2013. doi: 10.1038/nphoton.2013.177. URL <https://doi.org/10.10382FnpPhoton.2013.177>.
- [66] M. Tse et al. Quantum-enhanced advanced ligo detectors in the era of gravitational-wave astronomy. *Phys. Rev. Lett.*, 123:231107, Dec 2019. doi: 10.1103/PhysRevLett.123.231107. URL <https://link.aps.org/doi/10.1103/PhysRevLett.123.231107>.
- [67] C. W. Misner et al. *Gravitation*. Princeton University Press, United States, 2017.
- [68] V. Martynov et al. 93(11), jun 2016. doi: 10.1103/physrevd.93.112004. URL <https://doi.org/10.11032Fphysrevd.93.112004>.
- [69] M. Andersen and B. Lantz. Enhanced feedforward control for advanced ligo. Apr. 2013. URL <https://dcc.ligo.org/DocDB/0109/T1300907/001/T1300907-feedforward.pdf>.
- [70] L. McCuller. Irrational fitter exploration, 2018. URL <https://dcc.ligo.org/LIG0-G1800571>.

- [71] A. Buikema et al. Sensitivity and performance of the advanced LIGO detectors in the third observing run. *Physical Review D*, 102(6), sep 2020. doi: 10.1103/physrevd.102.062003. URL <https://doi.org/10.11032Fphysrevd.102.062003>.
- [72] K. Merfeld. 2nd order violin damping and monitor filters created, guardian and wiki updated, medm under construction. Mar. 2019. URL <https://alog.ligo-wa.caltech.edu/aLOG/index.php?callRep=47239>.
- [73] Y. Levin and M. van Hoven. On the excitation of f modes and torsional modes by magnetar giant flares. *Monthly Notices of the Royal Astronomical Society*, 418(1):659–663, 11 2011. ISSN 0035-8711. doi: 10.1111/j.1365-2966.2011.19515.x. URL <https://doi.org/10.1111/j.1365-2966.2011.19515.x>.
- [74] K. Kashiyama et al. Magnetar asteroseismology with long-term gravitational waves. *Phys. Rev. D*, 83:081302, Apr 2011. doi: 10.1103/PhysRevD.83.081302. URL <https://link.aps.org/doi/10.1103/PhysRevD.83.081302>.
- [75] K. Hurley et al. An exceptionally bright flare from sgr 1806–20 and the origins of short-duration -ray bursts. *Nature*, 434:1098–1103, 2005. doi: doi.org/10.1038. URL <https://doi.org/10.1038/nature03519>.
- [76] S. Mereghetti et al. The First Giant Flare from SGR 1806-20: Observations Using the Anticoincidence Shield of the Spectrometer on INTEGRAL. *ApJL*, 624(2):L105–L108, May 2005. doi: 10.1086/430669.
- [77] S. E. Boggs et al. The Giant Flare of 2004 December 27 from SGR 1806-20. *ApJ*, 661(1):458–467, May 2007. doi: 10.1086/516732.
- [78] P. Kalmus et al. Search method for unmodeled transient gravitational waves associated with sgr flares. *Classical and Quantum Gravity*, 24(19):S659, sep 2007. doi: 10.1088/0264-9381/24/19/S28. URL <https://dx.doi.org/10.1088/0264-9381/24/19/S28>.
- [79] P. Kalmus. Search for gravitational wave bursts from soft gamma repeaters, 2009. URL <https://arxiv.org/abs/0904.4394>.
- [80] P. Kalmus et al. Stacking gravitational wave signals from soft gamma repeater bursts. *Phys. Rev. D*, 80:042001, Aug 2009. doi: 10.1103/PhysRevD.80.042001. URL <https://link.aps.org/doi/10.1103/PhysRevD.80.042001>.

- [81] J. Abadie et al. Search for gravitational wave bursts from six magnetars. *The Astrophysical Journal Letters*, 734(2):L35, jun 2011. doi: 10.1088/2041-8205/734/2/L35. URL <https://dx.doi.org/10.1088/2041-8205/734/2/L35>.
- [82] LIGO Scientific Collaboration. Search for transient gravitational-wave signals associated with magnetar bursts during advanced ligo’s second observing run. *The Astrophysical Journal*, 874(2):163, Apr 2019. ISSN 1538-4357. doi: 10.3847/1538-4357/ab0e15. URL <http://dx.doi.org/10.3847/1538-4357/ab0e15>.
- [83] P. Schale. Search for gravitational waves from magnetars during advanced ligo’s second observing run. September 2019. URL <https://scholarsbank.uoregon.edu/xmlui/handle/1794/24835>.
- [84] B. Abbott et al. Search for gravitational wave radiation associated with the pulsating tail of the sgr 1806 – 20 hyperflare of 27 december 2004 using ligo. *Phys. Rev. D*, 76:062003, Sep 2007. doi: 10.1103/PhysRevD.76.062003. URL <https://link.aps.org/doi/10.1103/PhysRevD.76.062003>.
- [85] L. Matone et al. Search algorithm for the detection of long-duration narrow-band transients in GW interferometers. *Classical and Quantum Gravity*, 24(19):S649, sep 2007. doi: 10.1088/0264-9381/24/19/S27. URL <https://dx.doi.org/10.1088/0264-9381/24/19/S27>.
- [86] R. Quitzow-James et al. Exploring a search for long-duration transient gravitational waves associated with magnetar bursts. *Classical and Quantum Gravity*, 34(16):164002, jul 2017. doi: 10.1088/1361-6382/aa7d5b. URL <https://dx.doi.org/10.1088/1361-6382/aa7d5b>.
- [87] R. Quitzow-James. Search for long-duration transient gravitational waves associated with magnetar bursts during ligo’s sixth science run. *Classical and Quantum Gravity*, 2016. URL <https://dcc.ligo.org/LIGO-P1600095>.
- [88] K. Merfeld. Search for gravitational-wave transients associated with magnetar bursts during the third Advanced LIGO and Advanced Virgo observing run. *Proceedings of the International Astronomical Union*, 16(S363):187–190, Jun 2020. doi: 10.1017/s1743921322002629. URL <https://doi.org/10.10172Fs1743921322002629>.
- [89] P. A. Evans et al. Swift-BAT trigger 960986: Swift detection of a new SGR Swift J1818.0-1607, . URL <https://gcn.gsfc.nasa.gov/gcn3/27373.gcn3>.
- [90] S. Lesage et al. Re-classification of Fermi GBM triggers 200203137, 200203156/GRB200203A and 200203861. *GRB Coordinates Network*, 26980:1, February 2020.

- [91] Fermi GBM Team. Fermi GBM final real-time localization. *GRB Coordinates Network*, 26969:1, February 2020.
- [92] M. Durant and M. H. van Kerkwijk. Distances to anomalous x-ray pulsars using red clump stars. *The Astrophysical Journal*, 650(2):1070–1081, October 2006. doi: 10.1086/506380.
- [93] The LIGO-Virgo-KAGRA Collaboration. Search for gravitational waves associated with gamma-ray bursts detected by Fermi and Swift during the LIGO–Virgo run O3b. *The Astrophysical Journal*, 928(2):186, apr 2022. doi: 10.3847/1538-4357/ac532b.
- [94] The LIGO-Virgo-KAGRA Collaboration. Search for gravitational waves associated with gamma-ray bursts detected by Fermi and Swift during the LIGO–Virgo run O3a. *The Astrophysical Journal*, 915(2):86, jul 2021. doi: 10.3847/1538-4357/abee15.
- [95] E. Thrane et al. Long gravitational-wave transients and associated detection strategies for a network of terrestrial interferometers. *Phys. Rev. D*, 83: 083004, Apr 2011. doi: 10.1103/PhysRevD.83.083004. URL <https://link.aps.org/doi/10.1103/PhysRevD.83.083004>.
- [96] E. Thrane and M. Coughlin. Searching for gravitational-wave transients with a qualitative signal model: Seedless clustering strategies. *Phys. Rev. D*, 88: 083010, Oct 2013. doi: 10.1103/PhysRevD.88.083010. URL <https://link.aps.org/doi/10.1103/PhysRevD.88.083010>.
- [97] P. Sutton. A rule of thumb for the detectability of gravitational-wave bursts, 2013. URL <https://arxiv.org/abs/1304.0210>.
- [98] P. Sutton. Computing the energy for GW bursts, 2023. URL <https://wiki.ligo.org/Bursts/BurstEgw>.
- [99] The LIGO Scientific Collaboration. Search for gravitational waves associated with gamma-ray bursts during the first Advanced LIGO observing run and implications for the origin of GRB 150906b. *The Astrophysical Journal*, 841(2):89, may 2017. doi: 10.3847/1538-4357/aa6c47. URL <https://doi.org/10.3847/1538-4357/aa6c47>.
- [100] F. Robinet et al. Omicron: A tool to characterize transient noise in gravitational-wave detectors. *SoftwareX*, 12:100620, jul 2020. doi: 10.1016/j.softx.2020.100620. URL <https://doi.org/10.1016/j.softx.2020.100620>.
- [101] R. Essick et al. idq: Statistical inference of non-gaussian noise with auxiliary degrees of freedom in gravitational-wave detectors. *Machine Learning: Science and Technology*, 2(1):015004, 2020.

- [102] J. M. Cordes and T. J. W. Lazio. Ne2001.i. a new model for the galactic distribution of free electrons and its fluctuations, 2003.
- [103] E. Petroff et al. FRBCAT: The Fast Radio Burst Catalogue. *pasa*, 33:e045, September 2016. doi: 10.1017/pasa.2016.35.
- [104] D. J. Champion et al. Five new fast radio bursts from the HTRU high-latitude survey at Parkes: first evidence for two-component bursts. , 460:L30–L34, July 2016. doi: 10.1093/mnrasl/slw069.
- [105] D. Thornton et al. A Population of Fast Radio Bursts at Cosmological Distances. *Science*, 341:53–56, July 2013. doi: 10.1126/science.1236789.
- [106] K. W. Bannister et al. The Detection of an Extremely Bright Fast Radio Burst in a Phased Array Feed Survey. , 841:L12, May 2017. doi: 10.3847/2041-8213/aa71ff.
- [107] R. M. Shannon et al. The dispersion-brightness relation for fast radio bursts from a wide-field survey. *Nature*, 562:386–390, October 2018. doi: <https://doi.org/10.1038/s41586-018-0588-y>. URL <https://www.nature.com/articles/s41586-018-0588-y>.
- [108] R. Luo et al. On the FRB luminosity function - - II. Event rate density. , 494 (1):665–679, May 2020. doi: 10.1093/mnras/staa704.
- [109] CHIME/FRB Collaboration. The chime fast radio burst project: System overview. *The Astrophysical Journal*, 863(1):48, 2018. ISSN The Astrophysical Journal.
- [110] IAU Working Group. Transient name server, 2021. URL <https://www.wis-tns.org>.
- [111] Spitler et al. A repeating fast radio burst. *Nature*, 531(6143):202–25, 2016.
- [112] S. Chatterjee et al. A direct localization of a fast radio burst and its host. *Nature*, 541(7635):58–61, Jan 2017. ISSN 1476-4687. doi: 10.1038/nature20797. URL <http://dx.doi.org/10.1038/nature20797>.
- [113] P. Scholz et al. THE REPEATING FAST RADIO BURST FRB 121102: MULTI-WAVELENGTH OBSERVATIONS AND ADDITIONAL BURSTS. *The Astrophysical Journal*, 833(2):177, dec 2016. doi: 10.3847/1538-4357/833/2/177. URL <https://doi.org/10.3847>.
- [114] V. Gajjar et al. Highest frequency detection of frb 121102 at 4–8 ghz using the breakthrough listen digital backend at the green bank telescope. *The Astrophysical Journal*, 863(1):2, Aug 2018. ISSN 1538-4357. doi: 10.3847/1538-4357/aad005. URL <http://dx.doi.org/10.3847/1538-4357/aad005>.

- [115] Y. G. Zhang et al. Fast radio burst 121102 pulse detection and periodicity: A machine learning approach. *The Astrophysical Journal*, 866(2):149, Oct 2018. ISSN 1538-4357. doi: 10.3847/1538-4357/aadf31. URL <http://dx.doi.org/10.3847/1538-4357/aadf31>.
- [116] E. Fonseca et al. Nine new repeating fast radio burst sources from chime/frb. *The Astrophysical Journal*, 891(1):L6, Feb 2020. ISSN 2041-8213. doi: 10.3847/2041-8213/ab7208. URL <http://dx.doi.org/10.3847/2041-8213/ab7208>.
- [117] The CHIME/FRB Collaboration et al. Chime/frb detection of eight new repeating fast radio burst sources, 2019.
- [118] The CHIME/FRB Collaboration et al. Periodic activity from a fast radio burst source, 2020.
- [119] K. M. Rajwade et al. Possible periodic activity in the repeating FRB 121102. *Monthly Notices of the Royal Astronomical Society*, 495(4):3551–3558, may 2020. doi: 10.1093/mnras/staa1237.
- [120] K. W. Bannister et al. A single fast radio burst localized to a massive galaxy at cosmological distance. *Science*, 365(6453):565–570, Jun 2019. ISSN 1095-9203. doi: 10.1126/science.aaw5903. URL <http://dx.doi.org/10.1126/science.aaw5903>.
- [121] V. Ravi et al. A fast radio burst localized to a massive galaxy. *Nature*, 572(7769):352–354, Jul 2019. ISSN 1476-4687. doi: 10.1038/s41586-019-1389-7. URL <http://dx.doi.org/10.1038/s41586-019-1389-7>.
- [122] E. Platts e. al. A living theory catalogue for fast radio bursts. *Physics Reports*, 821:1–27, Aug 2019. ISSN 0370-1573. doi: 10.1016/j.physrep.2019.06.003. URL <http://dx.doi.org/10.1016/j.physrep.2019.06.003>.
- [123] S. B. Popov et al. Hyperflares of sgrs as an engine for millisecond extragalactic radio bursts, 2007.
- [124] B. D. Metzger et al. Millisecond magnetar birth connects frb 121102 to superluminous supernovae and long-duration gamma-ray bursts. *The Astrophysical Journal*, 841(1):14, May 2017. ISSN 1538-4357. doi: 10.3847/1538-4357/aa633d. URL <http://dx.doi.org/10.3847/1538-4357/aa633d>.
- [125] B. Margalit et al. Fast radio bursts from magnetars born in binary neutron star mergers and accretion induced collapse. *The Astrophysical Journal*, 886(2):110, Nov 2019. ISSN 1538-4357. doi: 10.3847/1538-4357/ab4c31. URL <http://dx.doi.org/10.3847/1538-4357/ab4c31>.

- [126] The LIGO and Virgo Collaboration. GW170817: Observation of gravitational waves from a binary neutron star inspiral. *Physical Review Letters*, 119(16), oct 2017. doi: 10.1103/physrevlett.119.161101. URL <https://doi.org/10.11032Fphysrevlett.119.161101>.
- [127] P. Beniamini et al. Periodicity in recurrent fast radio bursts and the origin of ultra long period magnetars, 2020.
- [128] K. Ioka et al. A binary comb model for periodic fast radio bursts. *The Astrophysical Journal*, 893(1):L26, Apr 2020. ISSN 2041-8213. doi: 10.3847/2041-8213/ab83fb. URL <http://dx.doi.org/10.3847/2041-8213/ab83fb>.
- [129] Y. Levin et al. Precessing flaring magnetar as a source of repeating frb 180916.j0158+65, 2020.
- [130] M. A. Abramowicz et al. Collisions of neutron stars with primordial black holes as fast radio bursts engines. *The Astrophysical Journal*, 868(1):17, Nov 2018. ISSN 1538-4357. doi: 10.3847/1538-4357/aae64a. URL <http://dx.doi.org/10.3847/1538-4357/aae64a>.
- [131] P. Scholtz on behalf of the CHIME/FRB Collaboration. A bright millisecond-timescale radio burst from the direction of the Galactic magnetar SGR 1935+2154.
- [132] C. D. Bochenek et al. STARE2: Detecting fast radio bursts in the milky way. *Publications of the Astronomical Society of the Pacific*, 132(1009):034202, jan 2020. doi: 10.1088/1538-3873/ab63b3. URL <https://doi.org/10.10882F1538-38732Fab63b3>.
- [133] D. Palmer on behalf of the Swift/BAT team. A Forest of Bursts from SGR 1935+2154. URL <http://www.astronomerstelegam.org/?read=13681>.
- [134] S. Mereghetti et al. INTEGRAL discovery of a burst with associated radio emission from the magnetar SGR 19352154. *The Astrophysical Journal*, 898(2):L29, jul 2020. doi: 10.3847/2041-8213/aba2cf. URL <https://doi.org/10.38472F2041-82132Faba2cf>.
- [135] J. W. T. Hessels et al. FRB 121102 bursts show complex time–frequency structure. *The Astrophysical Journal*, 876(2):L23, may 2019. doi: 10.3847/2041-8213/ab13ae.
- [136] The LIGO-Virgo Collaboration. Search for transient gravitational waves in coincidence with short-duration radio transients during 2007–2013. *Phys. Rev. D*, 93(12):122008, June 2016. doi: 10.1103/PhysRevD.93.122008. URL <https://link.aps.org/doi/10.1103/PhysRevD.93.122008>.

- [137] H. Grote. The GEO 600 status. *Class. Quant. Grav.*, 27:084003, 2010. doi: 10.1088/0264-9381/27/8/084003.
- [138] T. Accadia et al. Virgo: a laser interferometer to detect gravitational waves. *JINST*, 7:P03012, 2012. doi: 10.1088/1748-0221/7/03/P03012.
- [139] The CHIME/FRB Collaboration. The First CHIME/FRB Fast Radio Burst Catalog. *arXiv e-prints*, art. arXiv:2106.04352, June 2021.
- [140] The LIGO Scientific Collaboration. Search for gravitational-wave bursts from soft gamma repeaters. *Phys. Rev. Lett.*, 101:211102, Nov 2008. doi: 10.1103/PhysRevLett.101.211102. URL <https://link.aps.org/doi/10.1103/PhysRevLett.101.211102>.
- [141] The LIGO Scientific Collaboration. STACKED SEARCH FOR GRAVITATIONAL WAVES FROM THE 2006 SGR 190014 STORM. *The Astrophysical Journal*, 701(2):L68–L74, jul 2009. doi: 10.1088/0004-637x/701/2/168. URL